Final Report

DOE Contract No. DE-FG36-04G014294

ICEKAP 2004:

A Collaborative Joint Geophysical Imaging Project

at Krafla and IDDP

P.E. Malin, S.A. Onacha, E. Shalev

Division of Earth and Ocean Sciences

Nicholas School of the Environment

Duke University

Durham, NC 27708

ABSTRACT

In this final report, we discuss both theoretical and applied research resulting from our DOE project, ICEKAP 2004: A Collaborative Joint Geophysical Imaging Project at Krafla and IDDP. The abstract below begins with a general discussion of the problem we addressed: the location and characterization of "blind" geothermal resources using microearthquake and magnetotelluric measurements. The abstract then describes the scientific results and their application to the Krafla geothermal area in Iceland. The text following this abstract presents the full discussion of this work, in the form of the PhD thesis of Stephen A. Onacha. The work presented here was awarded the "Best Geophysics Paper" at the 2005 Geothermal Resources Council meeting in Reno.

Relict or active high-temperature hydrothermal systems are areas of complex fluid circulation, active tectonic and volcanic activity. The postulated activities produce microearthquakes and resistivity contrasts which are characteristic of the source process and the medium which they propagate through. Fluid circulation is controlled by fault zones which are buried below the surface and therefore hard to delineate using surface geological mapping tools. This study presents the modeling of buried fault zones using microearthquake and electrical resistivity data based on the assumptions that fluid-filled fractures cause electrical and seismic anisotropy and polarization. In this study, joint imaging of electrical and seismic data is used to characterize the fracture porosity of the fracture zones. P-wave velocity models are generated from resistivity data and used in locating microearthquakes. Fracture porosity controls fluid circulation in the hydrothermal systems and the intersections of fracture zones close to the heat source

form important upwelling zones for hydrothermal fluids. High fracture porosity sites occur along fault terminations, fault-intersection areas and fault traces.

Hydrothermal fault zone imaging using resistivity and microearthquake data combines high-resolution multi-station seismic and electromagnetic data to locate rock fractures and the likely presence fluids in high temperature hydrothermal systems. The depths and locations of structural features and fracture porosity common in both the MT and MEQ data is incorporated into a joint imaging scheme to constrain resistivity, seismic velocities, and locations of fracture systems. The imaging of the fault zones is constrained by geological, drilling, and geothermal production data. The main objective is to determine geophysical interpretation techniques for evaluating structural controls of fluid circulation in hydrothermal systems. The conclusions give below are results from this study;

- The directions of MT polarization and anisotropy and MEQ S-wave splitting at most of the sites correlate. Polarization and anisotropy are caused by fluid filled fractures at the base of the clay cap.
- Microearthquakes occur mainly on the boundary of low resistivity within the fracture zone and high resistivity in the host rock. Resistivity is lowest within the core of the fracture zone and increases towards the margins of the fracture zone. The heat source and the clay cap for the hydrothermal have very low resistivity of less than 5Ωm.
- Fracture porosity imaged by the resistivity modeling indicates that fracture porosity varies between 45-5% with most of the porosity between 10-20%

which is comparable to porosity values from core samples in the hydrothermal systems in volcanic areas in Kenya and Iceland. This study shows that for resistivity values above 60Ωm, the porosity reduces drastically and therefore this might be used as the upper limit for modeling fracture porosity from resistivity. When resistivity is lower than 5Ωm, the modeled fracture porosity increases drastically indicating that this is the low resistivity limit. This is because at very low resistivity in the heat source and the clay cap, the resistivity is dominated by ionic conduction rather than fracture porosity.

- Microearthquakes occur mainly in the hydrothermal system above the heat source which is defined by low resistivity at a depth of 3-4.5 km at the Krafla hydrothermal system and 4-7 km in the Longonot hydrothermal system.
- Conversions of S to P waves occur for microearthquakes located above the heat source within the hydrothermal system. Shallow microearthquakes occur mainly in areas that show both MT and S-wave anisotropy.
- S-wave splitting and MT anisotropy occurs at the base of the clay cap and therefore reflects the variations in fracture porosity on top of the hydrothermal system.
- In the Krafla hydrothermal system in Iceland, both MT polarization and MEQ splitting directions align with zones that have high fracture porosity below the clay cap. These zones coincide with fault zones trending in the

NNE-SSW and NW-SE directions in otherwise uniform volcanic rocks and laterally continuous geology. The NW-SE orientation is parallel to the regional shear fractures while the NNE-SSW trending polarizations align parallel to rift zone fracture swarms. This observation and equivalent ones in the other data sets suggest that correlations between MT polarizations and MEQ splitting may be related to fluid filled fractures in the hydrothermal systems.

- In areas of high resistivity (60Ωm), the P-wave velocity approaches that of the rock matrix.
- S-wave splitting polarization is determined from measurements of angles of rotation to get the optimum direction of polarization.
- The use of both MEQ and resistivity data for imaging fracture zones requires that the sites for the MEQ data acquisition system be located close to the fracture zone within the hydrothermal system.

TABLE OF CONTENTS

LIST OF TABLES

LIST OF FIGURES

LIST OF ABBREVIATIONS

[Insert List of Abbreviations here, if necessary.]

INTRODUCTION

Relict or active hydrothermal systems are areas of complex fluid circulation, tectonic activity and volcanic activity. Heat sources for hydrothermal systems include magma chambers, young dikes and frictional heating due to faulting (Lanchenbrunch 1980). Ancient hydrothermal flow is recorded in hydrothermally metamorphosed rock masses and veins (Curewitz and Karson 1997). The postulated activities produce microearthquakes which are characteristic of the source process and the medium which they propagate through. The fluid circulation is controlled by fault zones which are buried below the surface and therefore hard to delineate using surface geological mapping tools. This study focuses on alternative methods of using collocated microearthquake and resistivity data to map buried fault zones and locate the heat sources for the hydrothermal system.

Resistivity methods have been used in hydrothermal exploration for many years. Calibration of this method against drilling results has been done in several geothermal fields, and it is apparent that resistivity measurements can be used as a subsurface thermometer (Árnason, 2000). This correlation between resistivity and temperature is associated with the local degree of hydrothermal alteration. Most high-temperature hydrothermal systems are associated with a low resistivity layer over the geothermal reservoir due to clay mineral alteration.

The use of resistivity methods gives unique information about the rock properties, temperature and degree of hydrothermal alteration. This information can be used in resolving the geometry of the hydrothermal reservoir, depth to hydrothermal reservoir,

fracture zones and permeability distribution. Resistivity variations are usually related to salinity, water saturation, porosity, and cation exchange capacity in hydrated clays (Cumming et. al 2000). Understanding the low resistivity distribution can contribute to the location of the high temperature upflow zones as targets for drilling. The resistivity distribution is also used in evaluating depth to the geothermal reservoir and dimensions of the heat source.

In MT methods, the resistivity properties of the rocks are determined from the measurements of orthogonal components of the natural time varying electrical and magnetic fields. The electrical fields are measured by two sets of orthogonal non-polarizing electrodes while the magnetic field by induction coils. In this study we will use MT measurements acquired at frequencies of 400-0.0025HZ). EM field propagate into the Earth as coupled E- and H- fields. The fields are commonly represented in the frequency domain as a four element impedance tensor. The apparent resistivity is obtained from the scaled ratio of $\sqrt{\frac{E}{H}}$. If the subsurface 2D, EM fields are usually polarized into two modes usually referred to as TE-mode when the E fields are parallel to the direction of strike and the TM-mode when the H-field is parallel to the strike direction. One of the problems in the interpretation of MT data is the static shift. The shift is caused by shallow polarization of the EM fields by local resistivity contrasts at the scale of the measurement dipole (in this study 50-70 m) that lead to a constant vertical displacement of the MT apparent resistivity curve on a log scale at all frequencies. To sort distortions on the MT data, different decomposition techniques (Groom and Bailey, 1991, Torquil Smith, 1995) are used to correct 3-D impedance for statics and non 2-D

distortions. These shifts were corrected by the TEM data before interpretation. The characteristics of the MT curves are analyzed to extract structural information that is used to determine high-permeability zones and upflow zones of the hydrothermal systems.

The goal of this study is to combine microearthquake and electrical resistivity data to image fault zones and determine fracture porosity. This study addresses the integrated scientific challenges of developing methods of fault zone characterization and analysis in high temperature hydrothermal systems found in zones of extensional tectonics. The scientific and application challenge is to map the fault zones and determine their size, orientation and depth. Microearthquake and the resistivity imaging are used to map buried faults zones and the role of the intersections of the faults in transmitting fluids in hydrothermal systems.

As a starting point to Joint Geophysical Imaging (JGI) mathematical study of the data that both combine into one set that takes into account their known geological setting, this study establishes the relationship between resistivity, P-wave velocity and porosity. This relationship is proposed as an initial step for further research in JGI. The relationship between resistivity and shear wave anisotropy is used as a useful tool of imaging the depth, size and orientation of fault zones. In this structural approach, the study assumes that gradients in acoustic impedances and resistivity occur at the same structural boundary due to variations in fracture porosity of the rocks. Initial joint imaging is carried out on the MT data after using TEM data to correct for static shifts then carrying out the inversion for closely spaced MT stations. This study uses the principal of average conductance and 2-D Non Linear Conjugate Gradient (NLCG)

method for MT data interpretation to determine the depth to the anisotropic area close to the fault zone.

The special focus the joint imaging is to map the subsurface location, orientation, and size of fracture zones and fractures. This study presents evidence of local correlations between MT polarization and S-wave splitting directions, directions that also match surface geologic and drill hole fracture zone and fracture directions. This study also correlates the results of data analysis from a new hydrothermal system in Kenya with that from Krafla hydrothermal system in Iceland. The microearthquake and resistivity data used in this study was acquired with instruments bought by funding from the United Nations Environmental Program (UNEP) in collaboration with the Kenya Electricity Generating Company (KenGen), the Icelandic National Power Company, Landsvirkjun and Icelandic Geosurvey (ISOR), and DOE.

This study has been carried to contribute to the on going research in the scientific community to carry out joint interpretation of geophysical data to constrain models obtained by different inversion schemes to minimize the difference between a starting model response and the observed data. The tasks undertaken are listed below.

1. Joint TEM and MT data interpretation. The TEM and MT data was used in a joint imaging to correct for static shifts inherent in MT methods. 1-D models generated from TEM data in the vicinity of the MT measurements were used to correct for static shifts. The characteristics of the MT curves have been analyzed to extract information on lateral variation in resistivity and physical parameters that give evidence of the presence fluid

circulation in the hydrothermal systems. In particular, the MT data was analyzed with emphasis on determining the dimensions of conductive zones that coincident with degree of hydrothermal alteration which can be a proxy for either relict hydrothermal systems or the temperature of the hydrothermal fluids. In MT methods when the magnetic field is polarized along the strike direction, then the current density at a lateral resistivity interface is discontinuous and this is known as the TM mode. As pointed out by Wannamaker (1999), lateral changes in resistivity are often derived from TM mode impedance. Recent 2-D numerical modeling studies of a conductive fault zone indicate that closely spaced TM mode MT data can be used to locate a fault structure (Ingham M., 2005).

2. Reduce, analyze and interpret Krafla data sets for the types of electrical and microearthquakes signatures associated with local tectonics. This includes location of earthquakes. Critical analysis of microearthquakes to establish whether they have characteristic signals associated with tectonic movements, fluid movement in the upflow zone and fluid movement in the downflow zone. The pores, cracks, fractures, fissures, joints, faults, and the internal rock structures are important in controlling the storage and transmission of fluids in rocks. This study takes into consideration that several theoretical formulations to study seismic propagation in porous or fractured medium have been formulated over the years (Biot 1956; Hudson, 1981 and O'Connell and Budiansky, 1974) but their field

applications have been limited. The physical properties of porous medium are usually determined by evaluating the interaction between the solid grains and pore fluid, parameters that characterize the structures, and the coupling mechanisms between the solid matrix, fluid, fractures and pressure. The velocity variation due to pressure changes is caused mainly by mechanical coupling between solid grains, pore fluid and the interconnection of the pores (Maultzsch et al., 2003).

3. Determine the local seismic wave velocity and electrical resistivity structure at Krafla, as much as is possible with publicly available modeling codes. Then make use of the expanded Krafla seismic data set from 2004 and 2005 to study S-wave splitting for evidence of fractures. This was achieved through analysis of shear wave polarization and travel times delay caused by anisotropic properties of the propagating medium. In this research, the resistivity structure is used to constrain the velocity model. Initial velocity models will be based on the depths to the resistivity interfaces of 1-D resistivity sections.
4. Critical evaluation and modeling the evidence for MT polarization orientations that correlates with the seismic anisotropy. S-wave anisotropy is usually caused by aligned systems of open, fluid-filled micro-fractures. It has been noted in many surveys that the structurally-caused anisotropy is strongly frequency dependent (Orange, 1989). Since the primary target for productive geothermal wells is faults and fractures,

we expect that this anisotropy would be diagnostic of the variability of the factors that affect fluid flow. In this study, it is anticipated that such a relationship can be used to map out the depth and location of fracture systems.

5. Correlate the JGI modeling results with reservoir production zones to establish parameters like permeability thickness product, porosity, degree of alteration of clays and temperature.

This research has direct application to the exploration for renewable geothermal energy. Costs of geothermal power plants are heavily weighted toward early expenses such as well drilling and pipeline construction. During this stage, resource analysis of the drilling information is carried out. The risks of development and the time for construction can tremendously be reduced if the total number of production wells can be reduced by half. For instance a total of 34 wells have been drilled in Krafla within an area covering 3-4 km^2. The initial output from the wells ranges from 2.3 to 19.7 MWe (Gudmundsson, 2001), reflecting the variability in permeability in the hydrothermal reservoir. Two wells in the Krafla geothermal field account for over 50% of the steam required to power the installed capacity of 60MWe. Similar well output variability exists in the Olkaria Geothermal field in Kenya where two wells produce 19 MWe for a power station of an installed capacity of 45 MWe. If these high production wells were drilled at the beginning of the project, there would have been tremendous savings on the infrastructure and the total costs of developing the geothermal power plants. On average it takes about 45-60 days to drill wells to a depth of 2000 m. If we consider the case for

Krafla the drilling of 34 wells would have taken between 4 to 5.5 years of continuous drilling. This is a long time that makes the rapid implementation of geothermal projects difficult. Reducing this number of wells by half, the project costs and therefore the cost of steam per KWh will be reduced significantly and increase the number of plants that can be constructed.

1. Geological and tectonic setting and description of microearthquake and resistivity data acquisition at Krafla in NE Iceland and Longonot in Kenya

1.1 Geological and tectonic setting

Krafla and Longonot hydrothermal systems occur in tectonically active rift zones which are areas of extensional tectonics and volcanisms. The Krafla hydrothermal system is located within an interpreted caldera that lies at the boundary of the America and Europe plates along the Neovolcanic Zone (NZ). The NZ zone with an estimated spreading rate of 0.9cm/year occurs along the Mid-Atlantic Ridge in northeast Iceland.

The Krafla Hydrothermal area lies within the Neovolcanic Zone (NZ) along the Mid-Atlantic Ridge (MAR) extending from the Reykjanes to the Kolbeinsey Ridge in the north. The Neovolcanic Zone is composed of three main branches, the Northern Volcanic Zone (NVZ), the Eastern Volcanic Zone (EVZ) and the Western Volcanic Zone (WVZ). The NZ is composed of central volcanoes and fissures swarms (Figure 1). The geology of the Krafla area is dominated by basaltic lava, hyaloclastites and intrusives. The volcanic activity in this area is episodic, occurring every 250-1000 years, with each episode lasting 10-20 years (Halldor et al., 1987). The last volcanic episode started in 1975 and ended in 1984. The caldera was formed about 100, 0000 years ago (Saemundsson, 1983). This episodic volcanic activity can have an impact on the hydrothermal system by opening up new factures by rifting and injection of magmatic gases mainly carbon dioxide and hydrogen sulfide. The rifting process can change the

fluid flow regimes while the magmatic gases can change the composition of the hydrothermal fluids.

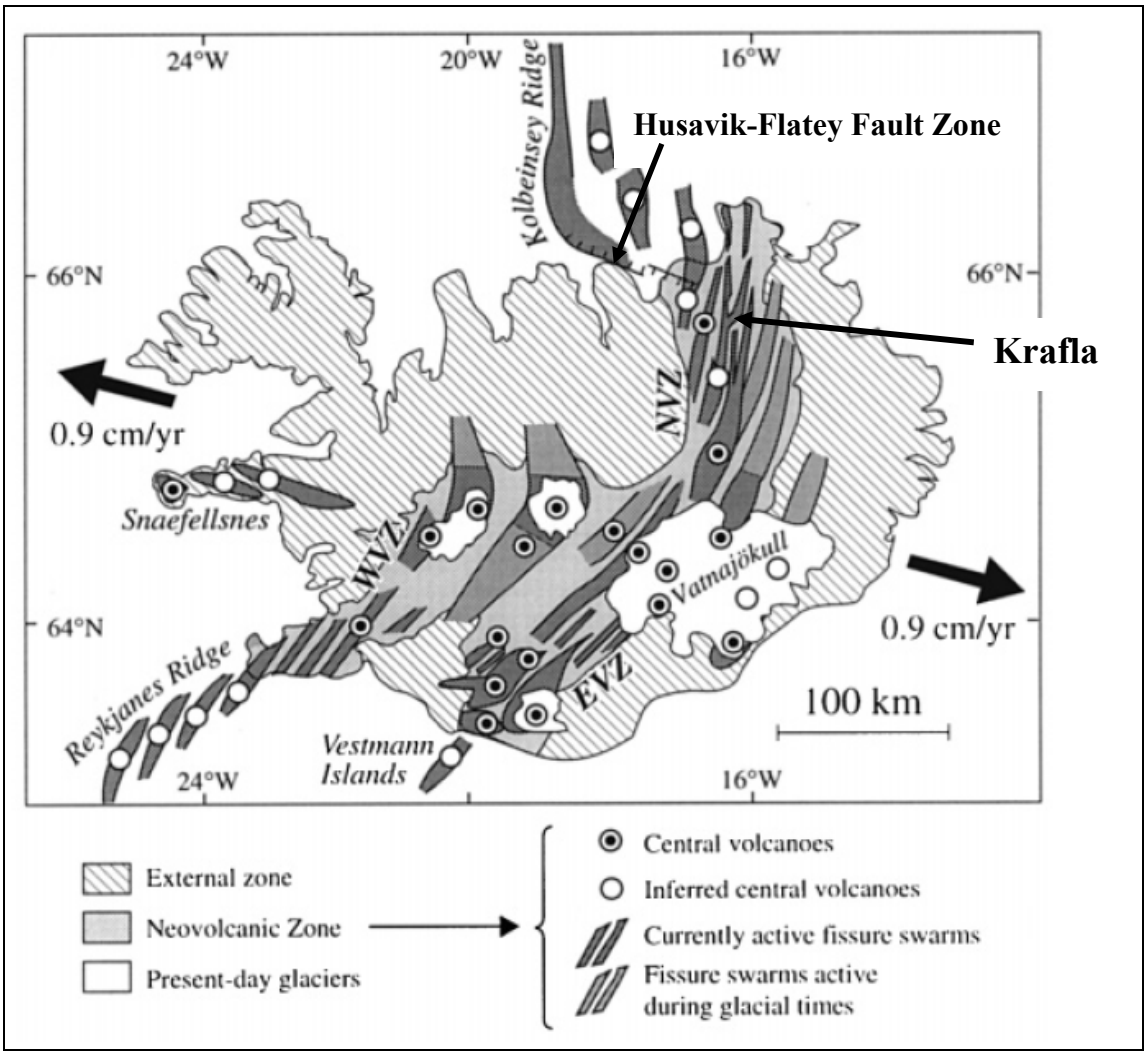

Figure 1 Geological and tectonic setting of Iceland. The Krafla Hydrothermal area lies within the Neovolcanic Zone (NZ) along the Mid-Atlantic Ridge (MAR) extending from the Reykjanes to the Kolbeinsey Ridge in the north. The Neovolcanic Zone is composed of three main branches, the Northern Volcanic Zone (NVZ), the Eastern Volcanic Zone (EVZ) and the Western Volcanic Zone (WVZ). The NZ is composed of central volcanoes and fissures swarms.

The Longonot hydrothermal system is located to the south of the equator in the Kenya Rift Valley which is part of the East Africa Rift System extending from Beira in Mozambique in the south to the Red Sea in the north. The East Africa rift system is associated with an initial domal uplift caused by convective mantle plumes accompanied by extensional crustal rifting. The domal uplift was followed by down warping, volcanism and extensive faulting. Volcanism in the central part of the rift valley started in Miocene and continued to late Pliocene. The

1.1.1 Krafla hydrothermal system

Krafla is a high-temperature hydrothermal system which lies in an active caldera that formed 100,000 years ago (Armannsson et al. 1987) in the rift zone in NE-Iceland. This area has experienced repeated volcanic activity. The last volcanic period started at the end of 1975 and ended in September 1984 with 21 tectonic events and 9 eruptions (Gudmundsson 2001). This volcanic activity occurred along a fissure and released volcanic gases into the hydrothermal reservoir. From studies of S-wave shadows, it has been postulated that a cooling magma chamber exists at shallow depth of 3-8 km below the hydrothermal field (Einarsson 1978).

The Krafla volcanic system is transected by a fissure swarm (Figure 2), which is 4-10 km wide and trends in a near north-south direction (Björnsson, 1985). The hydrothermal manifestations are controlled by tectonic fractures, faults and dykes.

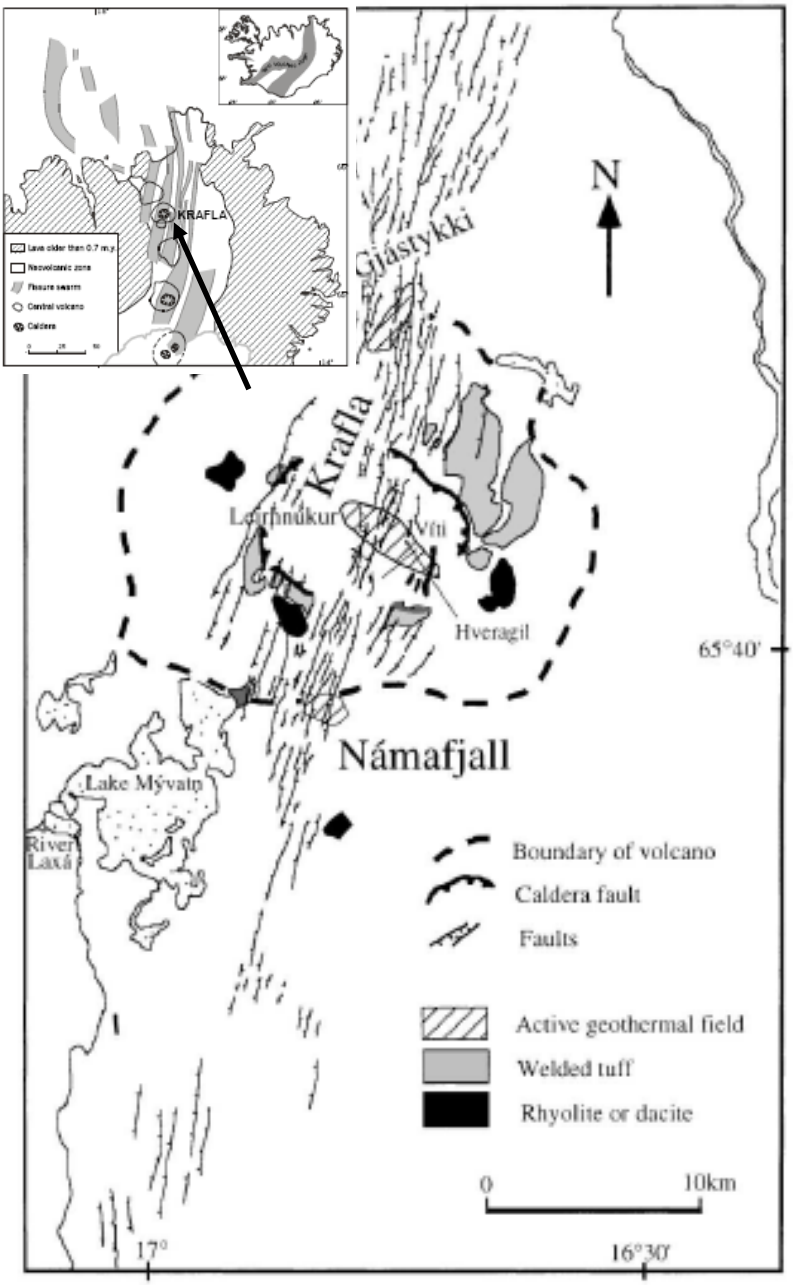

Figure 2 Geological and structural model of Krafla hydrothermal system with a NW-SE trend within an interpreted caldera. The caldera faults have a NW-SE trend while the faults within the volcanic zone have an N to NNE trend. Welded tuff and Rhyolite eruptions occur at the margins of the caldera.

Drilling of geothermal production wells focused on intersecting known fractures and intrusion boundaries at a depth of 800-2100 m. This strategy was aimed at obtaining geothermal wells high mass flow rates.

Additional hydrothermal exploration was carried out between 1984 and 1996 to locate hydrothermal fluid with low magmatic gases and also find replacement wells for some of the wells damaged due to tectonic movements. Although some of the wells were targeted in the known fracture zone, the production was still low. This highlights the problem of fluid flow from the drilled production hydrothermal wells. Analysis of drill cuttings from the wells has facilitated the evaluation of the distribution of individual lithological units, correlation of aquifers with lithology, and the degree of hydrothermal alteration. Intrusive rocks are the dominant features below 1200-1300 m depth.

A geological cross section (Figure 3) in an NW-SE direction across the hydrothermal system shows three stratigraphic units. The upper layer is made of young lava (less than 10,000 years) and a hyaloclasite formation up to a depth of about 200-300m. Rhyolite volcanism identified at Krafla has been attributed to silicic melts of hydrothermally altered crust of basaltic composition. The origin of the rhyolite has been postulated to be on the periphery of an active magma chamber at temperatures of about 850-950°C (Jonasson, 1994).

The second group is made of lava and hyaloclasite rocks up to a depth of 1000-1300m (Halldor et al, 1987). The third stratigraphic unit consists of basaltic lavas with doleritic and minor gabbroic intrusives up to a depth of 2000-2200m. This geological section has been used to constrain the geophysical model. In this study, it is assumed that

the first two stratigraphic units form the capping for the hydrothermal system and are expected to be nearly isotropic and homogenous. The near surface lateral changes are attributed to channeling of hydrothermal fluids along faults and dykes. The third stratigraphic unit is assumed to be anisotropic and therefore forms the basis of this study to evaluate the anisotropic effects on both MT and MEQ data.

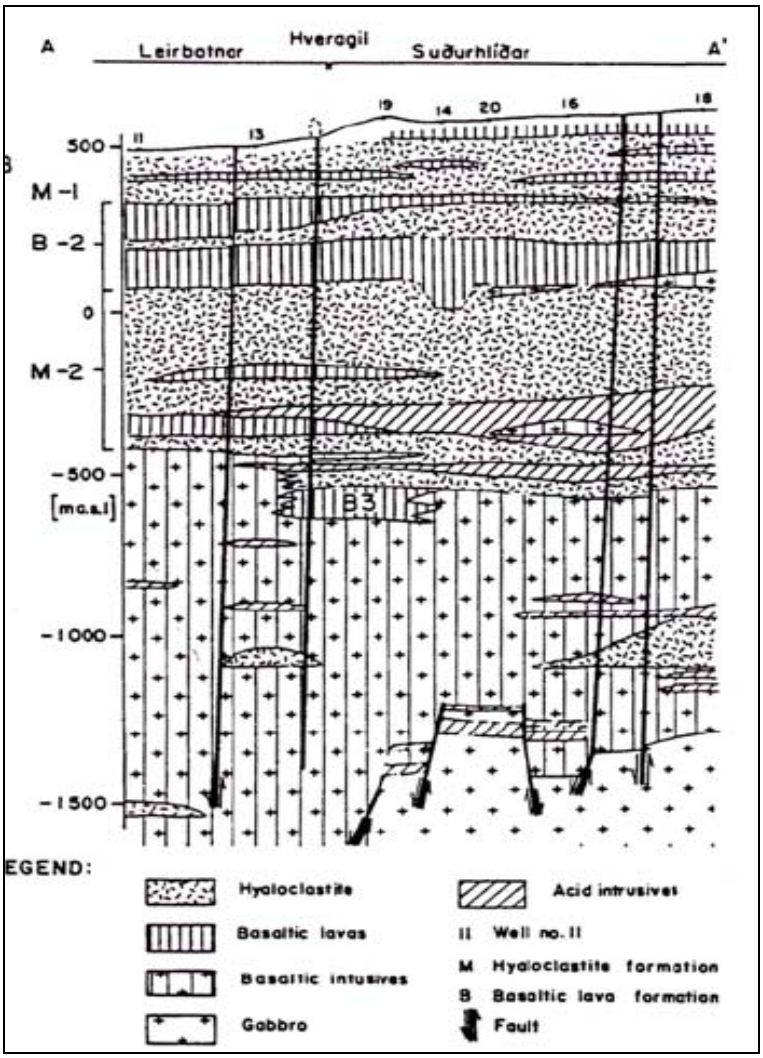

Figure 3 Geological section in a NW-SE direction across the Krafla hydrothermal system. Surface layers to a depth an elevation of 500 mbsl are dominated by hyaloclastites and basaltic lava flows. Below, 500 mbsl, basaltic intrusions, minor acid intrusions and Gabbros dominate.

1.1.1.1 The Krafla hydrothermal system

A total of 34 wells have been drilled at Krafla within an area covering 3-4 km^2. The initial output from the wells ranges from 2.3 to 19.7 MWe (Gudmundsson, 2001), reflecting the spatial variation in permeability across the hydrothermal system. Two wells in the Krafla hydrothermal system account for over 50% of the steam required to power the installed capacity of 60MWe. Similar well output variations exist in other hydrothermal systems like Olkaria in Kenya where two wells produce 19 MWe for a power station of an installed capacity of 45 MWe. The Krafla hydrothermal area is divided into three fields (Figure 4): Leirbotnar, Sudurhlídar and Hvíthólar fields. Although the sectors are within a caldera, the drilled wells show big differences in fluid chemistry, temperature and pressure. The Leirbotnar hydrothermal system is divided into an upper and a lower zone (Stefánsson and Steingrimsson, 1980).

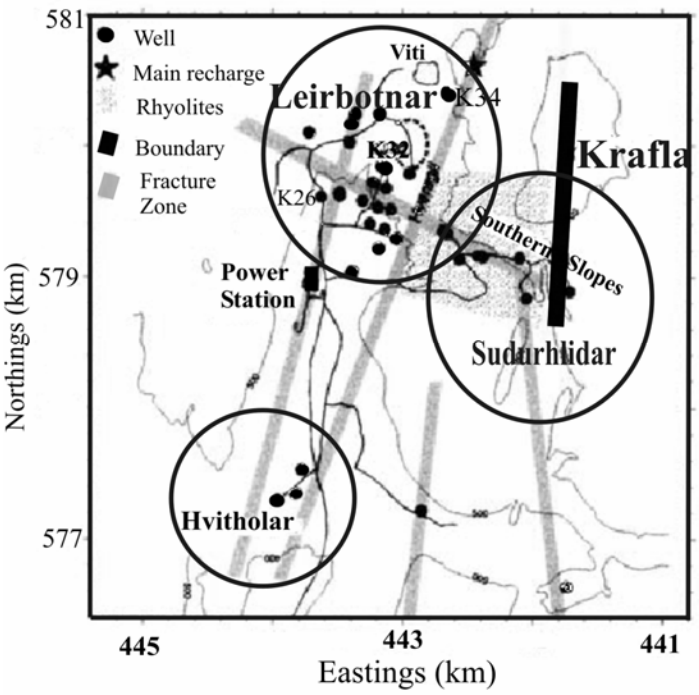

Figure 4 Location of Krafla Hydrothermal System showing the location of 3 geothermal fields and the power plant. The interpreted fracture zones and locations of wells are shown

The upper reservoir to a depth of 1000 m is water saturated with a mean temperature of 205°C. The main aquifers in the lower zone are associated with fissures and intrusives. This lower zone is boiling with temperatures ranging from 300 to 350°C. The Sudurhlídar field is a boiling system while the Hvíthólar field exhibits boiling characteristics down to 700 m depth with a temperature reversal (Armannsson et al. 1987).

1.1.2 Longonot hydrothermal system

The Longonot hydrothermal system is associated within the Longonot Volcano which has a well developed 2 km wide summit crater (reaches a pick altitude of over 2770 masl) and in interpreted caldera covering about 40 km^2 which is postulated to have been formed by a regional withdraws of magma along the rift floor (Scott and Skilling, 1990). The first volcanic eruptions are postulated to have occurred at about 0.4Ma with eruption of trachyte lava and volcanic ash deposits (Scott and Skilling, 1990). Pumice eruptions also occurred at about 9150±110 followed by trachytic volcanic eruptions at about 5650 ypb and explosive eruption of volcanic ash and pumice at about 3280±120 ypb (Scott Skilling, 1990). The eruption of pumice is important because it signifies the interaction of fluids with magmatic sources that could be the heat source for the hydrothermal system. The geological setting and the predominance of the trachytic lava flows may indicate a less favorable high temperature hydrothermal system than one dominated by rhyolitic lavas.

Hydrothermal fluid indicators in this area include fumaroles and altered grounds. The fumaroles occur within the summit crater, southern part of caldera rim and to the

southeast. A shallow well which was drilled to the south west of the inferred caldera for groundwater to a depth of 240m produced steam.

Several geological, geophysical and geochemical studies have been carried out in the Kenya Rift Valley to study and understand the complex geological and tectonic setting of the rift (Karson and curtis, 1989; Green et al., 1991). Most of these studies have been focused on understanding the deep crustal structure and therefore not relevant to evaluating the reservoir properties of the hydrothermal system. The significant finding of most of the studies is that structure of the rift valley varies both along and perpendicular to the rift. Seismic tomographic studies through Longonot have shown low P-wave velocities in the crust interpreted as zones of partial melt.

Previous studies relevant to geothermal exploration at Longonot have been carried by the British Geological Survey, KenGen and Duke University. The Longonot Caldera is thought to have formed at the summit of a large volcanic shield (Clarke et. al. 1990). The main events of the volcano include building of an early shield, pyroclastic and lava cone, formation of a summit crater and crater floor lava eruptions. The rocks in this area are mainly trachyte, pumice, ignimbrite, mixed lava and tuffs. These rocks have high silica content (≥ 60%). From analysis of incompatible trace elements (ICE), Clarke et. al. 1990 noted that:

(a) Data from Longonot interpreted as indicating the tapping of a large magma chamber.

(b) The evolved nature of the most recent volcanic rocks at Longonot indicates that a fractionating magma chamber still exists and that in the next few centuries a moderate sized pyroclastic eruption is expected to occur. This is indeed a very scaring conclusion especially taking into account the development of a power station.

(c) A Tectono-Volcanic Axis (TVA) together with the caldera walls form major structures in this area. However, other structures are probably concealed by pyroclastics.

(d) The Longonot crater seems to be at the intersection of NE and NW trending regional faults. These structures may strongly influence the regional hydrogeology while the grid faults within the rift valley may control the local hydrogeology. The faults might act both as barriers and channels of fluid flow. High permeability shear zones will act as channels of fluid flow. The fault patterns may therefore significantly determine the overall productivity of the wells. The tectonic evolution and in particular the overall stress regime in this area is another important factor.

In 2000, KenGen carried extensive geophysical, geochemical and geological studies of Longonot with a view drilling exploration wells to a depth of 2000m. The hydrothermal systems in Kenya are usually covered by thick volcanic ash which tends to conceal fractures and geothermal manifestations. The Olkaria-Domes Field was identified using resistivity measurements in an area without surface manifestations. Longonot hydrothermal system is covered by more than 600 meters of volcanic ash.

From these examples of hydrothermal systems in Kenya and Iceland, the physical state and spatial distribution of the fracture and fluid systems associated with these sites are not well known. This study therefore focuses on:

(a) Critically evaluate the subsurface resistivity structure with a view of establishing the extent and nature of the hydrothermal system.

(b) Determine the probable fluid flow paths, porosity and temperature distribution so as to give an indication of suitable sites for exploration wells.

(c) Give an indication of the up-flow zones, out-flow features and the role of structures in the control of hydrothermal fluid circulation.

(d) Give an indication of the dimension of the probable heat source in this area.

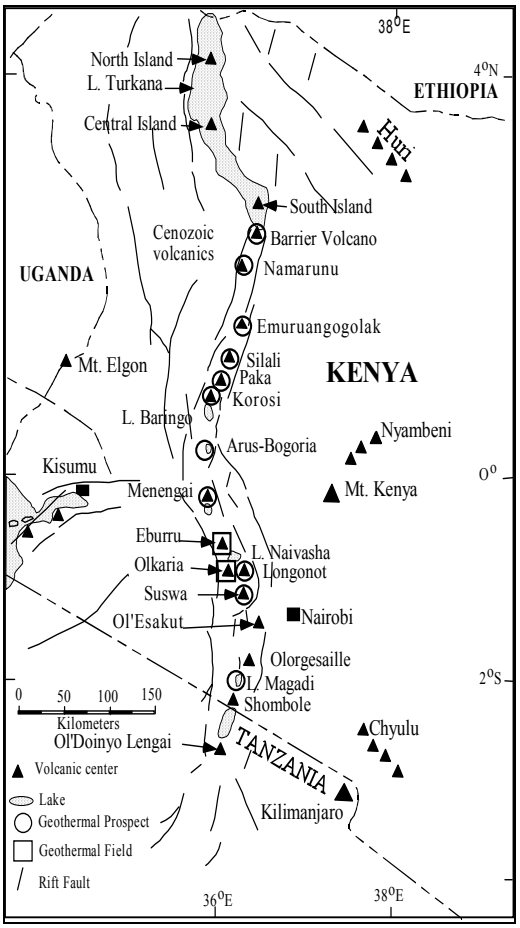
38°E
4°N
ETHIOPIA
North Island
L. Turkana
Central Island
Huri
South Island
Cenozoic
volcanics
Barrier Volcano
Namarunu
UGANDA
Emuruangogolak
Mt. Elgon
Silali
Paka
KENYA
Korosi
L. Baringo
Nyambeni
Arus-Bogoria
Kisumu
0°
Menengai
Mt. Kenya
Eburru
L. Naivasha
Olkaria
Longonot
Suswa
Nairobi
Ol'Esakut
Olorgesaille
2°S
L. Magadi
Shombole
0 50 100 150
Kilometers
Chyulu
Ol'Doinyo Lengai
TANZANIA
Volcanic center
Lake
Geothermal Prospect
Geothermal Field
Rift Fault
Kilimanjaro
36°E
38°E

Figure 5

1.2 Geophysical and geological model of the hydrothermal systems

In this study, the working conceptual model assumes that the total porosity within the hydrothermal reservoir is equivalent to fracture porosity. This is consistent with studies based on the properties of more than 500 samples of igneous rocks in Iceland hydrothermal systems. These studies show that total porosity is equivalent to effective porosity (Sigurdsson et al., 2000). The study and data analysis of igneous rock properties in Iceland by Sigurdsson et al., 2000, indicates that matrix permeability is related to capillary tube model and therefore in this study, the model used is that the flow of fluids in the hydrothermal systems is controlled by faults and dykes.

Fluid movement in a hydrothermal system is also controlled by temperature and pressure gradients, fracture permeability, storativity permeability-thickness product. Storativity is the amount of fluid stored per unit volume of reservoir rock and is a product of thickness and compressibility. The total reservoir compressibility (C_t) is defined below;

$$C_t = \phi C_w + (1-\phi)C_r$$

where C_w is the compressibility of water, C_r is the compressibility of the rock matrix and ϕ is the porosity. In this study we assume that porosity below the clay cap is

mainly controlled by fracture porosity. The total hydrothermal reservoir storativity is therefore a function of the fracture intensity within the fault zone.

The model (Figure 6) used in this study consists of a fault zone, defined as a zone of high fracture porosity which is made up of a core bounded by a damaged zone embedded in a host rock. The fault zone is overlain by a clay cap and recent volcanic rocks. The core is expected to be a region of low resistivity while the damaged zone would have a higher resistivity than the core. The host rock is expected to have the highest resistivity.

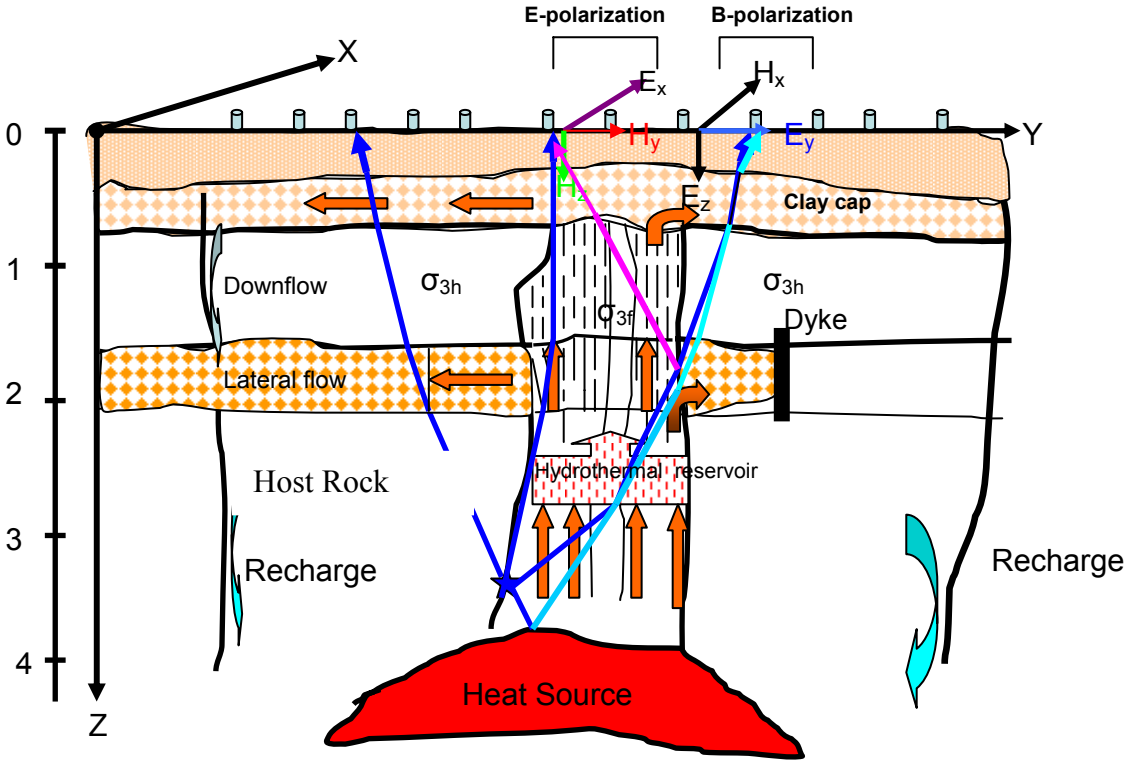

Figure 6 Model for MEQ and Resistivity data interpretation. In this model, the fracture zone defined by lower resistivity and P-wave velocity is within a host rock with high resistivity and P-wave velocity. The clay cap occurs above the hydrothermal system and the heat source below. Microearthquakes occur above the heat source at the contact between low and high resistivity. Conversions of S-waves to P-waves occur on top of the heat source. The resistivity contrasts below the clay cap causes polarization and splitting in the MT data.

The conceptual model of the hydrothermal system (Figure 6) close to the fault zone based on resistivity is therefore postulated to have:

1. A surface layer of recent volcanic rocks or pyorclastics with variable resistivity depending on the age of the rocks and proximity to the fault zone. Areas close to the hydrothermal system are expected to have low resistivity due to alteration of the rocks to low temperature clays. Areas with young basaltic, rhyolitic and trachytic rocks are expected to have high resistivity.
2. The second layer with variable thickness is formed by a clay clap due to alteration of rocks by low temperature hydrothermal fluids.
3. In high temperature hydrothermal systems, the third layer is expected to have a higher resistivity due to a high degree of hydrothermal alteration. The buried fault zone is postulated to have a lower resistivity due to circulation of hydrothermal fluids and high fracture porosity. The fault zone is also postulated to be associated with shear wave splitting. Lateral flow within this zone may be controlled by a series of dykes and intrusives.
4. The heat source for the hydrothermal system occurs below the fault zone and is postulated to have low resistivity.
5. The resistivity contrasts at the fault zone produce anisotropy and polarization both in MT data and shear wave splitting. The anisotropy in MT data is assumed to be due to resistivity contrasts at the base of the clay

cap rather than near surface lateral changes. The MT polarization is postulated to have the same orientation as shear wave polarization.

6. Stresses on the boundary faults and at the boundary of the heat source and host rock produce microearthquakes. It is postulated that microearthquakes produced above the heat source produce conversions of the S-wave to a P-wave.

1.3 Geological and Structural Justification of the Model

The geophysical model is based on the postulated geometry of a buried fault zone within a host rock (Gudmundsson et al., 2002). This model is based on the observations of systems of mineral veins in the damaged zone of Husavik-Flatey Transform Fault Zone with a NW-SE trend (See Figure 1). The fault zone is covered by either volcanic pyroclastic rocks or fresh volcanic rocks and it is divided into a fault core bounded by damaged zones on either side (Figure 7). The core may be formed by tectonic gauge and breccia; the damaged zone is formed next to the core and it consists of breccia and fractures of different sizes (Evans et al., 1997) which could form a zone of high permeability that can allow flow of hydrothermal fluids. The contact between the fault zone and the host rock may form a barrier to lateral fluid flow. The assumption is that the fault zone is expected to have low resistivity with the lowest resistivity within the core. The host rock is postulated to have high resistivity and high P-wave velocity.

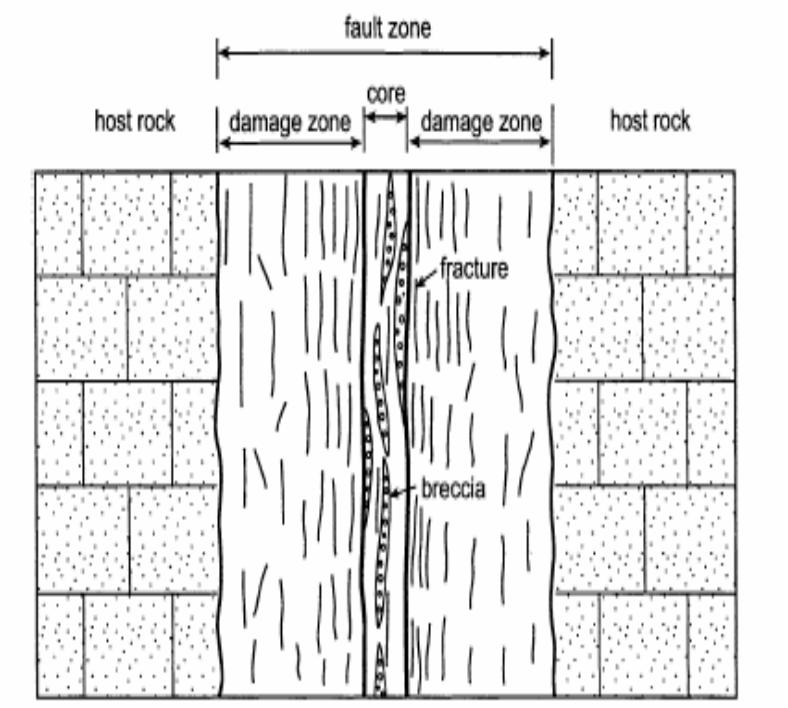

Figure 7. The structural model of a fault zone showing the core, damaged zone and the host rock. Fault displacement generally occurs either at the core or at the contact with the damaged zone. The fluid flow within the damaged zone can be modeled as flow through a fractured medium (After Gudmundsson et al., 2002)

1.3.1 Previous Resistivity Studies at Krafla

Based on DC resistivity (Flóvenz' et al. 1985) proposed the general relationship between bulk resistivity of rocks, porosity and temperature for the upper crust in Iceland. The resistivity structure depends on the age of the volcanic rocks. The resistivity in the high-temperature hydrothermal systems is low 1-10 Ωm at a depth of 500-800m. In the areas of older Quaternary volcanism, typical resistivity at a depth of 200-500m is 100-1000 Ωm.

Electromagnetic measurements have been used extensively to study the study the hydrothermal systems in Iceland (Árnason et al. 2000). A major finding of this work is that all high temperature hydrothermal systems have the same resistivity structure characterized by a low resistivity cap at the outer margins of the hydrothermal system and underlain by a more resistive core within the reservoir. The low resistivity zone has been interpreted as a zone dominated by low temperature (100-200˚C) alteration of rocks to clays. In this clay zone (depth up to 1000m), the resistivity is controlled by both ionic and interface conduction. Below the clay cap, the resistivity is dominated by interface conduction and generally the resistivity increases (Flovenz et al., 2000).

1.3.2 Previous Local seismic activity and velocity studies at Krafla

A microearthquake study around the Krafla Hydrothermal system in 1967 and 1968 (Ward and Bjornsson, 1971) showed a high level of seismicity with an average of 191 events in 1967 and a low level of seismicity with an average of 1.2 events per day. The unusual high level of seismicity was attributed to the inflation of a magma chamber beneath the hydrothermal system at Krafla.

The seismic structure of the Krafla central volcano is characterized by extreme variations in P-wave velocity (Brandsdottir et al., 1995). The resistivity structure is therefore also expected to show these extreme variations. The near surface structure as determined from the seismic undershooting experiment showed that the upper most 2.5 km is almost isotropic.

Based on the results of a 0.2-0.3 s P-wave delay and shear wave shadowing, the preferred interpretation by Brandsdottir et la., 1995 was that the Krafla magma chamber has a width of 2-6 km wide elongate in a NW-SE direction across the rift zone with a thickness of 0.75-1.8 km (Figure 8).

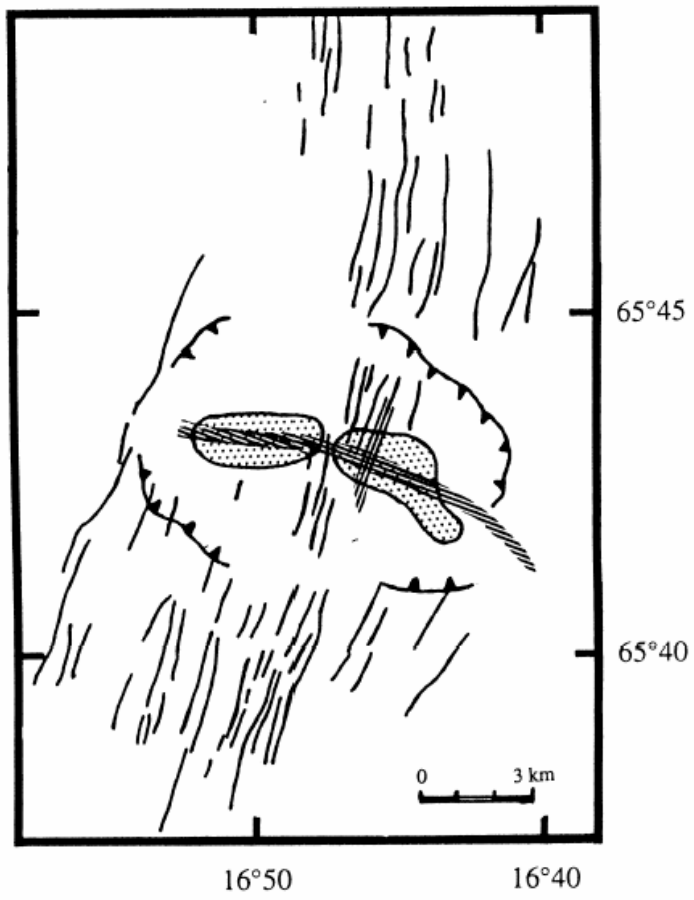

Figure 8 Map of the Krafla caldera showing the fissure swarms, shear wave attenuation zones (shaded regions) delineated by Einarsson (1978), and the P-wave attenuation (stripped zones). The P-wave attenuation zones cuts across the NNE fissure swarm and extend 3km NS and 10 km EW (From Brandsdottir et. al., 1995)

The Krafla area was defined by a high velocity chimney below the magma chamber. The high velocity chimney is 40km wide and dips sharply on both sides at Krafla (Figure 9).

The higher v … preted to indicate that there was no partial … at 20 km (Brandsdottir et al. 1995). This in … nalysis of the MT and microearthquake da …

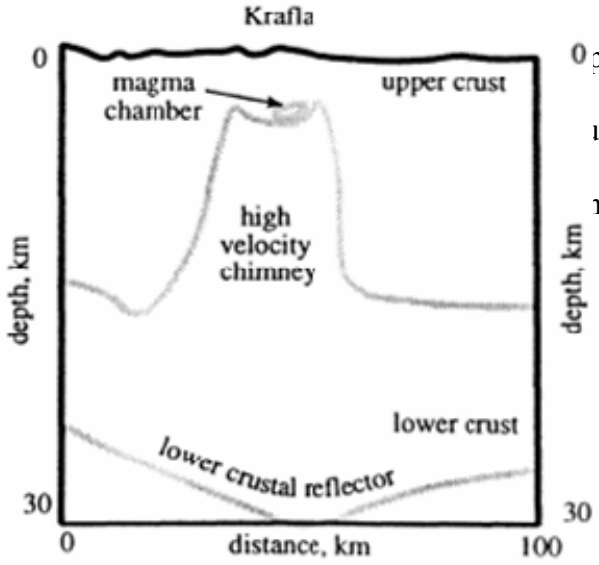

Figure 9 Physical structure of Krafla area showing the interpreted magma chamber, high velocity chimney and seismic reflectors at the lower crust (From Brandstottir et al., 1995).

1.4 Data Acq…

1.4.1 Magnetot…

In Ma… …ontal components of the electric an… …flects the conductivity distribution in some volume below the measurement point. Prior to inverting for a conductivity model, an analysis of the estimated impedance tensor was carried out to understand the basic electrical properties of the earth in the area of investigation.

The MT data used in this study was acquired at the Krafla hydrothermal system in two field campaigns in the summers of 2004 and 2005. Acquisition of high quality Magnetotelluric (MT) and Microearthquake (MEQ) data at the Krafla geothermal field was completed in September 2005. This second data set was acquired to complement the data set acquired in 2004. These data has been used in the Joint Geophysical Imaging

study of the Krafla geothermal area to understand the fluid movement in the hydrothermal system.

The MT data acquisition was carried out at predetermined sites to complement the existing data and also address the concerns already mentioned in the introduction. The final location depended on the conditions at the site. The magnetic coils and potential electrodes were oriented in the orthogonal NS and EW directions (Figure 10). Many of the sites were in areas covered by recent volcanic rocks. The acquisition of high quality data within such an area has demonstrated the value of MT data acquisition in areas with rocks of high resistivity. Some MT sites were located across known fractures to study the effect of open fractures on the MT data. The ground conductivity was improved by using salty water and clay. The typical layout of the MT data acquisition is shown below (Figure 10.)

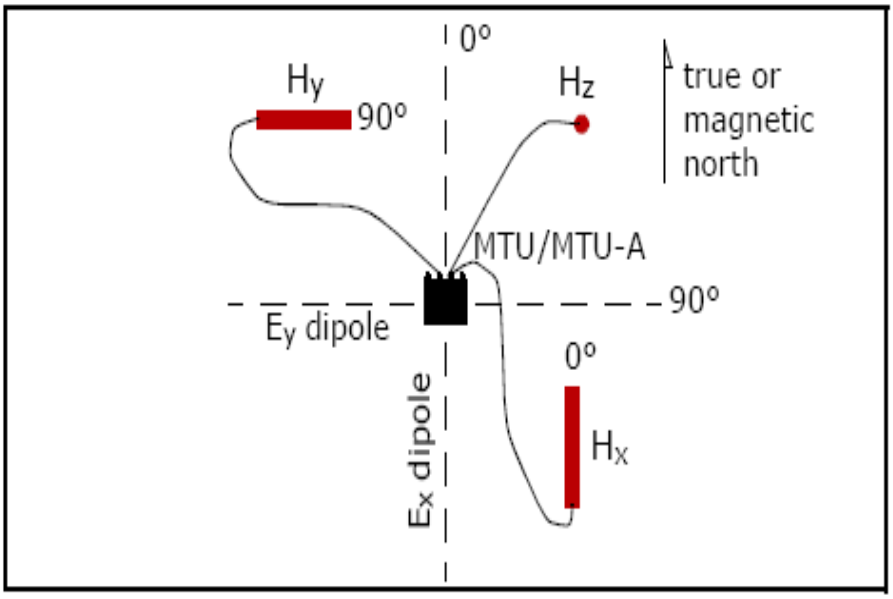

Figure 10 Layout of MT data acquisition. The magnetic sensors were usually located in the quadrants between the electric dipoles. The electric dipoles used were between 50-70m for this survey.

The ground contact resistance was generally between 1,000 -6,000 Ohms (manufacture recommendations should be less than 2,000 Ohms). The Alternate Current (AC) coupling was used with a high pass filter with a corner frequency of 0.005HZ which removes self potential from the electric dipoles. The background DC current due to electrochemical potentials was also generally high. Other sources of EM noise included the power lines wind noise and thunderstorms.

The Phoenix MTU-5A equipment was used in this field survey with MTC-50 coils used for acquiring low frequency data (400-0.0025 HZ). The telluric lines were typically between 50-70m. The lines were kept short to minimize the effects of AC from the power lines. In the course of the field work, longer telluric lines were tried out but they did not improve the data quality. The three MT loggers were deployed every day and

data acquired automatically overnight from 16.00 Hours to the following day at 9.00AM. This was done so as to acquire low frequency data. The electric field was measured by lead chloride porous pots. The magnetic sensors were buried about 30 cm below the surface to minimize the effect of wind. A total of 100 MT stations were acquired during the field campaigns in 2004 and 2005 (Figure). Roving remote reference stations were usually sited in areas to the periphery of the geothermal system away from power line noise

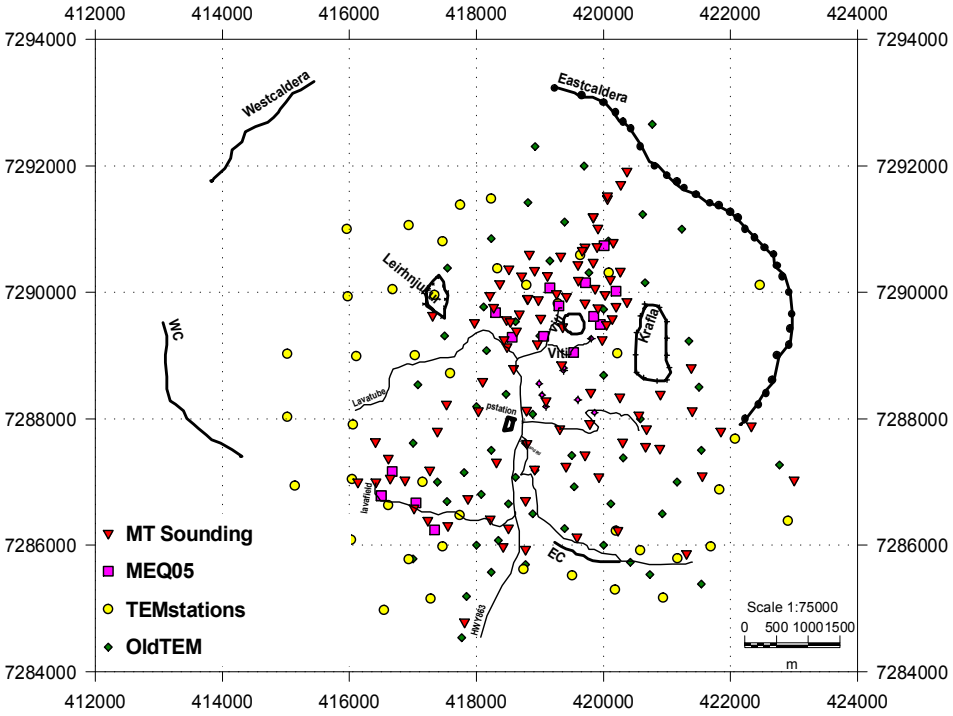

Figure 11 Location of MT soundings (red triangles) both for 2004 and 2005 field campaigns, TEM soundings (yellow circles and blue squares) and MEQ stations (purple squares) for 2005 campaign.

The data was automatically acquired over three frequency bands. The highest frequency band was sampled at 2,400 samples per second; the intermediate band was sampled at 150 samples per second while the low frequency band was sampled

continuously at 15 samples per second. The high frequency MT band covers the frequency range 317.645-0.3515625HZ, the intermediate band covers frequency range 0.2929688-0.0003433HZ and the low Band covers the frequency range 0.009155275-0.0000107. The acquisition of adequate low frequency data requires 18 hrs of data. In this survey we collected data for 16 hrs. In the second MT deployment of 2005, some data was acquired with the Phoenix AMT system with a sampling rate of 24000 for the highest frequency band, 2400 for the intermediate band and 150 for the low frequency band which corresponds to the 4^{th} band in the MT system. The data parameters for each site were recorded on data sheets and checked everyday during pick up of the equipment.

1.4.2 MT Data Processing

Data processing started with downloading data from the flash cards to the computer. The site parameters and acquisition times of the time series were then verified to ensure that the correct parameters are used. The next stage was to transform the time series to Fourier transforms which were then processed into crosspower estimates. The crosspowers were then edited to obtain resistivity and phase consistent data. These estimates were then converted to the standard Electronic Data Interchange (EDI) format.

The data was decomposed to the principal axis which is a mathematical decomposition commonly used in MT data interpretation to minimize the diagonal elements of the impedance tensor. TEM data was then used to correct for static shifts and then choose the TE and TM polarizations. After the decomposition, 1-D and 2-D

interpretation was carried out. The data was then used to plot resistivity sections and maps to assist in evaluating the hydrothermal systems.

1.4.3 MT data quality

As already pointed out, the MT data was affected by wind, power lines, seismic noise from movement of trees, thunderstorms and the high contact resistivity due to recent lava flow close to the surface. Precautions were taken during data acquisition to acquire the best data under the prevailing field conditions. Two measurements close to the power station could not used because of the effects of the electric fences with DC current. In a few instances, thunderstorms caused saturation on the electric and magnetic signals. The theoretical average depth of investigation in meters is given by the relationship $\nabla = 500\sqrt{T\rho_a}$ where T is the period in seconds and ρ_a is the average resistivity at the site. The depth of penetration at a period of 10 seconds (0.1 HZ) for a subsurface resistivity of 5-500 Ohm meters (Ωm) is about 1500-15,000 meters. We therefore concluded that the data was adequate for evaluating the depths of interest for determining the structures that control fluid circulation in a high temperature hydrothermal system.

1.4.4 Microearthquake data acquisition and Analysis

In the summer of 2004, Duke University deployed 20 new Geospace GS-1 seismometers at Krafla in NE Iceland at sites close to the MT measurements (see Figure 7). In the summer of 2005, Duke University deployed 15 more stations to the north and southwest of the power station. The GS-1 is a 3-component, 24-bit, 4-channel

seismometer designed for seismic exploration in a variety of terrains. The new seismometer is designed with a natural frequency of 1 Hertz (Hz), well suited for optimal response to microearthquakes.

The locations of the seismometers were determined with several features in mind. The first and most important requirement was that the network of stations be evenly distributed around the target area to the north of the power station. Transportation of the stations was convenient due to their compactness. A group of four was capable of transporting eight stations by foot over several kilometers with backpacks.

The MEQ data from the 2004 and 2005 field campaigns were carried out at predetermined locations to determine the microearthquake activity within the hydrothermal system to map the earthquake activity including in the two areas to the north and to the southwest. The design of the deployment took into account the fact than the 2004 deployment of the seismometers mainly to the southern part of the hydrothermal system recorded very few earth quakes. These two areas have been earmarked for exploration drilling. The location of the 2005 deployment was mainly to the north and south west (Figure 12)

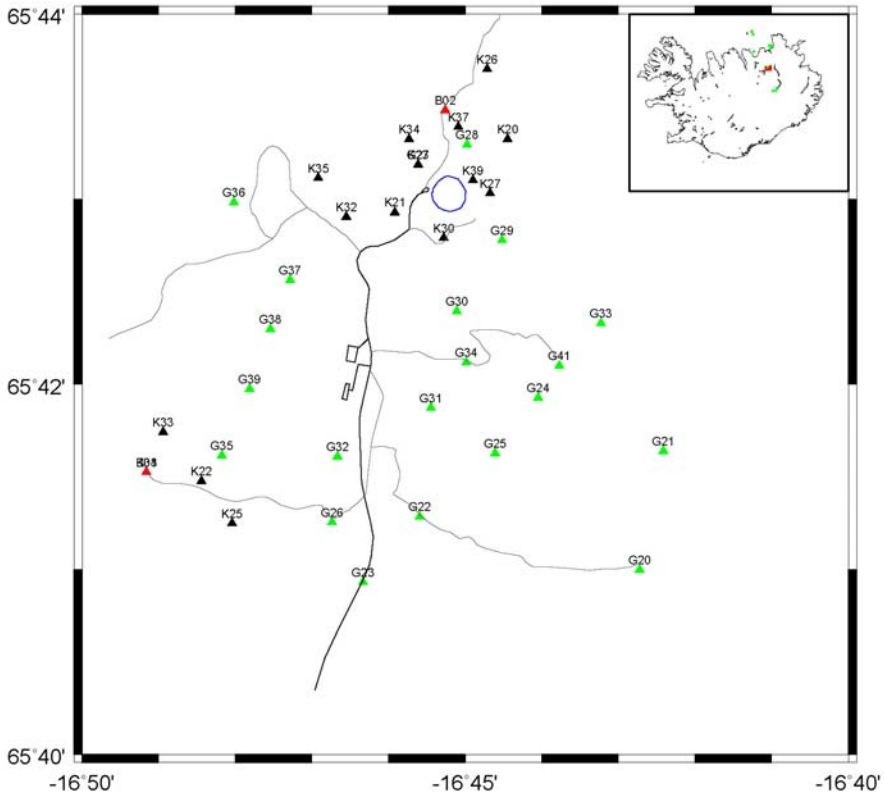

Figure 12 Location of MEQ stations from 2004 campaign (green triangles), 2005 campaign (black triangles) and two down hole seismometers (red triangles) installed after the 2005 field campaign

2. Resistivity imaging of a fault zone at the Krafla hydrothermal system

2.1 Transient electromagnetic (TEM) data modeling

In the TEM method, a time varying magnetic field is generated by a controlled artificial source. In this method, a loop of wire is placed on the ground and a constant current transmitted through it. The current is turned on and off at predetermined turnoff times. When the current is turned off, it creates a decaying magnetic field, which induces an electric current into the Earth. This electric current distribution induces a secondary magnetic field that decays with time and the rate of decay is measured at the centre of the loop by an induction coil.

The initial 1-D models for the TEM data from Krafla were generated by the temtd code written by (Arnasson) for a square loop with a receiver at the centre of the loop. The forward algorithm uses standard recursive relations to calculate the kernel function for the vertical magnetic field due to a grounded dipole with a transmitted harmonic current on the surface of a horizontally layered Earth (Árnason, 1989; Ward and Hohmann, 1987). The J1 Hankel transform for calculating the frequency domain response of the dipole is performed by using the J1 digital filter of Anderson (1979). The signal in the source-loop is accurately reproduced by dividing the sides of the loop into small segments so that the ratio of the distance from the receiver to the segment and the segment length is higher than 5:1.

The Fourier transform from frequency domain to the time domain is performed by using the sine-transform of the imaginary part of the frequency domain response

(Árnason, 1989). The sine-transform is performed using the sine digital filter of Anderson (1979). The induced transient voltage in the receiver is then calculated as the sum of the responses from successive current turn-on and turn-off time, starting from late time to early time. The transient response is calculated both as induced voltage and late time apparent resistivity as function of time. The apparent resistivity for the central loop as a function of distance and time as shown below:

$$\rho_a C(r,t) = \frac{\mu_0}{4\pi}\left[\frac{2\mu_0 A_r n_r A_s n_s}{5t^{5/2} V_C(r,t)}\right]^{2/3} \qquad 2.1$$

where μ_0 is the magnetic permeability, *Vc* is the measured voltage, A_r is the area of the receiver coil, n_r is the number of turns in the receiver coil, A_s is the area of the source loop, and n_s is the number of turns in source loop. Since the main objective of the study is to use the TEM data for static shifts in MT data, no further discussion is given on the theoretical formulation for TEM methods which are well established in the literature.

The inversion algorithm is carried out by the Levenberg-Marquardt non-linear least square inversion as described by Arnason (1989). The misfit function calculated from the root-mean-square difference between measured and calculated values (chisq), weighted by the standard deviation of the measured values. The damping is achieved by utilizing both on first derivatives and on second derivatives, to obtain smooth models. The actual function that is minimized is in this potential (ς) instead off the weighted root-mean-square misfit ($chisq$).

$$\varsigma = chisq + \alpha D_{S1} + \beta D_{S2} + \gamma D_{D1} + \delta D_{D2} \qquad 2.2$$

where D_{S1} and D_{S2} are the first and second order derivatives of log-

conductivities in the layered model and D_{D1} and D_{D2} are the first and second order derivatives of the logarithms of the ratios of layer depths. The coefficients α,β, γ and δ are the relative contributions of the different damping terms and in this case values of 0.1 were used. The half space or basement depth was fixed at 1500 while the number of layers for the initial model depended on the data but in most cases it was fixed at 5.

The TEM data for Krafla was acquired by the PROTEM receivers from Geonics while the data from Longonot was acquired by the Zonge GDP-32 receivers respectively. The averages and standard deviations for repeated transient voltage measurements are calculated for late time apparent resistivity as a function of time. The Occam and layered inversions were then performed by the program temtd written by (Arnasson, 2004).

The Occam one-dimensional inversion of electromagnetic data generally refers the data interpretation with many layers with fixed thicknesses and variable resistivities. The resistivity values vary with little contrast between layers. The initial model can either be automatically generated with constant initial reisistivities or by specifying an initial model file and the resistivities of the layers.

The smoothness of the model is specified by the $-R\alpha$ and $-S\beta$ options, where α and β are the parameters that control the damping on first and second derivatives of the conductivities with depth. The data was interpreted also interpreted for layer thickness and resistivity to obtain a model to use with the MT data to correct for static shifts. In places where data was not available for the old TEM soundings, the available 1-

D models from the report by ISOR were used to generate one 1-D models in the WinGlink program.

2.2 Magnetotelluric (MT) data modeling and interpretation

2.2.1 Theoretical Formulation of Magnetotelluric (MT) Method

The theory of Magnetotelluric method used in resistivity studies is based on the Maxwell's equations which relate electric and magnetic fields. These equations are routinely used together with experimentally determined constitutive equations to evaluate the resistivity structure at a measurement location. Maxwell's equations are given below:

$$\nabla \times E = -\frac{\partial B}{\partial t} \qquad 2.3$$

$$\nabla \times H = J + \frac{\partial D}{\partial t} \qquad 2.4$$

$$\nabla . B = 0 \qquad 2.5$$

$\nabla . D = \Theta$ (if we assume no charges accumulate, then Θ tends to zero) 2.6

where **E** is the electric field vector ($Volts/meter$), **H** is the magnetic field vector ($Amperes/meter$), **B** is the induction field vector (Wb/m^2 Tesla (T)- which is equal to the magnitude of the magnetic field vector necessary to produce a force of one Newton on a charge of one coulomb moving perpendicular to the direction of the magnetic field vector

with a velocity of one meter per second), D is the displacement vector (C/m^2 Coulomb is the amount of electric charge (quantity of electricity) carried by a current of 1 ampere flowing for 1 second. It is also about 6.241506×10^{18} times the charge of an electron. **J** is the current density, Θ is the electric charge density C/m^3 . In conductive materials, charge density decays very rapidly and therefore it is usually assumed that no charges accumulates in the materials. However, for inhomogeneous regions, a charge density accumulates at the interface between two different media.

The constitutive equations shown below are useful in deriving Maxwell's equations. These relationships assume that the fields are not dependent on pressure or temperature.

$$D = \varepsilon.E \qquad 2.7$$

$$B = \mu.H \qquad 2.8$$

$J = \sigma.E$ (Ohm's law relating current density to electric field intensity) 2.9

where ε is the electrical permittivity ($\varepsilon_o = 8.9\times10^{-12} F.m^{-1}$ in air), μ is the magnetic permeability ($\mu_o = 4\times\pi\times10^{-7} H/m$ in air), σ is the electric conductivity which is equivalent to the reciprocal of the resistivity, $1/\rho$. The conductivity is measured in siemens per meter while the resistivity is measured in ohms per meter. The Maxwell's

equations are usually simplified by assuming that the resistivities values in the earth are much higher than the variation in electrical permittivity and magnetic permeability.

This study focuses mainly on the conductivity distribution that might be an indicator of high fracture porosity zones for locating high production wells. The derivation of the equations for application of Magnetotelluric methods are not exhaustively analyzed in this text. The normal equations found in textbooks will be utilized to study and map structures.

2.2.2 Electromagnetic Induction in the Earth

In the existing publications, the most common approach used to determine the electric structure is the assumption of plane harmonic electromagnetic waves (Cagniard, 1953). The MT diffusion equation is derived by taking the curl of equations 2.3 and 2.4 above and using the constitutive equations 2.7 to 2.9.

$$\nabla \times \nabla \times E = -\frac{\partial(\nabla \times B)}{\partial t} = -\mu \frac{\partial(\nabla \times H)}{\partial t} = -\mu \frac{\partial(J + \frac{\partial D}{\partial t})}{\partial t} = -\mu \frac{\partial(\sigma . E + \frac{\partial D}{\partial t})}{\partial t} \qquad 2.10$$

The relationship on the left side of equation 2.10 can be evaluated from the relationship:

$$\nabla \times \nabla \times E = \nabla(\nabla . E) - \nabla^2 E \qquad 2.11$$

$$\nabla(\nabla.E) - \nabla^2 E = -\mu \frac{\partial(\sigma.E + \frac{\partial D}{\partial t})}{\partial t} = -\mu \frac{\partial(\sigma.E + \varepsilon \frac{\partial E}{\partial t})}{\partial t} \qquad 2.12$$

From equation 2.9 $\nabla.E = (\frac{\nabla.D}{\varepsilon})$ and $\nabla.D$=0 so that equation 2.12 can then be expressed as:

$$\nabla^2 E = -\mu\sigma \frac{\partial E}{\partial t} - \mu\varepsilon \frac{\partial^2 E}{\partial t^2} \qquad 2.13$$

The MT measurements are made in time domain by sampling the variations in the EM fields at specified frequency windows (determined by equipment type and manufacturer). A Fourier Transform is usually applied to the time domain electromagnetic variations E(t) and H(t) to determine their amplitudes as a function of angular frequency ($\omega = 2\pi f$). If the primary EM field has a harmonic time variation in the form $E = E_0 e^{-iwt}$, then taking the derivative of equation 10 can be expressed as:

$$\nabla^2 E = -(-\mu\sigma i\omega E + i^2 \mu\varepsilon\omega^2 E) = -(\mu\varepsilon\omega^2 - i\omega\mu\sigma)E = -k^2.E \qquad 2.14$$

where $\kappa = (\mu\varepsilon\omega^2 - i\omega\mu\sigma)^{1/2}$ which is the complex wave number.

A similar expression can be derived for the magnetic field so that:

$$\nabla^2 H = -\mu\sigma\frac{\partial H}{\partial t} - \mu\varepsilon\frac{\partial^2 H}{\partial t^2} \qquad 2.15$$

$$\nabla^2 H = -(-\mu\sigma i\omega H + i^2\mu\varepsilon\omega^2 H) = -(\mu\varepsilon\omega^2 - i\omega\mu\sigma)H = -k^2.H \qquad 2.16$$

Equations 2.15 and 2.16 are of the form $\nabla^2 X + k^2 X = 0$ where X is either the magnetic (H) or electric field (E). These are the wave equations in the frequency domain (commonly known as Helmholtz equations in E and H). The conductivity of rocks usually ranges from 10,000 to 0.1 mS/m (0.1Ωm to 10,000Ωm) while ε is in the order of $8.9\times10^{-12}F.m^{-1}$ and therefore $\mu\varepsilon\omega^2 \ll \mu\sigma\omega$ for most earth materials where displacement currents are much smaller than conduction currents. The MT method also uses frequencies less than 100,000Hz.

The electric conductivity **σ** is a tensor that relates two vectors (Keller 1988). The two vectors are the electric field intensity **E** and current density **J**. In Cartesian coordinates, the conductivity has the form:

$$\sigma = \begin{vmatrix} \sigma_{xx} & \sigma_{xy} & \sigma_{xz} \\ \sigma_{yx} & \sigma_{yy} & \sigma_{yz} \\ \sigma_{zx} & \sigma_{zy} & \sigma_{zz} \end{vmatrix} \qquad 2.17$$

This conductivity tensor is usually simplified by choosing two coordinate directions which define the direction of maximum and minimum conductivity. These

directions are known as the principal directions of the conductivity tensor. Equation 2.17 then can be expressed as:

$$\sigma = \begin{vmatrix} \sigma_{xx} & 0 & 0 \\ 0 & \sigma_{yy} & 0 \\ 0 & 0 & \sigma_{zz} \end{vmatrix} \qquad 2.18$$

2.2.3 1-D Formulation

The solution of the diffusion equation can be simplified by assuming plane waves incident on the earth's surface (Cagniard, 1953). The plane wave relationship can be used to evaluate the induction in 1-D structures by assuming the change in conductivity with depth. We consider a Cartesian coordinate system where x is positive north, y is positive east and z is positive down and z=0 is at the surface of the earth as shown below.

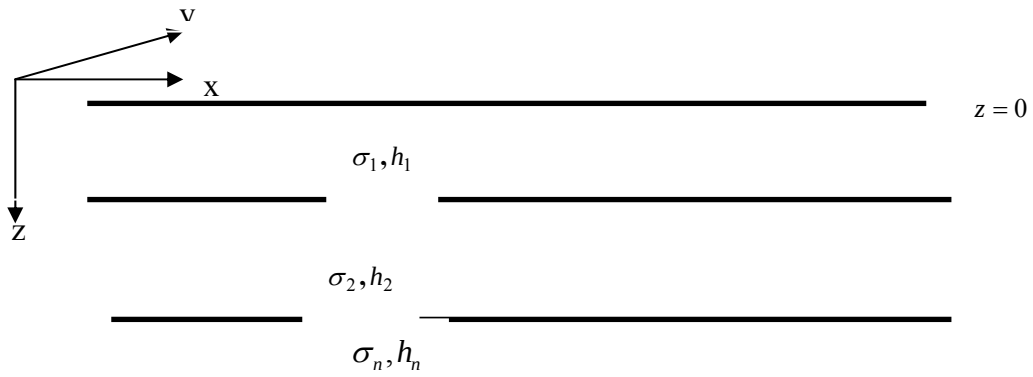

Figure 13 1-D resistivity model with n layers and varying conductivity with depth only. Resistivity within each layer does not change in the y and x axis.

For the normal incident plane wave in one dimensional earth model, the resistivity or conductivity is assumed to vary with depth in the z direction ($\sigma = \sigma_z$). The induced electromagnetic field is assumed to be parallel to the earth's surface. If the horizontal electric field is only in the x direction the orthogonal horizontal magnetic field is in the y direction, then ($E_y = E_z = 0$) and equation 2.15 and 2.16 can be expressed as:

$$\frac{\partial^2 E_x}{\partial z^2} = i\omega\mu\sigma_z E_x \qquad 2.19$$

$$\frac{\partial^2 H_y}{\partial z^2} = i\omega\mu\sigma_z H_y \qquad 2.20$$

For a harmonic time varying electromagnetic field, the general solution of the second order differential equation has been exhaustively discussed by Ward and Hohmann (1988) and is expressed as:

$$E_x = Ae^{(kz-iwt)} + E_0^{-}e^{i(kz+wt)} \qquad 2.21$$

and

$$H = H_0^{+}e^{-i(kz-wt)} + H_0^{-}e^{i(kz+wt)} \qquad 2.22$$

where k is complex and can be expressed in terms of real α and β as;

$$k = \alpha - i\beta \qquad 2.23$$

$$\alpha = \omega\left\{\frac{\mu\varepsilon}{2}\left[\left(1+\frac{\sigma^2}{\varepsilon^2\omega^2}\right)^{1/2}+1\right]\right\}^{1/2} \qquad 2.24$$

$$\beta = \omega \left\{ \frac{\mu\varepsilon}{2} \left[\left(1 + \frac{\sigma^2}{\varepsilon^2 \omega^2} \right)^{1/2} - 1 \right] \right\}^{1/2} \qquad 2.25$$

When displacement currents are ignored α and β are equal and are defined (Ward and Hoffman, 1988) by:

$$\alpha = \beta = \sqrt{\frac{\omega\mu\sigma}{2}} \qquad 2.26$$

For EM signals that decay in the positive z direction, the solutions for equations 2.21 and 2.22 can be written as:

$$E = E_0{}^{+} e^{-i\alpha z} e^{-\beta z} e^{i\omega t}, \qquad 2.27$$

$$H = H_0{}^{+} e^{-i\alpha z} e^{-\beta z} e^{i\omega t} \qquad 2.28$$

If the subsurface is 2D, the EM fields are usually polarized into two modes referred to as TE-mode when the E fields are parallel to the direction of strike and the TM-mode when the H-field is parallel to the strike direction. When the MT polarization is in the direction of the regional strike (Figure 12), it is assumed that there will be no conductivity variation in this direction and the resistivity varies only with depth and along one lateral axis (2-D). In this case the EM fields decouple into 2 distinct polarizations, the TE (transverse electric) and TM (transverse magnetic). During data acquisition, the EM measurements are usually made in the NS and EW directions which

do not always correspond to the direction of strike. MT data interpretation therefore involves the decomposition of the EM fields so that data can be reduced to a form that satisfies the 2-D assumptions for the commonly used 2D interpretation methods.

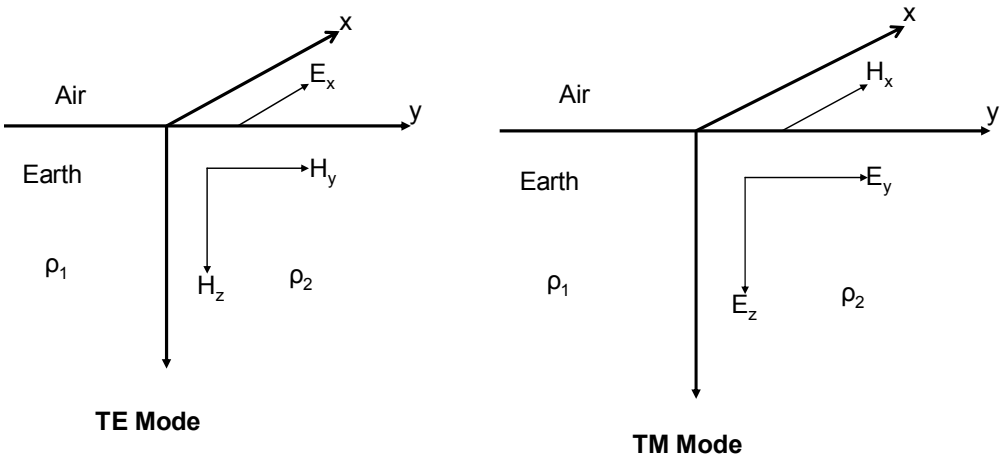

Figure 14 The effect of 2 dimensional half space. In the TE mode, the current is polarized in the direction of strike X creating associated magnetic fields in the Y and Z directions. IN TM mode the magnetic field is along strike direction generating associated magnetic fields in the Y and Z directions

2.2.4 Is the Seismic Analogue feasible?

In the initial stages of the development of the MT methods, considerable efforts were made to use the "image theory" by considering the "reflection of electromagnetic waves" in the earth. The pioneering publications include Yost (1952) and Orsinger and Van Nostrad (1954).

Equations 2.14 and 2.15 are second order differential equations (Chauveau, 1967) which have a similar form to the seismic acoustic wave equation

$$\nabla^2 U(r,t) = \frac{1}{V^2}\frac{\partial^2 U(r,t)}{\partial t^2} \qquad 2.29$$

where $U(r,t)$ is the elastic displacement and V is the wave velocity of the medium.

Several authors have made attempts to find the correlation of these equations with similar forms in seismic methods. The approach of Lee et al. (1987) and Levy et al. (1988) to apply seismic reflection ideas to solve the Magnetotelluric inversion problem is considered. These computations involve the principal of two-way travel time and reflection coefficients. This approach was found hard to implement and therefore it is not discussed further.

2.2.5 Telluric and Magnetic Tensor decomposition

In the MT methods, the measured impedances can be affected by DC-currents usually known as galvanic distortions which result from either local conductive structures or 3-D structures. These distortions pose a challenge to the modeling of the subsurface structures from surface measurements of MT data. In most of the regional studies, the effects of the local distortions are usually removed to recover the regional structure. In the case of mapping hydrothermal systems, the local distortions might give good information on the structure of the hydrothermal system.

In the presence of telluric distortions, Groom and Bailey (1989) proposed that the distortion matrix D_e can be separated into three matrices and a real number **g** which is a scaling of the measured apparent resistivity. The shift is caused by polarization of the EM fields by local resistivity contrasts at the scale of the measurement dipole (in this study

50-70M) that lead to a constant vertical displacement of the MT apparent resistivity curve on a log scale at all frequencies. To sort distortions on the MT data, different decomposition techniques (Groom and Bailey, 1991, Torquil Smith, 1995) are used to correct 3-D impedance for statics and non 2-D distortions. For the case of a 2-D regional structure, the measured impedance Z_o can expressed as a function of the regional 2-D impedance Z_r as shown below:

$$Z_o = D_e Z_r = (gTSA)Z_r \tag{2.30}$$

$$T = \frac{1}{\sqrt{1+t^2}}\begin{bmatrix} 1 & t \\ t & 1 \end{bmatrix} \tag{2.31}$$

$$S = \frac{1}{\sqrt{1+e^2}}\begin{bmatrix} 1 & e \\ e & 1 \end{bmatrix} \tag{2.32}$$

T is the twist and **S** is the shear and $t = \tan(\beta_t)$ which is the twist parameter that defines a clockwise electrical field rotation through an angle β_t caused by DC-currents. The shear parameter $e = \tan(\beta_e)$ deflects the electric field by an angle β_e in a clockwise position from the x-axis and anticlockwise from the y-axis (Groom and Bailey 1989). The shear represents deformation from the principal axis.

From this discussion, we will assume that in hydrothermal systems, fluid filled cracks cause polarization which is also recorded by microearthquake monitoring stations. The shear (S) in MT therefore represents the anisotropy or splitting tensor resulting in the stretching of the electric fields in the x and y directions by different factors. Groom and Bailey (1989) have shown that the anisotropy (A) which is produced by small scale

2-D or 3-D bodies and the gain factor **g** cannot be determined uniquely due to equivalence.

$$A = \frac{1}{\sqrt{1+s^2}}\begin{bmatrix} 1+s & 0 \\ 0 & 1-s \end{bmatrix} \qquad 2.33$$

In this study the TEM data is used to remove the static shifts before carrying out inversion of the MT data to determine 1-D and 2-D resistivity structures. We further assume that the shear and twist are equivalent to the shear wave splitting in the microearthquake data. While we acknowledge that there magnitude might be different, we postulate that both data sets are affected by the changes in the acoustic and resistivity impedances.

2.2.6 Induction arrows

In the 2-D case the magnetic field from the TE polarization indicate the lateral variations in conductivity. The vertical (B_z) and horizontal magnetic fields (B_x, B_y) in the x-direction (north-south) and y-direction (east-west) are related through the magnetic transfer functions known as the tipper T_x and T_y as shown below:

$$B_z = T_x B_x + T_y B_y \qquad 2.34$$

B_z is a secondary field and for 1-D case it is zero. The tipper gives an indication of the lateral changes in resistivity and is usually represented as vectors known as induction arrows (Parkinson, 1959) as shown below:

$$T = T_x n_x + T_y n_y \qquad 2.35$$

In this case n_x and n_y are unit vectors in the x and y directions. The tipper is the separated into frequency dependent real (R) and imaginary (I) parts. The real part can be represented as pointing either away or towards the conductor. The length of the induction arrows (L) and angle (θ) with respect to the X-axis are expressed as shown below:

$$L = \sqrt{(R,I(T_x)^2 + R,I(T_y)^2)}, \text{ and } \theta = \arctan\frac{R,I(T_y)}{R,I(T_x)} \qquad 2.36$$

In the case of 2-D, the direction of the induction arrow is perpendicular to orientation of regional strike.

2.3 Joint Inversion of MT and TEM data

The initial TEM models generated by the program temtd (described above) were input into the WinGlink program (which is used extensively both in industry and academic research in Magnetotelluric studies). The equivalent MT model of phase and resistivity generated from TEM data was then used to correct for static shifts in the MT data. In most cases the TEM model fitted the TE mode of the MT data very well.

Based on the evaluations by Berdichevsky et al. 1998, both the TE and TM modes provide complimentary information on shallow and deep structures. The TE mode is more sensitive to deep structures and more robust to 3-D effects caused by resistive structures. The TM mode is more sensitive to near surface structures and is affected by the static shift problem more than the TE mode. Based on this reasoning, this study used Time Domain Electromagnetic (TEM) data to correct for static shifts which are caused by an electric field from boundary charges on near surface inhomogeneities [*Pellerin and Hohmann*, 1990]. The static shift represents a scalar multiplier of the original data and in

the case where there is no shift the multiplier is equal to 1. The use of TEM method to correct for static shifts is based on the assumption that TEM data are less affected by static shift errors. The MT data was evaluated for static shifts to determine the amount of shift before carrying out 1-D and 2-D MT data interpretation. The shifts for all the sites were determined for all the MT stations (Figure 14). The TM shifts are generally higher than the TE shifts conforming to the interpretation that the TM mode is more affected by lateral resistivity changes.

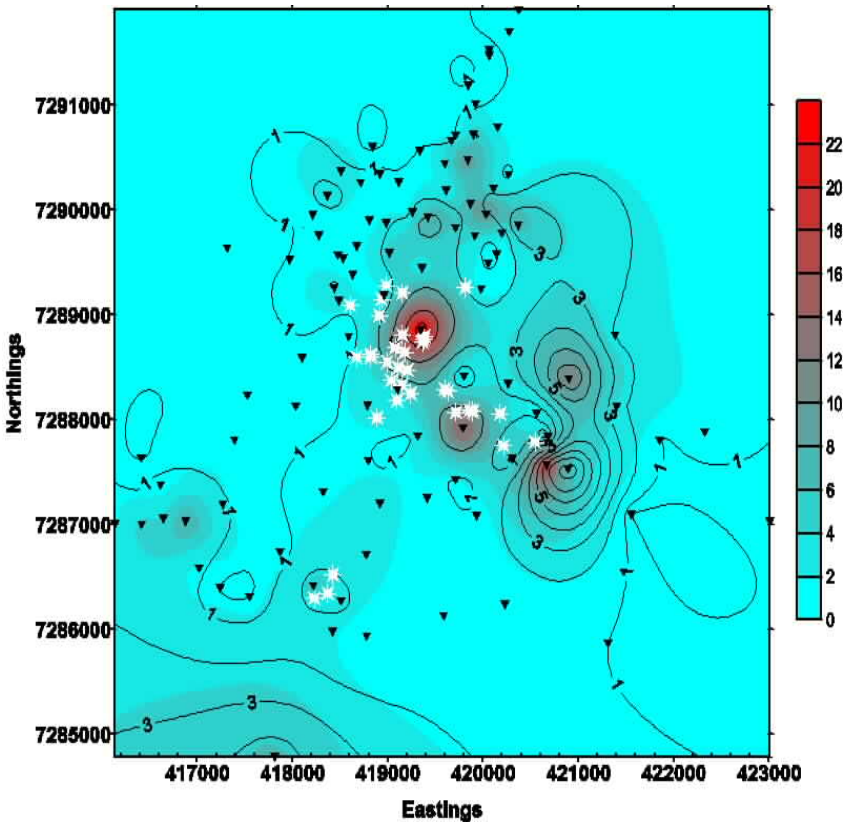

Figure 15 Distribution of TE mode (superimposed contours) and TM mode (colored map) shifts for data from the 2004 and 2005 field campaigns (black triangles)

The shifts are highest within the area covered by surface hydrothermal alterations within the geothermal field. The TE mode shifts (less than 5) are lower than the TM mode shifts which at some sites are more than 20. The shifts in the areas outside the hydrothermal system are generally low for both TE and TM mode indicating near 1-D resistivity distribution even in areas close to fracture zones like at sounding KMT47 (Figure 15) which was acquired across a fracture but shows very small shift. The EW dipole crossed the fracture zone while the NS dipole ran along the fracture. At high frequencies, there data shows no shift.

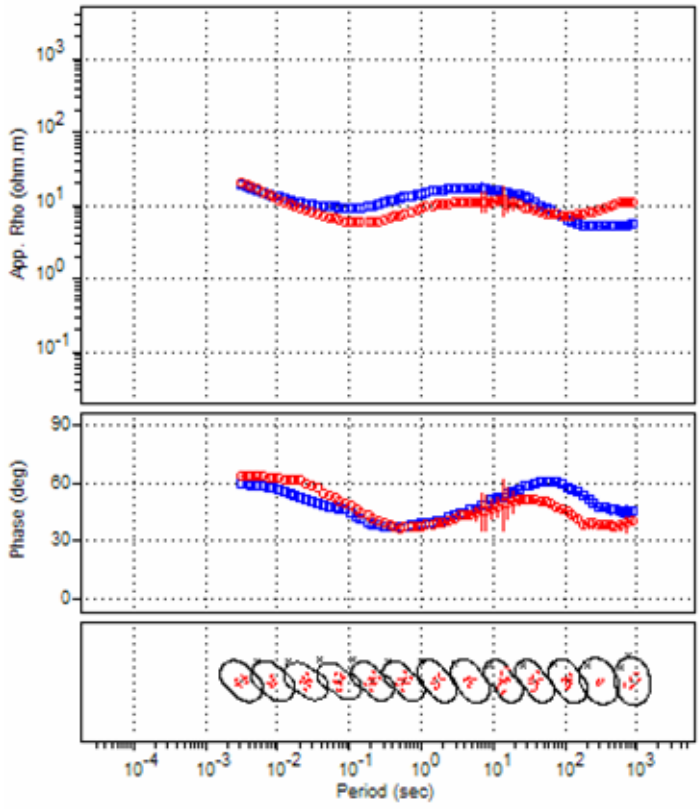

Figure 16 Plot of apparent resistivity, phase and polarization for site KMT 47. The upper panel shows the apparent resistivity for the TE mode (blue circles) and the TM mode (red circles). The middle panel shows the phase and the bottom panel shows the polarization direction which is in the NW-SE direction at almost all frequencies.

The shifts have a spatial variation across the area of study but are independent of topography (Figure 16). The shifts are generally low but at some sites the TM mode shift is quiet high (by a factor of more than 10). This seems to confirm that the TM mode is affected by the static shift more than the TE mode. From the plot of elevation and shift, there is some evidence of clustering around the same elevation indicating that the shifts are same for regions with similar elevations. The shifts are independent of the elevation but MT soundings in the same area have the same shift.

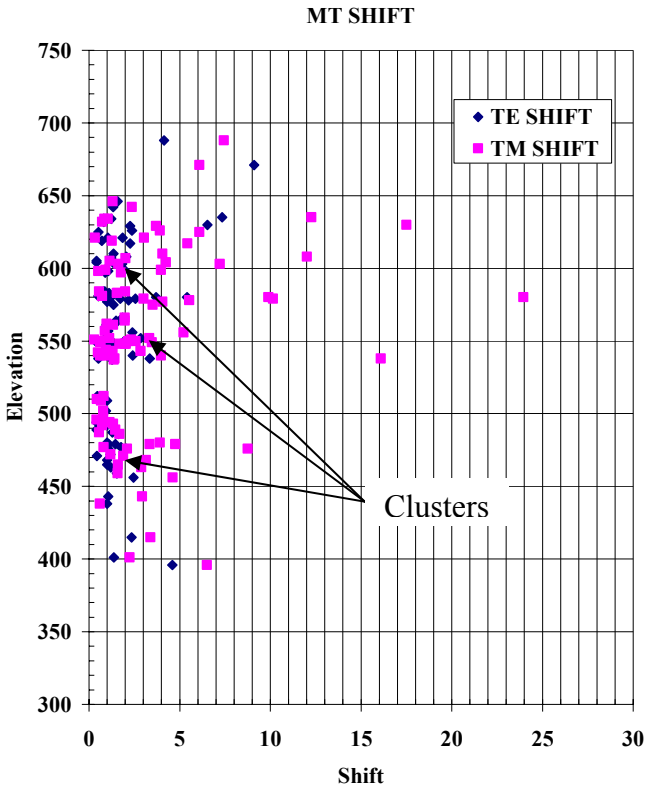

Figure 17 Distribution of TE mode and TM mode shifts against elevation for all the MT data for the 2004 and 2005 data. The shifts occur in clusters at sites with similar elevation indicating sites in the same are have similar shifts. The shifts are independent of elevation

The dimensionality of the data was also analyzed by determining the ellipticity and skew. Ellipticity (E) relates the magnitude of the difference of the rotated diagonal elements divided by the sum of the rotated off diagonal elements of the rotated impedance tensor as defined by Ranganayaki (1984) as shown below.

$$E = \frac{\left|Z_{xx}^{'} - Z^{'}_{yy}\right|}{\left|Z_{xy}^{'} + Z'_{yx}\right|} \qquad 2.37$$

The Ellipticity varies with frequency and it is high at some sites both at high and low frequency. As pointed out Ranganayaki (1984), Ellipticity can be affected by 3D resistivity structures and even though the TE and TM mode resistivity shows one dimension, the ellipticity can still be high (>0.2). From the example given below from site KMT 47, ellipticity is high at frequencies between 320-90 Hz even though the resistivity looks 1-D. In this case the ***skew*** which is defined as the dimensionless parameter that is the measure of how the measurements vary from an ideal 2-D model as defined by Swift (1967) is used as a measure of 1-D dimensions.

$$s = \frac{\left|Z_{xx} + Z_{yy}\right|}{\left|Z_{xy} - Z_{yx}\right|} \qquad 2.38$$

In the example for station KMT 47 the ***skew*** is very low (<0.2) even at low frequencies indicating that the structure is close to either 1-D or 2-D. At site KMT 55 (Figure 18), the skew and ellipticity is very low despite the large split in the MT resistivity data at about 10 Hz. Based on this analysis, our interpretation is that the near surface layers are 1-D dimension and the splitting in the MT data is caused by contrasts

in impedance at depth and not lateral changes. This interpretation is used together with shear wave splitting to analyze anisotropy.

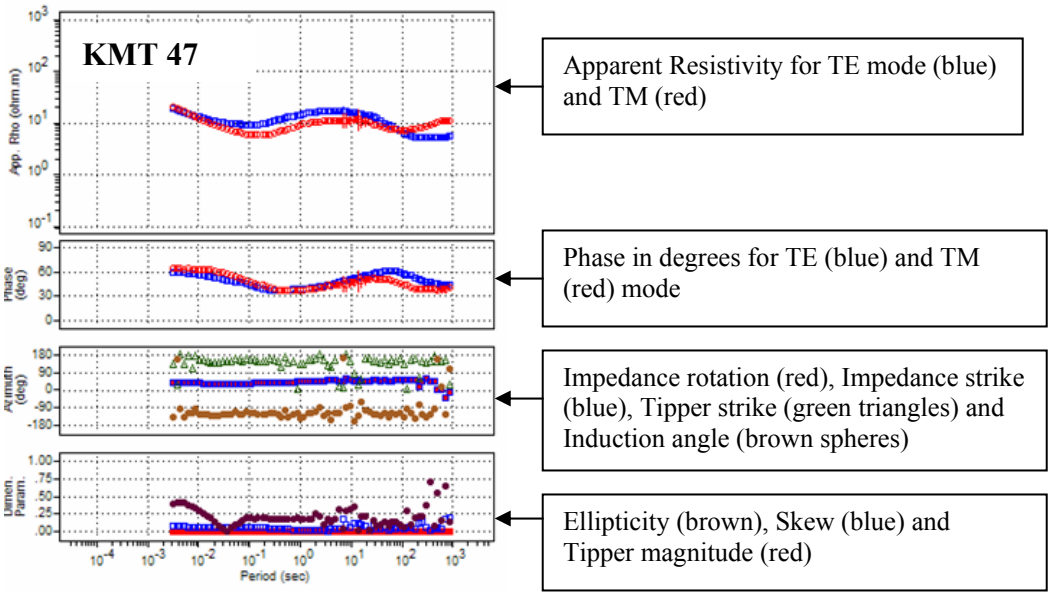

Figure 18 Apparent resistivity, phase, azimuths and dimensional parameters of site KMT 47. The resistivity shows near 1-D structures.

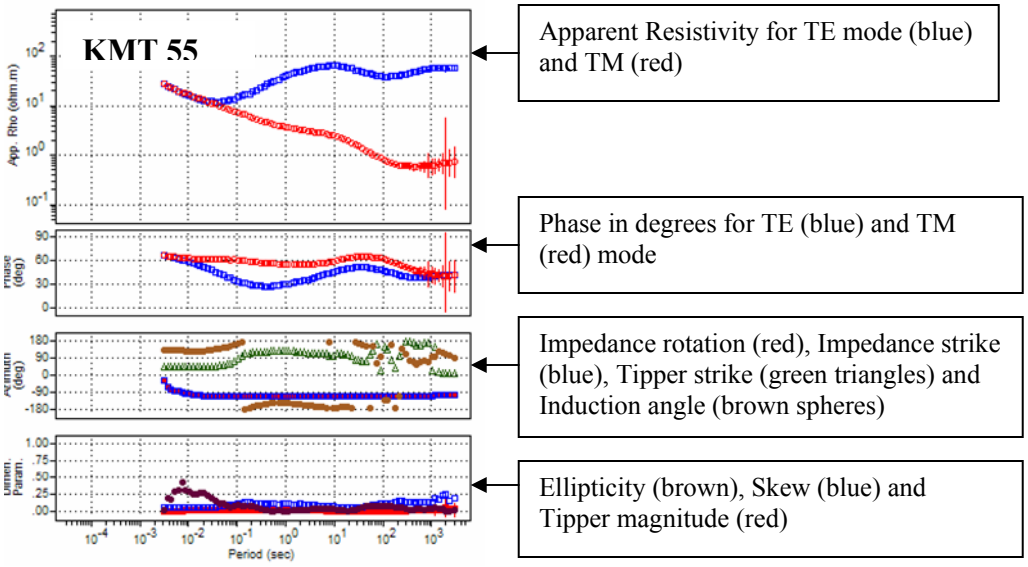

Figure 19 Apparent resistivity, phase, azimuths and dimensional parameters at site KMT 55. The resistivity shows splitting at 0.1 seconds with a change in induction direction and tipper strike.

2.4 Analysis of Depth of penetration

In general as already shown, the depth of penetration of EM fields within the earth for plane waves for orthogonal electric and magnetic fields in the frequency domain can be expressed in terms of conductivity σ, and magnetic permeability of μ_o and the frequency [*Nabighian*, 1979] by the equation below.

$$\delta_{FD} = \sqrt{\frac{2}{\mu_0 \sigma \omega}} \qquad 2.39$$

The highest frequency (ω) range for data acquisition 10,400Hz for the AMT data and 320 Hz for MT data. The lowest frequency for the MT data is 0.001Hz. These frequency ranges were used to plot the penetration depths for one skin depth for the effective resistivity ranging from 1to 100,000Ωm. In this case the effective conductivity is defined as the mean conductivity at each depth (Jain, 1966) as shown below:

$$\sigma_{mean}(z) = \frac{C(z)}{z} \text{ and } C(z) = \int_0^z \sigma(z) dz \qquad 2.40$$

where $C(z)$ is the cumulative conductance

The plot for 10,400Hz shows the shallowest depth of penetration at different effective resistivity. This plot shows that the lower the resistivity, the shallow the penetration depth. This means for a given frequency, in areas with low resistivity within the hydrothermal system, the depth of penetration is shallower than in areas with high resistivity (Figure 19).

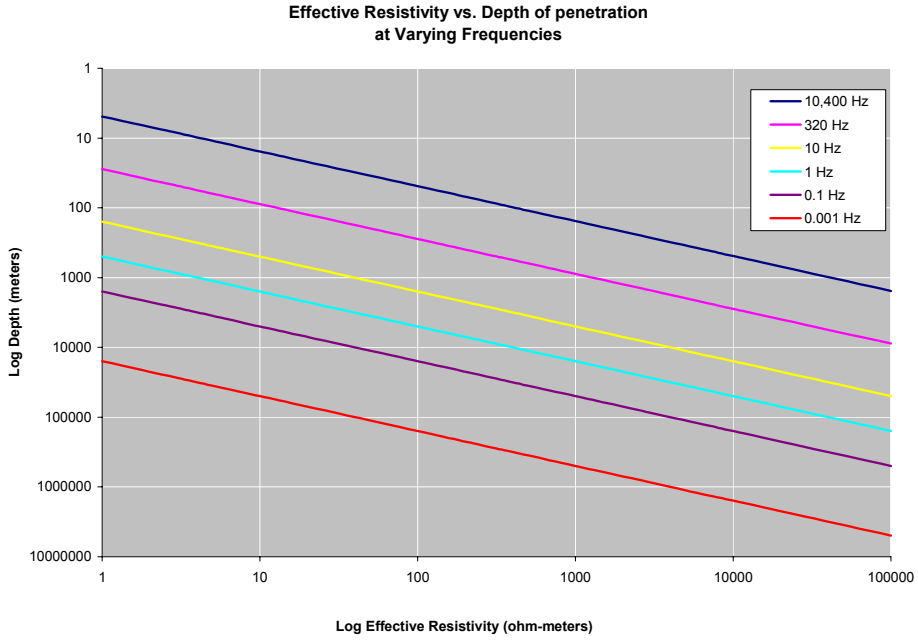

Figure 20 Depth of penetration plotted against resistivity. At any given effective resistivity, the depth of penetration is shallower for the high frequency.

The time-domain diffusion depth for TEM is proportional to the square root of time [*Spies*, 1989] as shown below.

$$\delta_{TD} = \sqrt{\frac{2t}{\mu_0 \sigma}} \qquad 2.41$$

where t is time. Another approximation for investigating the equivalent depth of penetration for both MT and TEM can be obtained by equating frequency with the reciprocal of the time for TEM [*Sternberg et al.*, 1988] as shown below.

$$f(HZ) \approx \frac{194}{t(ms)} \qquad 2.42$$

The ISOR TEM data used has a maximum time of 96ms at a sampling frequency of 2.5HZ. This gives an equivalent overlap MT frequency above 2.02HZ.

After initial editing of the MT data, TEM data acquired by the Icelandic Geosurvey (ISOR) at Krafla was used to correct for the static shifts. 1-D models were generated from the collocated data using the 1-D inversion program developed Arnasson (2005). The 1-D models were then imported into the WinGlink MT data interpretation software and used to correct for static shifts. The use of TEM data assumes similar overlapping depths of penetration for both TEM and MT data. The depth of penetration for both MT and TEM overlap depending on the frequency and time [*Spies*, 1989].

An example of the TEM data fit for site KMT 55 is shown below. In this case the TEM data fits the TE resistivity mode very well. The phase fits well at shallow depths but shifts at lower frequencies. This may be attributed to either 2-D effects or the anisotropy that cause the shift in the MT data. Some of the measurements show strong frequency dependences polarization.

2.5 1-D Models

The 1-D interpretation was carried out both for layered and Occam's inversion using the MT invariant (which is the geometric mean of the TE and TM modes) for the entire MT data set after rotation to the principal axes. The inversion was carried out by specifying an initial model and an RMS of less than 5% for both resistivity and phase of the MT data. In Occam's 1-D models consisted of 40 layers of constant thickness on the log scale. Occam's concept is simple where the objective s to minimize or maximize a penalty on the model, **m**, so that the model fits the observed data to within some reasonable level of misfit, X^2. A Lagrange multiplier formulation is used for an unconstrained functional **U** is minimized.

$$U = R(m) + \mu^{\{-1\}} X(m)$$

The first term, R (m) is a functional of the model which returns a property which is returns the function to penalize. The term X (m) measures the misfit obtained by the model. The relative importance of the model penalty function and the misfit is controlled by the Lagrange multiplier μ^{-1}. μ is chosen so that X (m) = X^2, which is the target misfit. 50 inversions were carried out at every site and the data used to construct maps and cross sections to evaluate the spatial variation in resistivity in the study area. An example of 1-D invariant model for (Figure 20) KMT 37 is shown below:

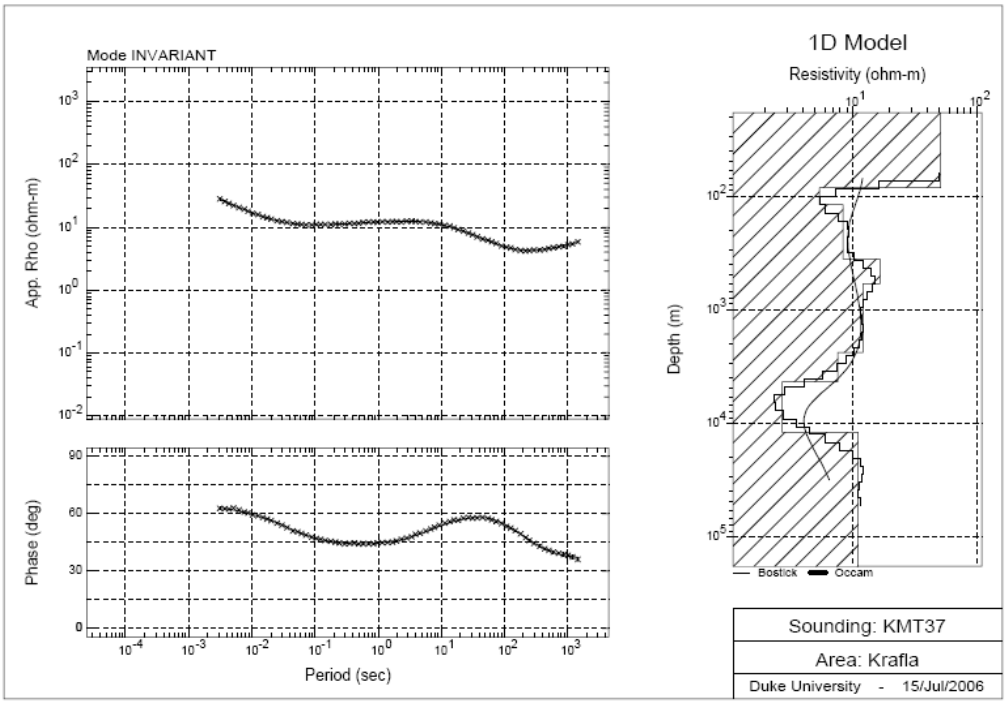

Figure 21 Invariant resistivity model of site KMT 37 indicating a general 5 layer model. The panel on the top left shows the variation of apparent resistivity with period in seconds. The panel on the bottom left shows the changes in phase with period in seconds. The panel on the right shows the variation in resistivity with depth for the 1-D layered and Occam's models

The models generally show a resistive near surface layer, a second conductive layer, a third resistive layer, a fourth conductive layer and a resistive half-space. The results of Occam's inversion were used to construct 1-D stitched sections for the invariant resistivity (Figure 22). The models show a narrow zone of low resistivity which is about 3 km wide at a depth of 3000 m. This low resistivity zone extends southwards along two profiles. The resistivity however increases southwards indicating a boundary of the hydrothermal system. The low resistivity zone is wider and depth and narrower towards the surface where it connects to a horizontal low resistivity between 0

to -500 mbsl that seems to dip to the SSW along the profiles. This layer does not extent to the north of the profile indicating the possibility of a sharp resistivity boundary.

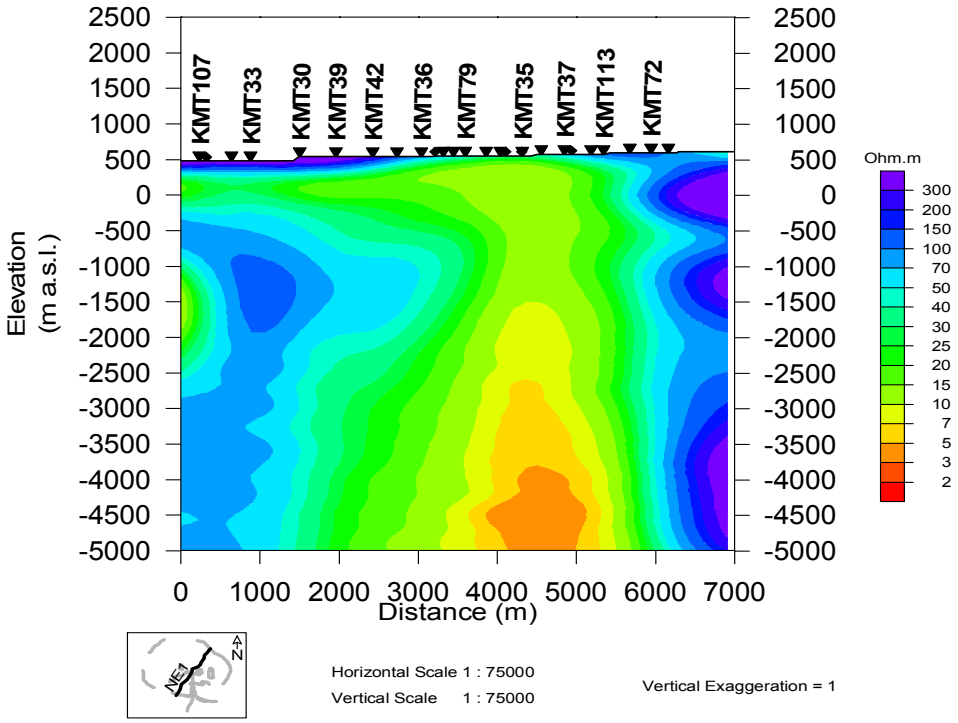

Figure 22 1-D stitched model from the Invariant resistivity data along a NE-SW profile across the Krafla hydrothermal area. Low resistivity is found in the middle of the profile with high resistivity on both sides of the low resistivity zone. The low resistivity zone occurs between KMT36 and KMT 113 and is centered on site KMT35.

2.6 1-D Resistivity Maps

Resistivity maps were prepared from the results of 1-D Occam's models to show the spatial distribution of resistivity at fixed elevations. The maps show that resistivity varies considerably both laterally and with depth. The low resistivity zone is mainly found to the north of the power station with a NW-SE trend. This zone of low resistivity

coincides with the location of microearthquakes. The hydrothermal system is therefore defined by a low resistivity zone and occurrence of shallow earthquakes less than 3km deep. Most of the earthquakes occur above the deep low resistivity which is interpreted as the heat source for the hydrothermal system.

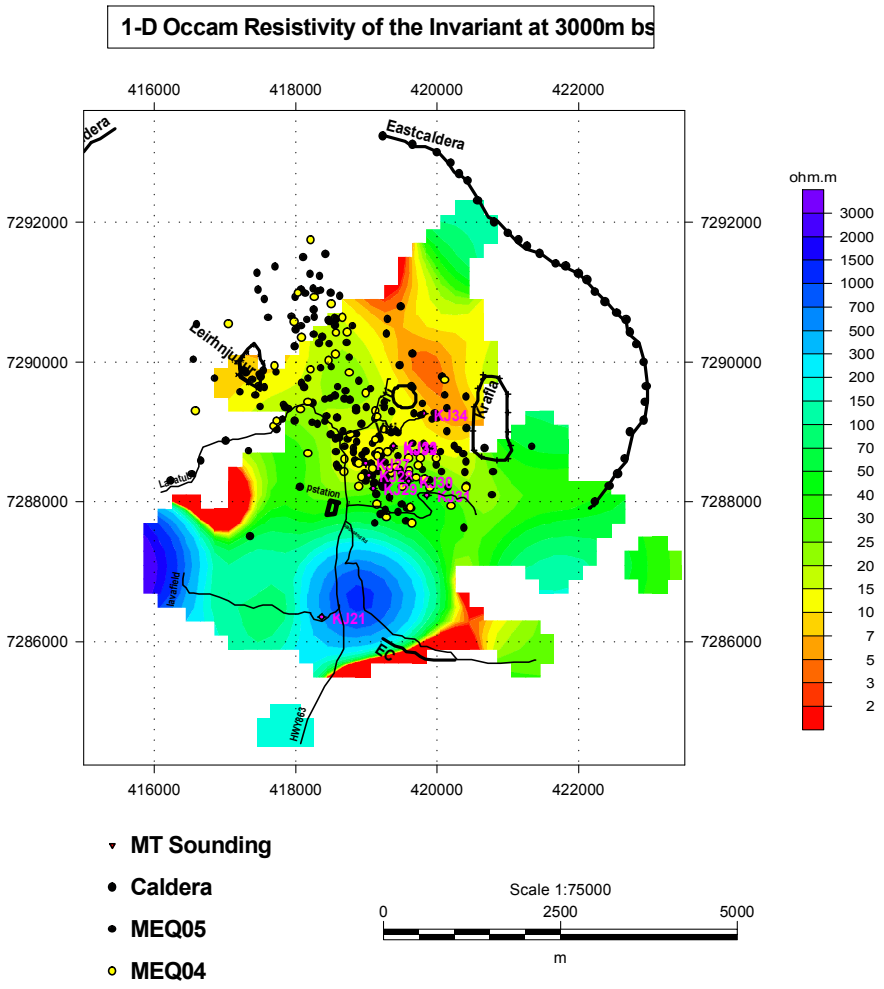

2.7 2-D MT Modeling

2.7.1 Synthetic Test for 2-D MT response across a fluid filled fault zone.

The model used in this study consists of a fault zone which is defined as a zone of high fracture porosity and consists of the main fracture zone with a core bounded by a damaged zone embedded in a host rock. The 2-D synthetic model is based on the conceptual model for the hydrothermal system (see Figure 6), the structural model of a fault zone (see Figure 7), existing models of S-wave and P-wave attenuation zones (see Figure 8) and the results of 1-D MT modeling. The choice of the orientation of the profile was based on the structural setting which shows that fissure swarms trend in this direction and also a postulated NW-SE structure which is the focus of this study. The synthetic models were developed to test whether anisotropy can be realistically modeled using different mesh sizes and resistivity contrasts to simulate anisotropy at the base of the clay cap. The anisotropy is presumed to be caused by variations in resistivity within isotropic bodies. In particular for the case a hydrothermal system where fluids flow along faults and fractures, we assume spatial variation in the physical properties of rocks on the scales of the fractures. However, the effect of alteration, temperature gradients and variations in hydrothermal fluids chemistry can cover a larger area than the fracture size.

For the synthetic model, the electromagnetic source is modeled as a plane wave and assuming that the physical properties of the earth are independent of one measuring direction. Recalling that the Maxwell's equations can be expressed in terms of the

decoupled TE and TM polarizations for currents flowing parallel and perpendicular to strike can be expressed as shown below:

$$\frac{\partial^2 E_x}{\partial y^2} + \frac{\partial^2 E_x}{\partial z^2} = -i\omega\mu\sigma E_x \qquad 2.43$$

$$\left.\frac{\partial E_x}{\partial z}\right|_{z=-h} = i\omega\mu \qquad 2.44$$

for the TE mode (Rodi and Mackie, 2001), and

$$\frac{\partial}{\partial y}\left(\rho\frac{\partial H_x}{\partial y}\right) + \frac{\partial}{\partial z}\left(\rho\frac{\partial H_x}{\partial z}\right) = -i\omega\mu H_x \qquad 2.45$$

$$H_x\big|_{z=0} = 1 \qquad 2.46$$

The complex apparent resistivities for the TE and TM mode are expressed as:

$$\rho_{TE} = \frac{i}{\omega\mu}\left(\frac{E_x}{H_y}\right)^2 \qquad \text{and} \qquad H_y = \frac{1}{i\omega\mu}\frac{\partial E_x}{\partial z} \qquad 2.47$$

$$\rho_{TM} = \frac{i}{\omega\mu}\left(\frac{E_y}{H_x}\right)^2 \qquad \text{and} \qquad E_y = \rho\frac{\partial H_x}{\partial z} \qquad 2.48$$

The algorithms used by Rodi and Mackie 2001, solves equations 2.43 to 2.48 by segmenting the half space into rectangular blocks of different dimensions each assigned a constant resistivity (for details refer to Rodi and Mackie 2001).

The forward model is computed using finite difference equations generated by network analogs to Maxwell's equations. The 2-D mesh is user defined and it incorporates topography. The forward response is saved as station data.

The synthetic model (Figure 23) based on the geological and 1-D model has a surface high resistivity layer corresponding to recent lava flows and hyaloclastites. The surface layer resistivity was based on the TEM data interpretation. The second layer has low resistivity and corresponds to the clay cap. This layer has variable resistivity at the base which can contribute to anisotropy. Third layer below the clay cap has higher resistivity than the low resistivity clay cap. The fracture zone is characterized by a low resistivity zone that increases in resistivity out ward from the core.

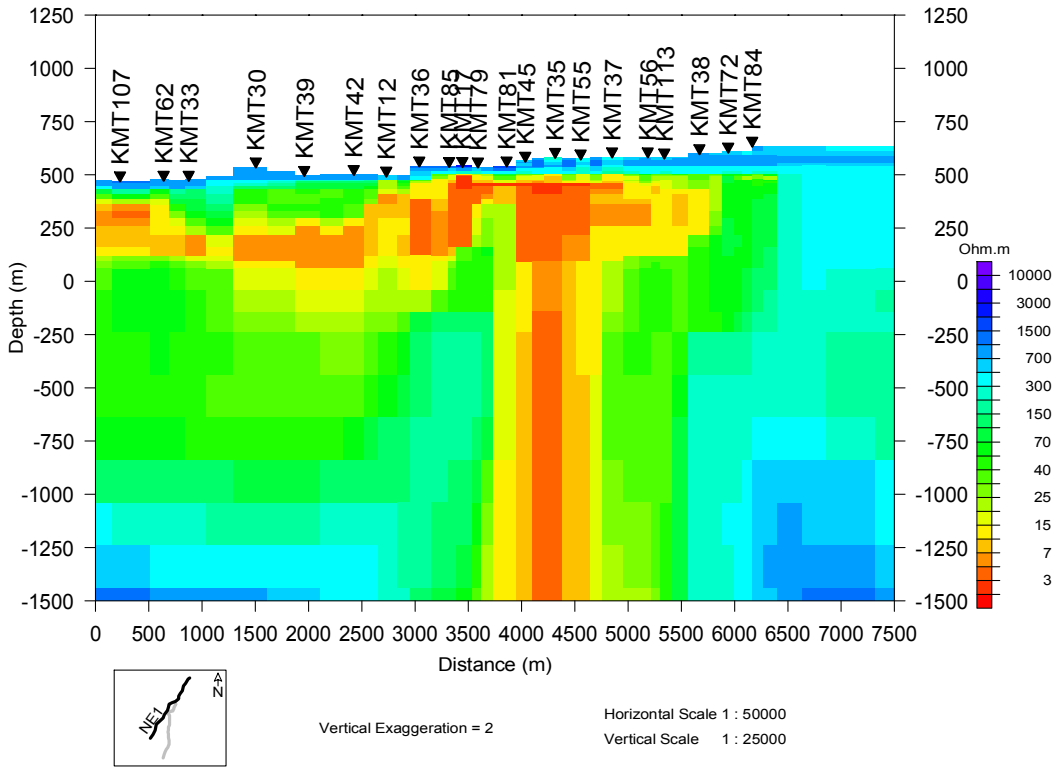

Figure 23 The synthetic 2-D resistivity model for the ear surface layers close to a fracture zone modeled as an area of lower resistivity than the surrounding host rock which has higher resistivity. The clay cap is defined by the horizontal layer of low resistivity which can be viewed as a zone of columns of variable low resistivity extending from the base of the clay cap.

The largest resistivity contrast is at the boundary of the fault zone and the host rock, the base of the clay cap and the contact zone of the heat source. Several forward models were tried out with variations in thin layers at the base of the clay cap and only the best model with the lowest RMS and which reproduced the splitting in the observed data is shown.

The model is sensitive to the depth to the base of the clay cap and the size of the fracture zone. Since most of the sites have a separation of about 300m the grids are interpolated between the stations and the resolution is about 150m. The vertical grid is near the surface is about 30m increasing logarithmically with depth.

The postulated heat source is modeled as a low resistivity zone with resistivity increasing outwards from the center. The low resistivity is bound by high resistivity on both sides. The response for the forward model shows that the low resistivity zone affects the resistivity in one of principal resistivity directions in such away that the resistivity continuously reduces with depth. The response of the data shown below produces shifts in the data. The amount of shift depends on the resistivity contrasts at depth and the proximity to the postulated fracture zone. The resistivity at sites some distance away on either side of the fracture zone show very little splitting in the resistivity in the principal directions.

From the forward model, we concluded that the split in the MT resistivity data is mainly caused by the resistivity contrasts at depth rather than lateral surface contrasts.

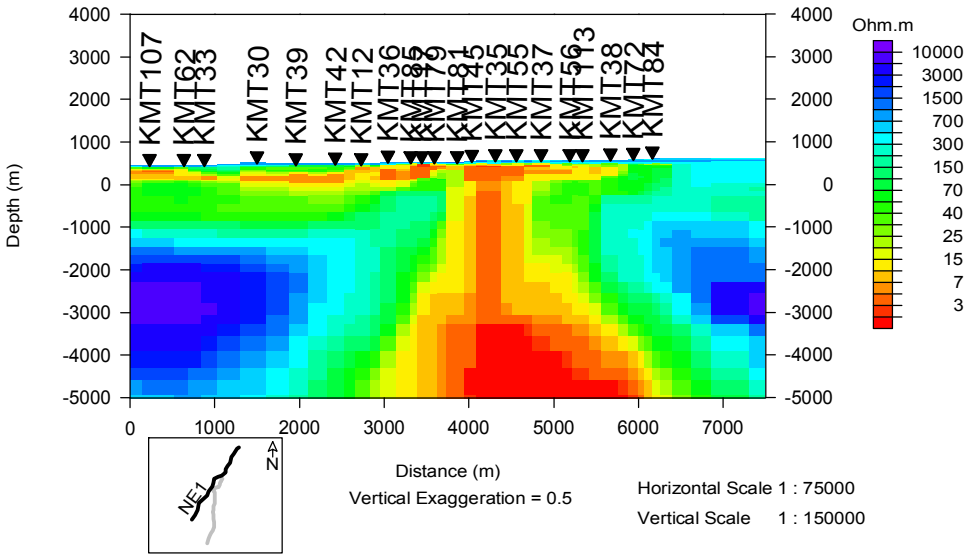

Figure 24 The synthetic 2-D model of the fracture zone including the postulated low resistivity heat source based on TEM and 1-D MT data of a NE-SW profile. The deep low resistivity zone is about 3km wide below a depth of 3km. The vertical column of low resistivity corresponds to the postulated core. Resistivity increases outwards from the core towards the host rock.

2.7.2 2-D MT inversion across a fluid filled fault zone.

The 2D smooth model inversion routine in WinGlink (Mackie, 1996) was used. The inversion routine finds regularized (smooth) solutions assuming a 2-D resistivity distribution using the Nonlinear Conjugate Gradients (NLCG) method to match the MT data (Rodi and Mackie, 2001). The NLCG method is used to minimize an objective function that is the summation of the normalized data misfits and the smoothness of the model. The tradeoff between data misfits and model smoothness is controlled by a regularized user defined parameter (tau) which penalizes data residuals and spatial second order resistivity (Rodi and Mackie, 2001).

The TE and TM resistivity modes can be expressed as complex linear systems of equations of the form given by Rodi and Mackie as shown below;

$$Kv = s \qquad 2.49$$

where the vector v is electromagnetic field (E_x or H_X) on the grid, the symmetric matrix K and vector s are functions of frequency and the dimensions and resistivities of the model blocks. From equations 2.47 and 2.49, the complex apparent resistivity for a given site is then formulated as;

$$\rho_a = \frac{i}{\mu\omega}\left(\frac{a^T v}{b^T v}\right)^2 \qquad 2.50$$

In this case a and b are given vectors and the superscript T indicates the transpose. The inverse problem relates the observed data vector (d) to a forward function (F) of the model vector (m) and the error vector (e) as shown below (Rodi and Mackie, 2001).

$$d = F(m) + e \qquad 2.51$$

For either TE or TM polarization, $d = \left[d^1 .....d^N\right]^T$ or d^i where $i = [1.....N]$ the number of log amplitude or phase apparent resistivity for any given frequency, $m = \left[m^1 ....m^M\right]^T$ is the resistivity and M is the model blocks. Details of the inversion and minimization can be found in Rodi and Mackie 2001.

The desire of the inversion is to achieve the lowest RMS error and the smoothest model. The 2-D mesh of is made of resistivity blocks each with a constant resistivity. The blocks extend laterally and with depth. The regularization is performed on the actual

mesh the Laplacian $\left(\nabla^2 m\right)^2$ of the model. The inversion was carried out for both TE and TM modes for 6 decades of data on the log scale covering frequency range of 320-0.001Hz for the MT data and 10,400-0.1Hz for AMT data.

The choice of the profiles was made after initial analysis of the data which indicated significant structures trending in the NE and NW directions. It was therefore anticipated that the principal resistivity directions would be in these directions.

2.8 3-D MT modeling

2.8.1 Data Parameters and Memory requirement.

The 3-D forward model and inversion was based on the WSINV3DMT code (Siripunvaraporn et al., 2005). The development of the code was based on Occam's inversion (Constable, 1987., deGroot-Hedlin and Constable, 1990). The WSINV3DMT code is based on data-space inversion approach in which the matrix dimensions depend on the data sets and not on the number of model parameters (Siripunvaraporn et al., 2005, Siripunvaraporn and Egbert , 2000). The code inverts for 3-D impedance data with 3-D inversion. One limitation of the code is the large memory required to store the sensitivity matrix.

The total size of the dataset is defined by the data parameter N defined below;

$N = N_p N_S N_r$ =18*50*8=7200

Where N_p , in the number of periods which are 18 for this study, N_S is the number of stations (50 for this study) and N_r is the number of responses (maximum 8).

The model parameter size M is defined by the product of number of discretization blocks in the north-south direction (M_X), the number in the east-west direction M_y, and the number in the vertical direction M_y as shown below;

$$M = M_X M_y M_Z = 12000$$

The memory requirement is 1.2*(8*7200*7200+8*12000*12000) = 1880064000=1.88 Gbyte.

2.8.2 Data Preparation

50 MT stations were chosen from the data to cover a nearly uniform grid covering an area of 5 km^2 around the Krafla hydrothermal system. The data at each site was reduced to 3 frequencies per decade for six decades. The data was edited manually to preserve the general resistivity trend at each site. After the editing, the data was transformed from the EDI format to the format required for the WSINV3DMT code using a Matlab code. The data input file contains the number of stations, number of periods, and the number of responses (the real and imaginary parts of the off-diagonal and diagonal impedance tensors). The data locations are listed in meters with respect to the centre station. The initial model specifies the number of resistivity grids, the block sizes in the north-south, east-west and vertical directions. The resistivity distribution in each block is specified by pre-assigned resistivity indexes.

2.9 Comparison of the results of 2-D and 3-D modeling

3. Microearthquake imaging of fault zones at the Krafla hydrothermal system

3.1 MEQ Data Acquisition

The data from two surveys carried out in July-August 2004 and August 2005 in the Krafla geothermal area has been used to locate microearthquakes and evaluate shear wave splitting anisotropy. In the summer of 2004, twenty microearthquake monitoring stations sampled at 500 samples per second (2ms). Additional data used in this research was collected by the University of North Carolina at Chapel Hill in July-August 2004. Additional MEQ data was collected by duke University in the northern part of Krafla using 15 three component geophones with a natural frequency of 1Hz and a sampling rate of 250 samples per second (4ms). MT data was collected at the same sites. The mechanisms for generating earthquakes in hydrothermal systems have been outlined in the introduction.

3.2 Theoretical Background

The basic theory of seismic wave propagation is based on the equations of motion. The wave can then be defined is a balance between an inertia term and a restoring force. The resulting wave propagates through the medium without movement of material. The wave motion is usually described using the theory of linear elasticity. The equation of motion for a bulk medium can be expressed as;

$$\rho \frac{\partial^2 u_i}{\partial t^2} = \sigma_{ji,j} + f_i \text{ for } (i, j = 1,2,3) \qquad 3.1$$

where ρ is the density, t is time, u_i is the i^{th} displacement component $\sigma_{ji,j}$ is the stress tensor Einstein's summation of the spatial derivative of the j^{th} component of the j^{th} element of the stress tensor and f_i is the body force component (which can be neglected for in most wave propagation problems). Hooke's law relates the stress tensor σ_{ij} to the constitutive elastic constants of the medium C_{ijkl} and the strain tensor e_{kl} as shown below.

$$\sigma_{ij} = C_{ijkl} e_{kl} \text{ for } (i, j, k, l=1, 2,3) \quad 3.2$$

and the strain tensor is defined as

$$e_{kl} = \frac{1}{2}\left(u_{i,j} + u_{j,i}\right) \quad 3.3$$

If the body force is ignored, the equation of motion can be expressed as;

$$\rho \frac{\partial^2 u_i}{\partial t^2} = C_{ijkl} u_{k,lj} \quad 3.4$$

This equation can be solved by assuming an exponential solution for the displacement to satisfy the second order differential equation.

$$u_i = A_i e^{-i(\omega t - k.x)} \quad 3.5$$

In this case, k is the wave number; ω is angular frequency and A_i is the amplitude. By differentiating equation 3.5 twice and substituting in equation 3.4, the equation can be expressed as;

$$\left(C_{ijkl} k_l k_j - \rho\omega^2 \partial_{ik}\right) A_k = 0 \quad 3.6$$

The focus of this research is to evaluate the properties of micro earthquake propagation with a view understanding the complex fluid circulation in hydrothermal

systems. The emphasis is then to evaluate the velocity of seismic waves in hydrothermal systems and establish quantifiable means of evaluating the subsurface elastic parameters which are controlled by rock type, complicated alignment of fractures and cracks, porosity and the amount and type of fluids filling the pores, pore pressure and connection of pores.

The pores, cracks, fractures, fissures, joints, faults, and the internal rock structures are important in controlling the storage and transmission of fluids in rocks. Several theoretical formulations to study seismic propagation in porous or fractured medium have been formulated over the years (e.g Biot 1956; Hudson, 1980 and O'Connell and Budiansky, 1974) but their field applications have been limited. This research focuses on evaluating the effect of internal rock and fractures. The physical properties of porous medium are usually determined by evaluating the interaction between the solid grains and pore fluid, parameters that characterize the structures, and the coupling mechanisms between the solid matrix, fluid, fractures and pressure. The velocity change due to pressure changes is caused mainly by mechanical coupling between solid grains, pore fluid and the interconnection of the pores (Sun et al., 1994; Sun and Goldberg, 1997a). The pressure affects the rigidity of the medium.

For a two phase isotropic fractured porous media, the porosity σ_f distribution can be expressed as

3.3 Location of microearthquakes

Locating earthquakes requires the identification of seismic phases and the knowledge of the velocity model. Solving the forward problem is easy if the velocity structure and the travel time of the P and S waves are known. However, the velocity structure and the origin time at the hypocenter are not usually known.

For a simple homogenous case, the travel time for the P and S waves can be calculated from the distance from the source to the receiver. If D is the distance from the hypocenter to seismometer, and Tp and Ts are the travel times for the P and S waves respectively, then for the forward problem:

$$T_p = D/V_p \text{ and } T_s = D/V_s \qquad 3.7$$

Where $T_p = t_p - t_o$, $T_s = t_s - t_o$ and t_p is the P wave arrival time, t_s is the S wave arrival time and t_o is the origin time.

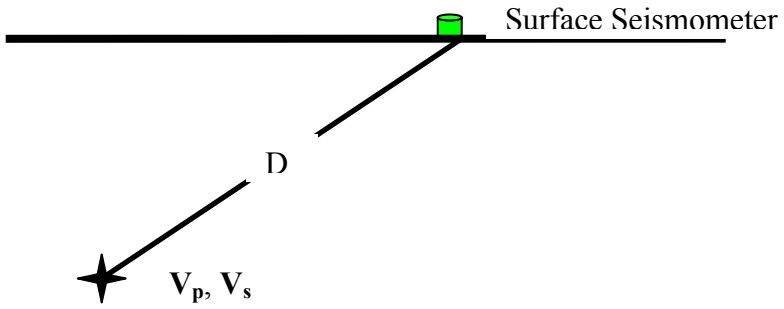

Figure 25

Since $T_p V_p = D$, then the difference in the travel time of the P and S is the same as the difference in the arrival time.

$$t_s - t_p = D\left(1/V_s - 1/V_p\right) = D/V_p\,(V_p/V_s - 1) = (V_p/V_s - 1)t_p \qquad 3.8$$

For any station, the arrival time is formulated in terms of the unknown parameters for the earthquake and the known parameters for the station location. For any given station, the forward problem for the arrival time $t^{(i)}$ is related to model parameters, the unknown earthquake location, the origin time, velocity and the known station location parameters by the equation shown below;

$$t^{(i)} = F^{(i)}\left[x_{(j)}, t_o, \vec{V}, \vec{y}_i\right] \qquad 3.7$$

where i=1,…..N; j=1,2,3; and N≥3 for accurate location of earthquakes; $t_{o;}$ is the origin time, $\vec{V}$ is the average velocity, $\vec{y}_i$ are the known station parameters. The expression $t^{(i)}$ forms the forward problem with the unknown parameters are $x_{(j)}, t_o$, the origin time and location of the earthquake. The arrival times for recording stations and the unknown parameters can be expressed as vectors as shown below:

$$\bar{d} = \left[t^1 \ldots\ldots t^N\right]^T \qquad 3.8$$

$$\bar{m} = \left[t_0, x_1, x_2, x_3\right]^T \qquad 3.9$$

The forward problem is then reformulated as;

$$\bar{d} = \bar{F}\left[\bar{m}\right] \qquad 3.10$$

For a homogenous earth, the forward problem can be expressed as a no-linear form;

$$t^i = t^0 + \frac{1}{V}\left[\left(y_1^i - x_1\right)^2 + \left(y_2^i - x_2\right)^2 + \left(y_3^i - x_3\right)\right]^{1/2} \qquad 3.5$$

This non-linear problem can be linearized by expanding equation 3.4 and expanding it using the Taylor series about a starting model $(\overline{m}_0)$.

$$\overline{d} = \overline{F}(\overline{m}_0) + \nabla\overline{F}\Big|_{m=m_0}\left(\overline{m} - \overline{m}_0\right) + \ldots\ldots \text{ + smaller terms} \qquad 3.6$$

$$\text{and } \nabla\overline{F} = \begin{matrix} \frac{\partial t^1}{\partial t_0} & \frac{\partial t^1}{\partial x_1} & \frac{\partial t^1}{\partial x_2} & \frac{\partial t^1}{\partial x_3} \\ . & . & . & . \\ . & . & . & . \\ \frac{\partial t^N}{\partial t_0} & \frac{\partial t^N}{\partial x_1} & \frac{\partial t^N}{\partial x_2} & \frac{\partial t^N}{\partial x_3} \end{matrix}$$

The terms in the first column correspond to the variation in the original time with time while terms in the other three columns express the time differences in the directions of the coordinate system.

The smaller terms can be ignored and the linear system solved in the least squares sense. The location of events is carried out first by picking only one P and S wave arrivals using the Hypoinverse-2000 code (Klein 2000) with a parameter input interface in Matlab.

The initial velocity model was obtained from the results of seismic studies at Krafla by Brandsdottir et al., 1995. After locating many events, the locations were used to improve on the velocity model. A list of the location of microearthquake stations were

determined from the internal GPS measurements and cross checked with locations from the hand held GPS. The microearthquakes are located at a reference datum which is the average of the stations which is 550m. Station corrections are incorporated to account for the elevation differences with respect to average elevation. The station corrections are computed by locating many earthquakes with zero corrections and then assign the average time errors as station correction.

In the 2005 data set, 198 MEQ events were used for the location of earthquakes with a minimum of 4 stations required to pick an event. In the 2004, data set, 50 MEQ events were used to locate the earthquakes. Only the high quality events with clear P and S arrivals were used. The earthquakes are found mainly in the hydrothermal systems with a NW-SE trend (Figure). The shallowest earthquakes are found to the northern part of the Leirbotnar and Sudirhlidar hydrothermal system and to the west of Krafla Mountain especially around well KJ34. Most of the earthquakes occur at elevations of less than 2000 mbsl. A second area of shallow microearthquakes is found in the area designated as Krafla NW to the north of Leirhnjukur. This area is close to the source of the 1979-1984 volcanic eruptions of basaltic lava flow. The area designated as Krafla SW has very few deep earthquakes.

The shallow earthquakes around well KJ34 seem to be associated with an area of high output (Figure) and fluid flow. From this observation, it is possible that the shallow earthquakes may be correlated to areas of enhanced fluid flow due to high fracture porosity.

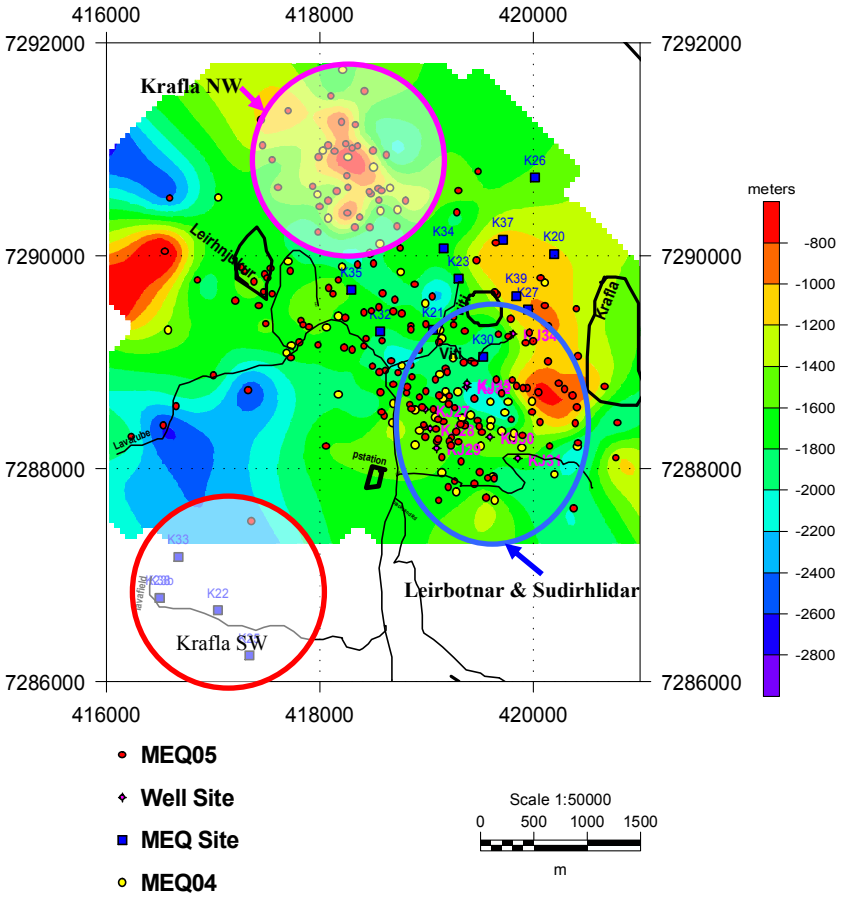
416000
418000
420000
7292000
7290000
7288000
7286000
Krafla NW
Leirhlidar
Krafla
Leirbotnar & Sudirhlidar
Krafla SW
K26
K37
K34
K20
K23
K39
K27
K21
K30
K33
K22
meters
-800
-1000
-1200
-1400
-1600
-1800
-2000
-2200
-2400
-2600
-2800
MEQ05
Well Site
MEQ Site
MEQ04
Scale 1:50000
0 500 1000 1500
m

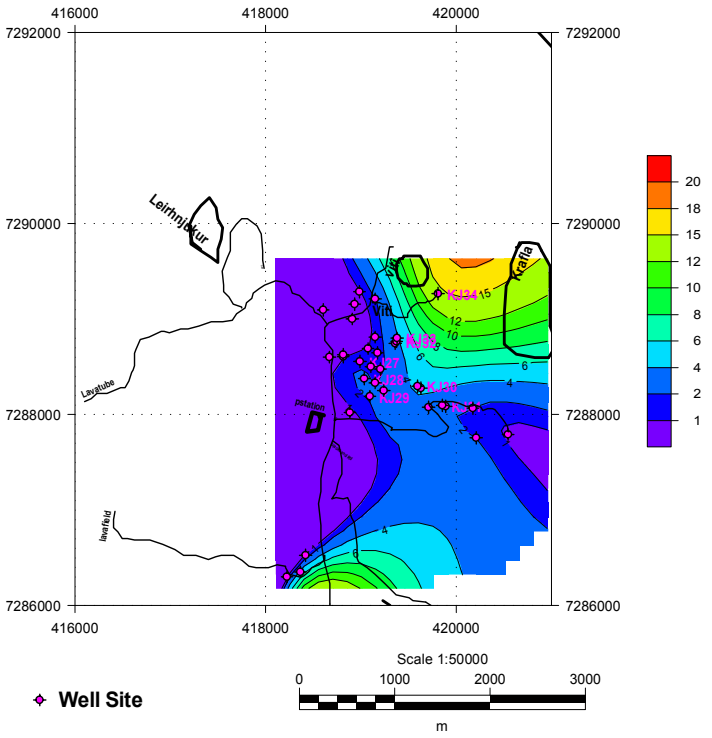

Include interpretation and Direction where earthquakes are located

Investigate Use of resistivity to generate model then relocate.

In this research, the resistivity structure is used to constrain the velocity model. Initial models P-wave will correlate with 1-D resistivity sections. Seismic anisotropy is routinely used to deduce information about the fracture orientation and the spatial distribution of fracture intensity. This method applies the equivalent medium theories which describe response of rocks containing cracks and fractures. This approach models frequency-dependent anisotropy and its sensitivity to the length scale of the fractures (Maultzsch et al., 2003)

3.1 Shear Wave Splitting and polarization

Shear wave splitting which is sometimes referred to seismic birefringence (or double refraction), has been thought of as the most diagnostic and measurable property of seismic anisotropy (Crampin 1985). The anisotropy is usually interpreted as a characteristic of fluid-saturated, stress-aligned cracks or grain-boundary films of liquid melt (Crampin, 1994, 1996, 2005). It has also been observed in several studies that shear-wave splitting shows temporal and spatial variation in response to small changes in stress (Crampin and Peacock, 2005). Crampin and Peacock (2005) have noted that there is a problem in analyzing and interpreting the observed anisotropy from measurements recorded by instruments on the surface because the depth of the anisotropy is not usually known. In this study we use the similarity in the MT polarization and shear wave splitting to determine the depth of the anisotropy (This is discussed in section 4.2). The most important parameters in evaluating shear wave splitting are the polarization angle (PA) of the fast shear wave arrival and the time difference (δt) between the fast and slow waves. Both the PA and δt are related to the orientations of the cracks and crack density.

Some of the earthquakes recorded both during the 2004 and 2005 field deployment show shear-wave splitting. An example of shear wave splitting is given for

station K21 below (Figure). The coda for the earthquake is less than 2 seconds and the difference between P and S wave arrival is less than 0.5 seconds.

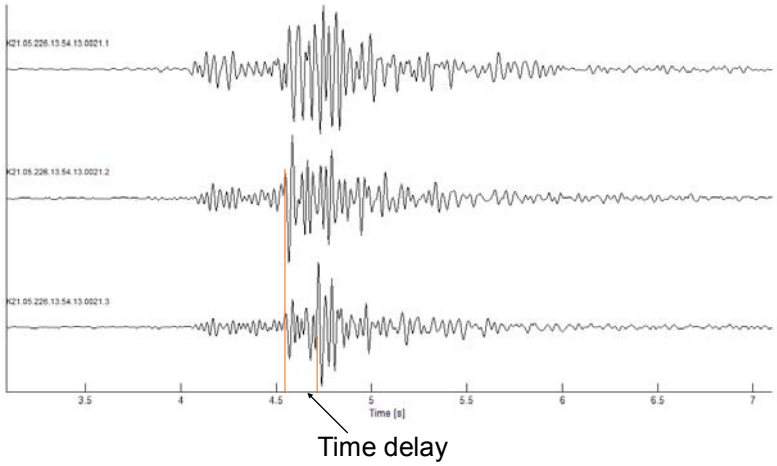

In shear wave splitting models, the only data available is arrival times and location of stations. Fractures are important in determining the amount of fluid in hydrothermal systems. The fractures are aligned parallel to the direction of maximum compression stress. The time delays between the fast and slow S-waves give information about the average crack density along the ray paths. The main interest is to determine the shear wave polarization and compare it to the polarization in the Magnetotelluric data. Is the shear wave related to fractures or is it related to the effects of temperature which include alteration. The major problem is determining the sizes, depth and volume of fractures. In hydrothermal systems, the interest is in large scale fractures. In developing the fracture model emphasis is on the size, orientation, depths and intersection of fractures. Some studies of shear wave splitting have been carried out in some geothermal fields like the Geysers (Elkibbi, 2005). Shear wave splitting data in the Geysers is

interpreted as due to stress-aligned fractures in otherwise isotropic medium (Elkibbi and Rial 200). The time delays were found to be between 8 and 40 milliseconds per kilometer.

The crack density varies in a given volume of rock is proportional to the cube of the crack radius (Hudson, 1980. Crampin, 1994) as shown below:

$$\delta = \frac{Na^3}{V}$$

In this case N is the number of cracks with radius a (length $2a$) for a given volume of rock V. If we assign the polarization parallel to the fractures as $P1$ and the polarization perpendicular to the fractures as $P2$, the difference in the velocity can be expressed as an approximation for number of fractures per unit volume.

$$\alpha = (V_{P1} - V_{P2}) \Big/ V_{P1}$$

When shear wave splitting is observed after rotation to the direction of fast and slow polarization, we can determine the corresponding time delay. Both the polarization direction (γ) and time delays (δt) can be used to estimate crack density and anisotropy. The shear wave polarization for each site is determined and compared to that of MT data.

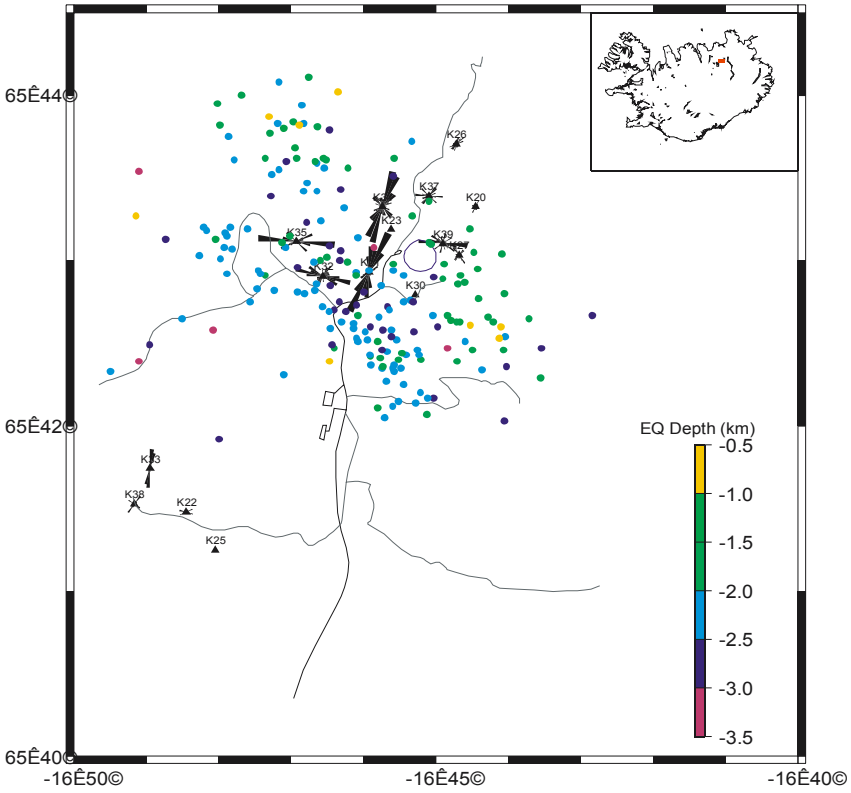

3.2 Analysis of Vp/Vs ratios

The plots of the difference between the S-arrival and the P-arrival time $(t_s - t_p)$ against the P-arrival time t_p for some selected earthquakes shows that there is a variation in the V_p/V_s ratios given by the slope of the gradient of the graph. The intercept of the graph is an approximation of the origin time for the earthquake.

In general for i stations the travel time is expressed in terms of the distance, arrival time, origin time, and the P wave velocity as shown below:

$$D^i = \left(t_p^i - t_0\right)V_p$$

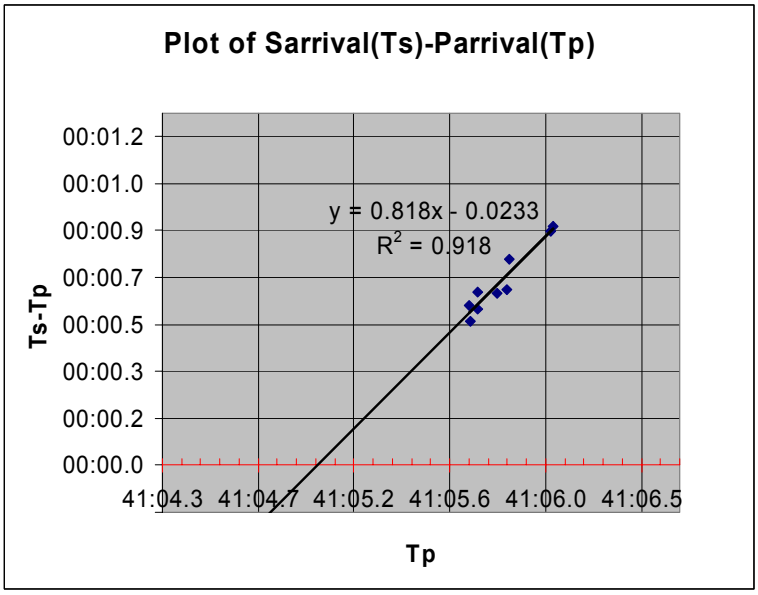

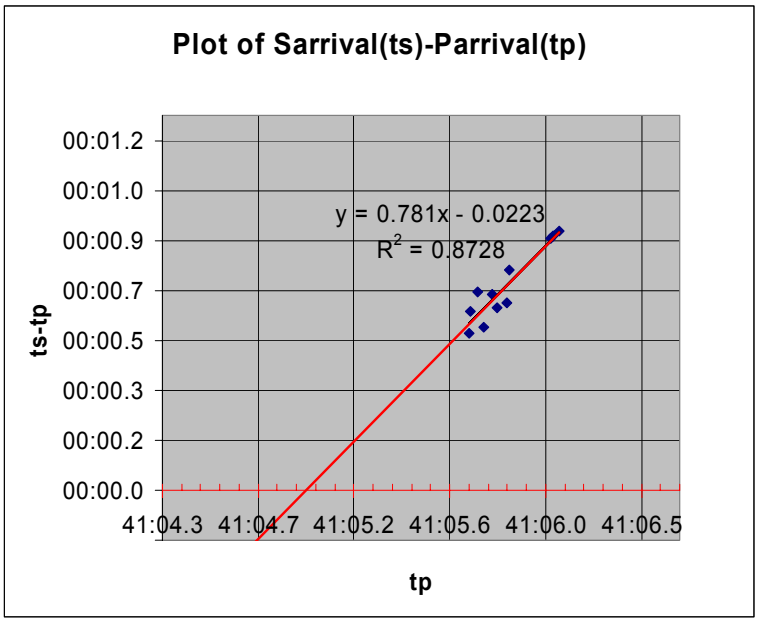

The figures above show that there is a variation in the Vp/Vs ratios which may be attributed to variations in fracture porosity. In regions with higher fracture porosity

4. Joint microearthquake and resistivity imaging of buried fault zones in hydrothermal systems

The background to joint interpretation of geophysical data acquired by different methods is based on the assumption that the observed anomalies are caused by the same physical parameters (Kozlovskaya E. 2001). The main assumption in this study is that both resistivity and velocity of rocks in hydrothermal systems are affected by the same physical properties, fractures and faults which have impedance and resistivity contrasts at structural and geological boundaries. Variation in measured resistivity values across a site are interpreted as variance in the relative resistivity of materials composing the matrix in the vicinity of each reading. Resistivity surveys respond to a combination of fluid content, temperature, degree of alteration (clay content), porosity, fracture density and rock type. In some instances we propose to use the variations of the resistivity in the electric major strike and that perpendicular as an estimate of fracture porosity as shown below. The higher resistivity (in the direction perpendicular to electric strike) was used as an estimated of the bulk resistivity of unfractured rock. The resistivity and velocity are affected by porosity, fluid content and type, degree of fracturing rock grain size and the clay content.

In this equation, we assume that porosity affects the propagation of seismic waves through the medium at collocated data acquisition sites. In clay mineral-rich rock, resistivity measurements can have frequency dependence because clays tend to preferentially absorb cations. The available geological well data is used to evaluate the

degree of hydrothermal alteration to use in modeling of the observed resistivity. This information will also be useful in comparing resistivity isotherms and the degree of hydrothermal mineral alteration. Fractured rocks will tend to have high porosity and therefore generally lower resistivity. Resistivity of near surface material is heavily affected by groundwater and degree of hydrothermal alteration. We will model the MT frequency dependent anisotropy to show the changes in anisotropy with depths using a similar scheme developed by O'Brien and Morrison (1997) who indicated that the larger scatter in the TE and TM mode resistivity can be accounted for by changes in Azimuthal polarization. Heise and Pous (2001) point out that it is generally hard to determine whether the splitting in the MT resistivity curves at a site are caused by anisotropy or 2-D or 3-D effects. However, their tests also indicate that when data shows high splitting of the resistivity, it is possible to model the data in terms of anisotropy. This scheme is used for the MT data in Krafla where the downhole geology is reasonably uniform and the near surface is quite homogenous. The anisotropy modeling will be carried out after using TEM data to correct the static shifts in MT data by transforming the TEM to equivalent MT frequencies. Where porosity measurements exist for instance in the Olkaria and Krafla geothermal fields, the computed values will be adjusted and used to constrain the resistivity model.

4.1 Relationship between resistivity, P-wave velocity and porosity

4.1.1 Relationship between resistivity, temperature of pore fluid and porosity

The key to mapping rock formations is to understand the factors that affect seismic velocities. The major factors are density of the rocks, porosity, degree of fracturing and temperature. All these factors also affect the bulk resistivity of rocks. The bulk modulus of the rocks relates strain due to an applied stress.

When the medium is elastic and isotropic, the velocity can be expressed as a function of bulk modulus (κ) and shear modulus (μ). In an isotropic medium, the elasticity coefficients can be expressed by Lame's coefficients λ and μ. The bulk modulus (incompressibility) relates the change in pressure to the change in volume. Other important coefficients are the Young's modulus (E), which relates the longitudinal stress and strain in the same direction and Poisson's ratio (σ). The Poisson's ratio relates strain in mutually orthogonal directions due to stress in one of the directions.

The shear modulus (rigidity) relates changes in form without change in volume. When an earthquake is generated, body and surface waves travel through the rocks. We are more interested in the body waves which generate P-waves and S-waves which are related to the elastic coefficients as shown below;

$$V_p = \sqrt{\lambda + 2\mu / \rho} \text{ or } V_p = \sqrt{(K + \frac{4\mu}{3}) / \rho} \text{ while } V_s = \sqrt{\mu / \lambda} \qquad 4.1$$

In this equation, K is the bulk modulus and μ is the shear modulus. The bulk density ρ_b depends on porosity (Φ), density of the matrix ρ_m and density of the fluid ρ_f as shown below

$$\rho_b = \Phi\rho_f + (1-\Phi)\rho_m \qquad 4.2$$

In hydrothermal systems, the density of the fluid is a function of pressure, temperature and salinity. The P wave velocity can be approximated by the equation below.

$$\frac{1}{V_p} = \frac{\Phi_f}{V_f} + \frac{(1-\Phi_f)}{V_m} \qquad 4.3$$

From the equation above, porosity can be expressed as;

$$\Phi_f = \frac{(V_m - V_p)V_f}{(V_m - V_f)V_p} \qquad 4.4$$

In the vicinity of the fractured zones, we can consider V_m as the velocity of the unfractured rock and V_p as the measured velocity, V_f is the velocity of the fluid.

This equation can be extended for the 3d case by considering the shear wave velocity. From this equation, we can deduce that as porosity increases, the velocity of the matrix reduces. We therefore expect the P wave velocity of the rock matrix to reduce in fault zone within a hydrothermal system. If we consider shear wave time arrivals, we can calculate the ratio of arrival times. If location of the earthquake is known then we can consider the direction of fast and slow shear waves. Ratio of T_f and T_s can be related to the anisotropy. In cracked reservoirs, this anisotropy is usually caused by aligned systems

of open, fluid-filled micro-fractures. The deployment of seismic arrays were designed especially designed to gather SWS data with uniform Azimuthal coverage, ideal to perform high-resolution tomographic inversion for 3D fracture density. In addition, evidence of time variations in shear wave splitting parameters, which are diagnostic of fluid migration in the reservoir, will be carefully monitored.

From the analysis of field measurements and core samples Flóvenz' et al. (1985) established a semi-empirical relation based on the double porosity model (Stefansson et al., 982). An important finding in this study was that for rocks saturated with fluids with resistivity higher than 2 Ωm (at room temperature), the bulk resistivity is independent of fluid but dependent on porosity and temperature. This finding was used in this study to evaluate the dependence of resistivity and P-wave velocity on fracture porosity with emphasis on understanding the structural and physical controls for hydrothermal fluid circulation.

The general equation that describes the measured resistivity of rocks is shown below:

$$1/\rho = ((1-\Phi)(1-P_c))/\rho_b + P_c(1-\Phi)/\rho_c + \Phi S_w/\rho_w + \Phi(1-S_w)/\rho_a \qquad 4.5$$

Where ρ, ρ_b, ρ_w and ρ_a are the measured resistivity (including fractures), resistivity of rock matrix, resistivity of clay, resistivity of the hydrothermal fluids (water) and resistivity of air or steam respectively. S_w is water saturation; Φ is porosity and p_c is percentage of clay.

If we consider the rocks a hydrothermal reservoir, below the clay cap, and assume maximum fluid saturation and a low percentage of low temperature clays, then the measured resistivity is controlled by fracture porosity, the bulk resistivity and the resistivity of the hydrothermal fluids as shown below:

$$1/\rho = (1-\Phi)/\rho_b + \Phi/\rho_w \qquad 4.6$$

The equation above can be rearranged as

$$\Phi_f = ((\rho_w(\rho_b - \rho)) / \rho\,(\rho_b - \rho_w) \qquad 4.7$$

Based on equation above, the measured resistivity can be used to estimate the fracture porosity of the formation.

The semi-empirical relationship established by Flóvenz' et al. (1985) for the measured resistivity is shown below:

$$\frac{1}{\rho}=\frac{0.22}{\rho_w}\left[1-(1-\Phi_f)^{2/3}+\frac{(1-\Phi_f)^{2/3}}{1+(1-\Phi_f)^{1/3}+(1-\Phi_f)^{1/3}4.9x10^{-3}}\right]+\frac{\Phi_f^{1.06}}{b} \qquad 4.8$$

$$\rho_w=\rho_{wo}/\left[1+0.023(T-23)\right] \qquad 4.9$$

$$b=8.7/\left[1+0.023(T-23)\right]\left[1+0.018(T-23)\right] \qquad 4.10$$

The analysis of the dependence of pore water resistivity on temperature from equation 4.9 indicates that for a reservoir saturated with meteoric water with a low percentage of dissolved salts, the pore water resistivity is always more than 10,000 Ωm for a temperature range of 100-400˚C. The resistivity of water at room temperature is about 2.5 x105 Ωm at 23˚C. The relation ship follows a power law (Figure 4.1).

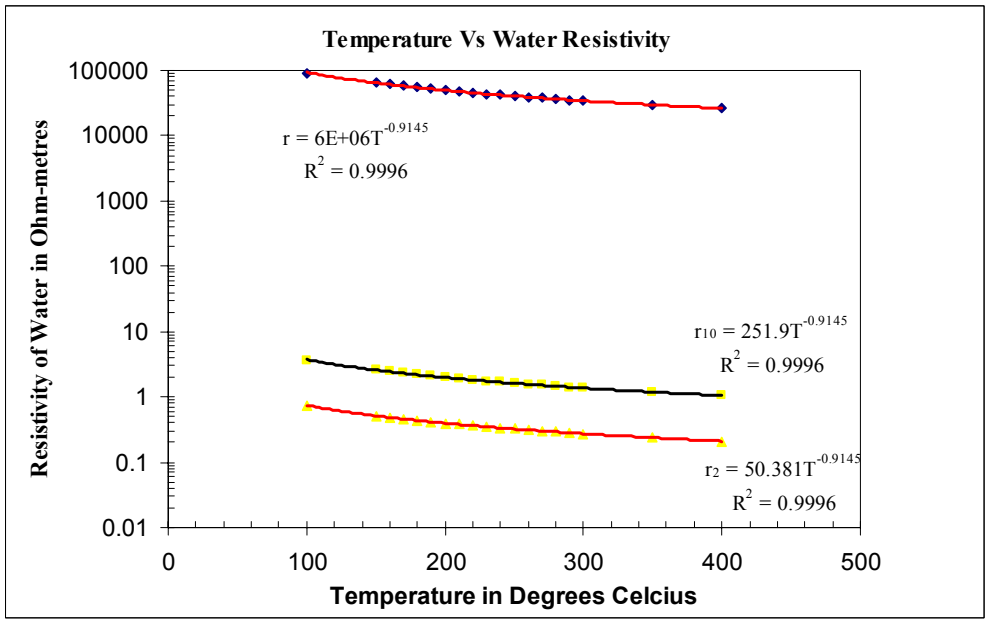

When the empirical results for the resistivity of water for 10 Ωm (r_{10}) and 2 Ωm (r_2) are plotted on a linear scale for the temperature range of 0-400°C, it is clear that for very low resistivity of water, there is very little variation in resistivity with increase in temperature. The variation is significant at high resistivity of water and at low temperatures (Figure).

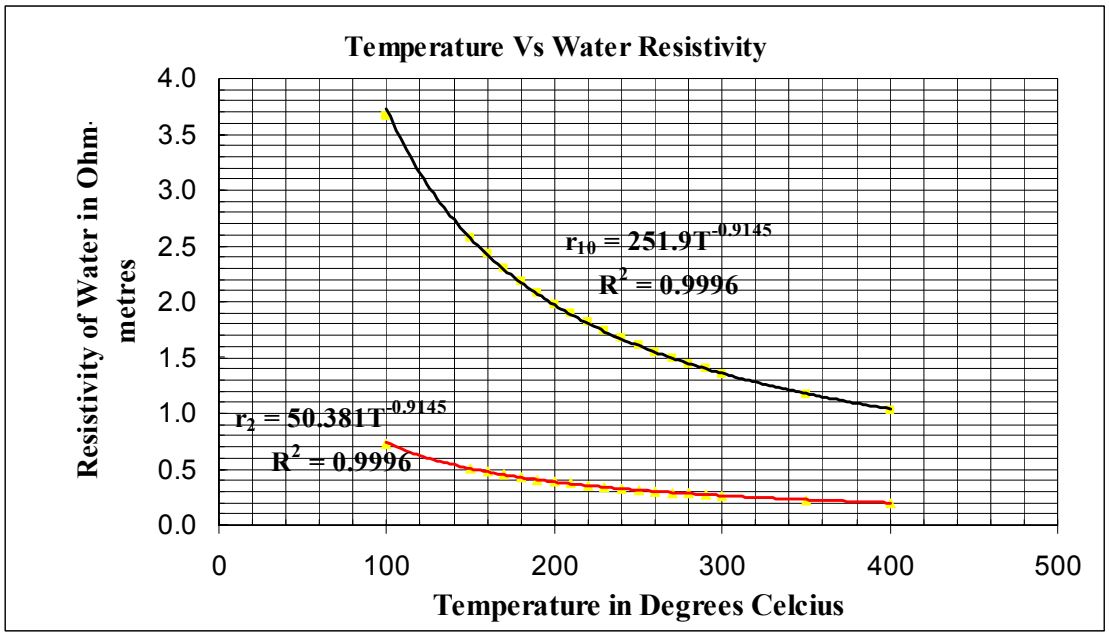

From this graph, the pore fluid resistivity for hydrothermal fluids of resistivity 2Ωm is given as shown below:

$$\rho_w = 50.381T^{-9145} \qquad 4.11$$

For a reservoir temperature of 240°C below the clay cap, the resistivity of the hydrothermal fluids would be 0.3354.

The value of **b** in equation 4.10 for a temperature range of 50-400˚C was empirically calculated and plotted against temperature (Figure 4.2). The plot shows that the value of **b** is higher at low temperatures below 100˚C but lower for temperatures

above 200˚C. For the purpose of evaluating fracture porosity below the clay cap, the reservoir temperature as estimated from downhole temperatures measurements below the clay cap is about 240˚C. The value for the **b** factor for hydrothermal fluids at 240°C is 0.28824.

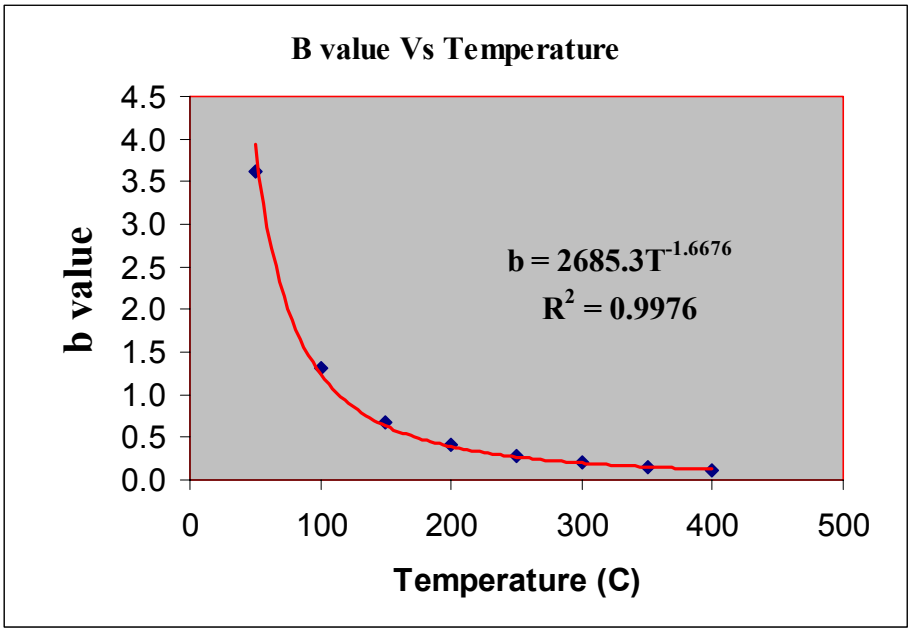

Equations above can be evaluated by considering different values of fracture porosity. We can consider two cases where the fracture porosity is very small and the second case where fracture porosity is dominant.

In the first case where fracture porosity is very small and substituting zero for the value of porosity in equation 4.8, then the measured resistivity depends only on the resistivity of the hydrothermal fluid as shown below.

$$\frac{1}{\rho} = \frac{0.22}{2.0049\rho_w} \qquad 4.12$$

This means that when fracture porosity is very small, the measured resistivity for rocks filled with meteoric water is very high. When fracture porosity is very high (totally

fractured and saturated rock), the measured resistivity is both a function of fluid resistivity and the b factor as shown below:

$$\frac{1}{\rho} = \frac{0.22}{\rho_w} + \frac{1}{b} \qquad 4.13$$

By considering the anticipated reservoir temperatures of more than 240˚C, equations 4.5 and 4.18 can be rearranged as shown below to solve for porosity using basis functions which finds a point with a value near zero as the solution for the resistivity equation to solve for the fracture porosity of the rocks given the range of the resistivity of the formation, the resistivity of the hydrothermal fluid at 240°C, very low percentage of clay and full saturation. For equation 4.8, the **b** factor and the resistivity of the hydrothermal fluid is determined from equation $b = 2685.3T^{-1.6676}$.

$$f(\Phi) = \frac{(1-\Phi)(1-P_c)}{\rho_b} + \frac{Pc(1-\Phi)}{\rho_c} + \frac{\Phi S_w}{\rho_w} + \frac{\Phi(1-S_w)}{\rho_a} - \frac{1}{\rho} \qquad 4.14$$

$$f(\Phi) = -\frac{1}{\rho} + \frac{0.22}{\rho_w}\left[1-(1-\Phi_f)^{2/3} + \frac{(1-\Phi_f)^{2/3}}{1+(1-\Phi_f)^{1/3}+(1-\Phi_f)^{1/3}4.9x10^{-3}}\right] + \frac{\Phi_f{}^{1.06}}{b} \qquad 4.15$$

The basis function tries to find a zero of the equation with one variable in this case porosity with a specified staring interval between 0.0001-0.9. The algorithm uses a combination of bisection, secant, and inverse quadratic interpolation methods to determine porosity. The algorithm was evaluated for both equation 4.14 and 4.15. In equation 4.14, a solution was found for values of a percentage of clay at about 10 percent, matrix resistivity of 5,000 Ωm (which was determined from the highest value of

resistivity from 2-D MT data interpretation), and resistivity of clay at about 5Ωm, and water resistivity of 7Ωm. The value of the water resistivity is slightly lower than that of 10-15 Ωm for measured resistivity of fresh-water hydrothermal systems Arnasson et al., 2000.

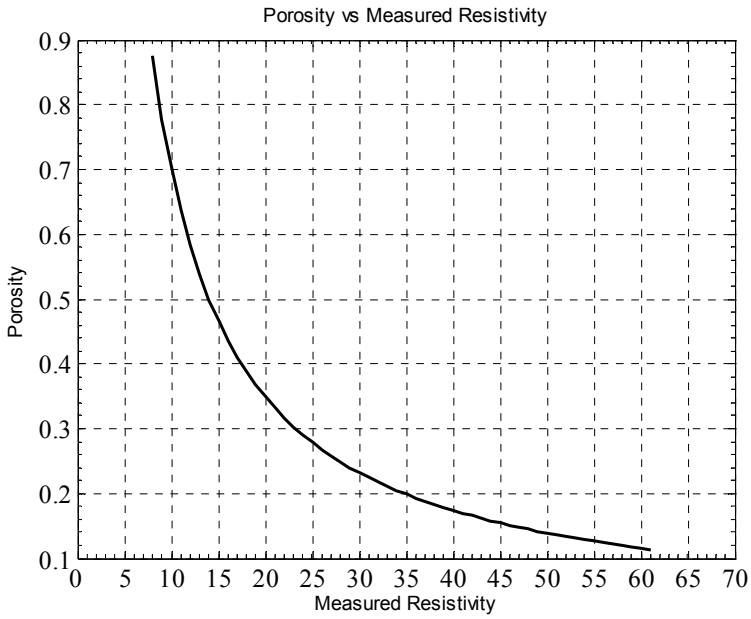

Analysis of the results for both methods indicates that equation 4.8 which takes into account the effect of temperature underestimates the porosity determined from some cores in the hydrothermal field.

From this analysis, there is a very narrow range (5-60Ωm) of resistivity for high fracture porosity of more than 10%. The fracture porosity is very low for resistivity more than 60Ωm. Based on this analysis, postulated that the areas with high resistivity at a depth of more than 1000m would have low fracture porosity.

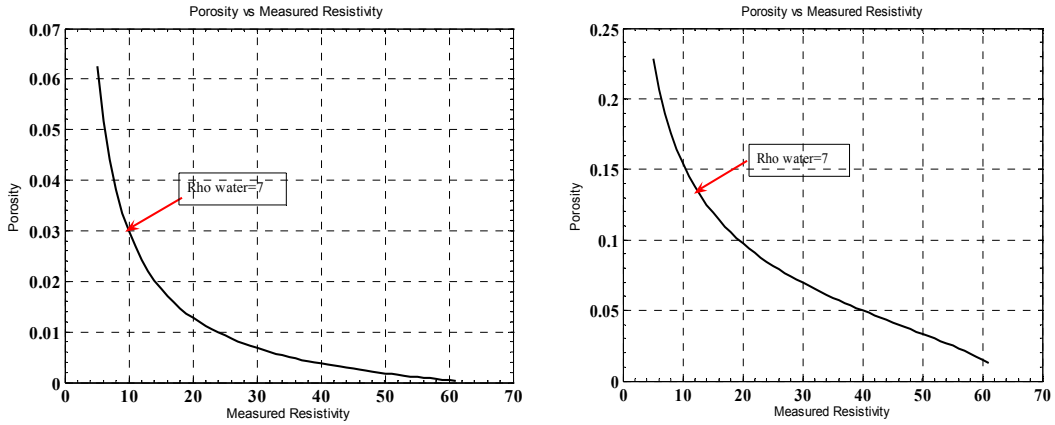

From the analysis of the resistivity and porosity from equation 4.14, the value of porosity is obtained is very low and not consistent with some of the porosity data from the hydrothermal system. When exponent of fracture porosity is modified from 1.06 to a value greater than 2 in equation 4.8, the solution gives consistent results with the measured effective porosity of between 0-50 percent with porosity as high as 49% measured in the igneous samples and majority falling below 20% (Sigurdsson et al., 2000). The porosity values are similar to those obtained from cores in the Olkaria geothermal field in Kenya. The porosity values range from 0-45% with most samples having porosity between 5-20% (Figure). This therefore justifies the use of a high exponent for equation 4.8 to simulate the measured porosity for various hydrothermal systems located within volcanic areas. The samples from Olkaria show that porosity below an elevation of 1000masl is predominantly between 5-20 %. The porosity is higher between 1500-1000 masl.

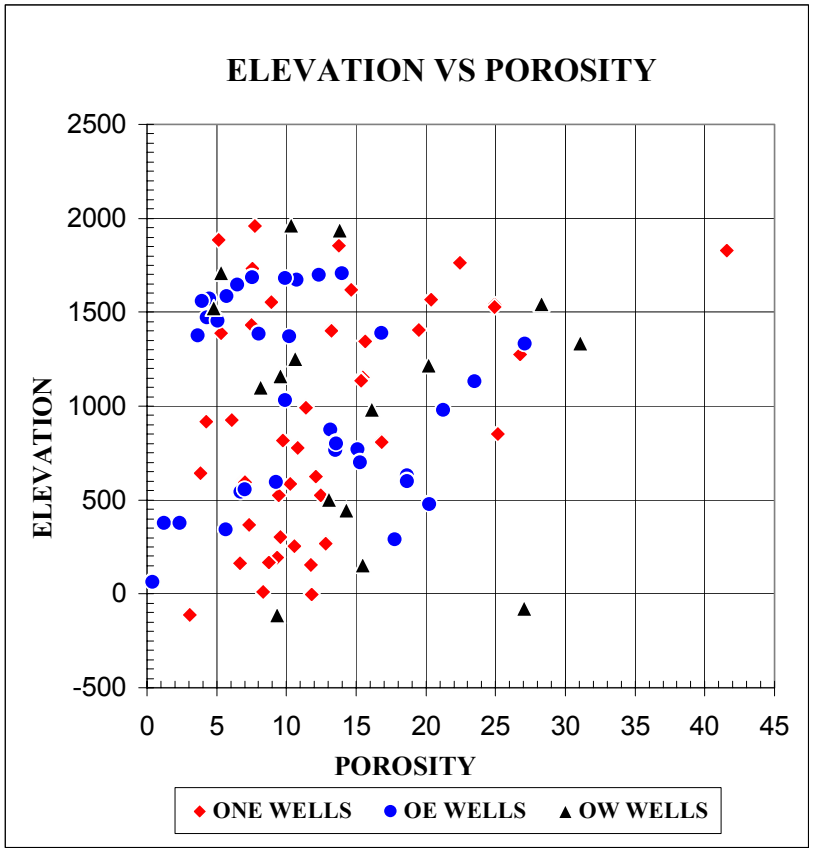

Recent studies in the characterization of subsurface fractures from azimuthal resistivity (Boadu et al., 2005) show that the presence of aligned vertical or sub vertical fractures causes azimuthal anisotropy. In this case the anisotropy can be modeled as isotropic bodies with spatial variation in resistivity and dimensions. For Azimuthal resistivity arrays, (ARS), the variation in apparent resistivity with square-array orientation over a homogeneous anisotropic earth (Lane et al., 1995) is given by:

$$\rho_a = 0.7\rho_m \left\{ \frac{2}{\left[1+(N^2-1)\cos^2\theta\right]^{1/2}} - \frac{1}{\left[2+(N^2-1)(1+\sin 2\theta\right]^{1/2}} - \frac{1}{\left[2+(N^2-1)(1-\sin 2\theta)\right]^{1/2}} \right\}$$

where $\boldsymbol{\theta}$ is the strike direction ρ_m is mean resistivity of the fracture rock, ρ_t is the apparent resistivity across the fracture and ρ_l is the apparent resistivity along the fracture and $\boldsymbol{N}$ is the effective vertical anisotropy and is related to coefficient of anisotropy $\boldsymbol{\lambda}$ and dip of the bedding plane $\boldsymbol{\alpha}$. In the case of MT resistivity, we consider the TE and TM mode resistivity and the Invariant resistivity as the mean resistivity.

$$N = \left[1 + (\lambda^2 - 1)\sin^2 \alpha\right]^{1/2}$$

In this study we assume that the fractures are vertical and the above equation can be reduced to

$$\lambda = \left(\rho_t \big/ \rho_l\right)^{1/2}$$

$$\rho_m = \left(\rho_t \rho_l\right)^{1/2}$$

The fracture strikes are usually estimated from polar plots (Habberjam, 1972) to find the dominant structural orientation. In this study we use the directions obtained from both MT polarization and shear wave splitting at four of the sites.

In this model, fracture porosity is modeled as a measure of fluid storage potential of a fractured rock mass (Boadu et al., 2005). The fracture porosity is estimated from the expression derived by Lane et al., 1995. The results of this model are compared to those of the previous models already discussed.

$$\Phi_f = \frac{3.31x10^4 (N-1)(N^2-1)}{N^2 C(\rho_{\max} - \rho_{\min})}$$

where $C(\mu S/cm)$ is the specific conductance of the pore fluid filling the fractures.

4.1.2 Relationship between P-wave velocity, porosity and resistivity

P-wave velocity and porosity relationship has been established based on the equation by Wyllie (1958) shown below.

$$\frac{1}{V_p} = \frac{\Phi_t}{V_w} + \frac{1-\Phi_t}{V_r} \qquad 4.16$$

where V_p is the bulk P-wave velocity, V_w is the P-wave velocity in water, V_r is the P-wave velocity of the rock matrix and Φ_t is the total porosity and in this study we assume that it is equivalent to fracture porosity. Based on a 2-km core from Eastern Iceland, Christensen and Wilkens (1982) concluded that the Wyllie equation was a good approximation of the interpreted P-wave velocity with V_w=1500 ms^{-1} and V_r=6250 ms^{-1}.

This relationship together with the Wyllie equation was used to give the empirical relationship between the porosity and the P-wave velocity as given by the dimensionless fracture velocity:

$$\Phi_f = 1974 ms^{-1} V_p^{-1} - 0.32 \qquad 4.14$$

Based on the assumption that both the P-Wave velocity and resistivity are affected by fracture porosity and considering equations 4.5, 4.7, 4.8 and 4.13, if the fracture porosity and the resistivity of the fluid are known, then P-wave velocity can be calculated. In this study, we use the range of porosity and resistivity values obtain from modeling the MT data to estimate the velocity model which is then used to locate the microearthquakes. From the analysis of the relationship between resistivity and porosity,

this study assumes that in areas with resistivity high than 60 Ωm the fracture porosity is very low and therefore from equation 4.14, the P-wave velocity approaches that of the rock matrix. We therefore expect that the variation in porosity is significant only in areas with low resistivity. The modified equation 4.8 that conforms to the observed porosity can be expressed as shown below:

$$f(\Phi) = -\frac{1}{\rho} + \frac{0.22}{\rho_w}\left[1-(1-\Phi_f)^{2/3} + \frac{(1-\Phi_f)^{2/3}}{1+(1-\Phi_f)^{1/3}+(1-\Phi_f)^{1/3}4.9x10^{-3}}\right] + \frac{\Phi_f{}^2}{b} \qquad 4.16$$

This equation can be equated to equation 4.14 to obtain the relationship between the measured resistivity and the P-wave velocity. From the solution of the porosity and measured resistivity (Figure) we assume that for areas of resistivity high than 60 Ωm, the P-wave velocity will be equal to that of the rock matrix V_r=6250 ms^{-1}. If measurements of the matrix p-wave velocity are known the value can be substituted in this equation. We obtained the solution for the resistivity and porosity and used them to determine P-wave velocity. As an example, when the measured resistivity is about 10Ωm, the porosity is 15% and equation 4.14 can be expressed as:

$$0.15 = 1974ms^{-1}V_p{}^{-1} - 0.32 \qquad 4.17$$

$$V_p = \frac{1974ms^{-1}}{0.47} = 4200\text{ms}^{-1} \qquad 4.18$$

This value is consistent with expected acoustic P-wave velocity of 4000-4600 m/s for basaltic samples with grain densities higher than 3000 kg//m^3 (Sigurdsson et al., 2000).

4.2 Analysis of MT and shear wave polarization

Anisotropy in the resistivity of rocks is caused by either orientation of elongated rock grains or from fine layering with different resistivity values. Anisotropy in hydrothermal systems can result from directional fracturing, pressure gradients, fluid content, and degree of hydrothermal alteration and orientation of pore spaces. We shall consider here anisotropy with vertical or inclined layering

A major problem in analyzing and interpreting shear wave anisotropy recorded by surface measurements is determining the depth of the anisotropy (Crampin and Peacock 2004). As part of this study, the depth to the resistivity interface is used to model the anisotropy. In general the observed anisotropy is a combination if various factors including permeability, fluid content, fracture size and orientation, orientation of grains in the rocks and the materials constituting the rocks. The model used for the analysis of MT and shear wave splitting is shown below:

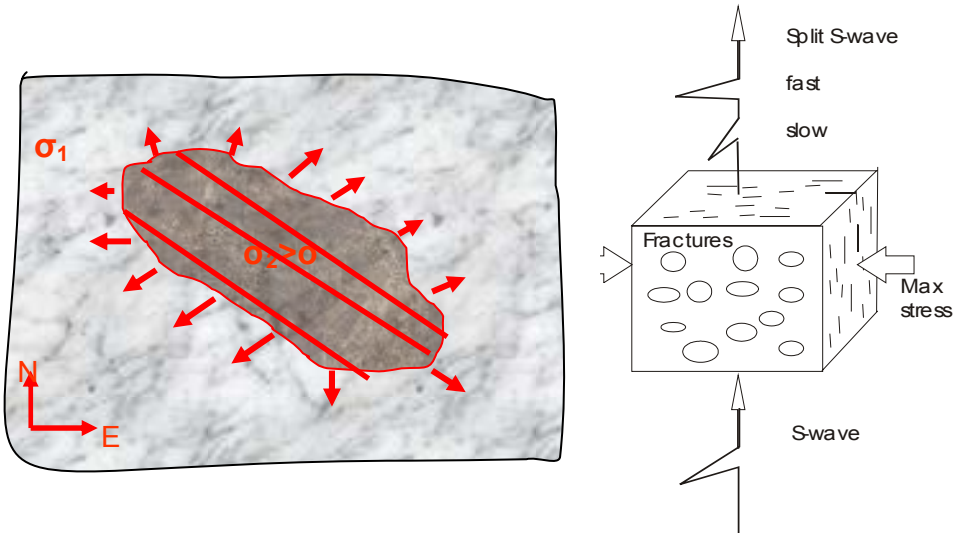

In this study, we assume that the polarization is both MT and shear wave splitting is caused by fluid filled fractures. If we consider a rock mass higher conductivity embedded in a host rock with lower conductivity, the induction arrows point away from the conductor and a normal to the conductor at any given measurement point direction defines the polarization direction. The shear wave is polarized into a fast and slow wave. The fast wave is parallel to the direction of maximum stress while the slow wave is perpendicular to the fractures.

In shear wave splitting models, the only data available is arrival times and location of stations. The unknown are the velocity structure and the location of the earthquakes. In modeling, it is common to assign a velocity model and then locate the events. After locating many events, is then the standard practice to use the locations to improve on the velocity model. A list of the location of microearthquake stations is required by the program to locate earthquakes. The locations were determined from the internal GPS measurements and cross checked with locations from the hand held GPS.

The microearthquakes are located at a reference datum which is the average of the stations. Station corrections are incorporated to account for the elevation differences with respect to average elevation. The station corrections are computed by locating many earthquakes with zero corrections and then assign the average time errors as station correction.

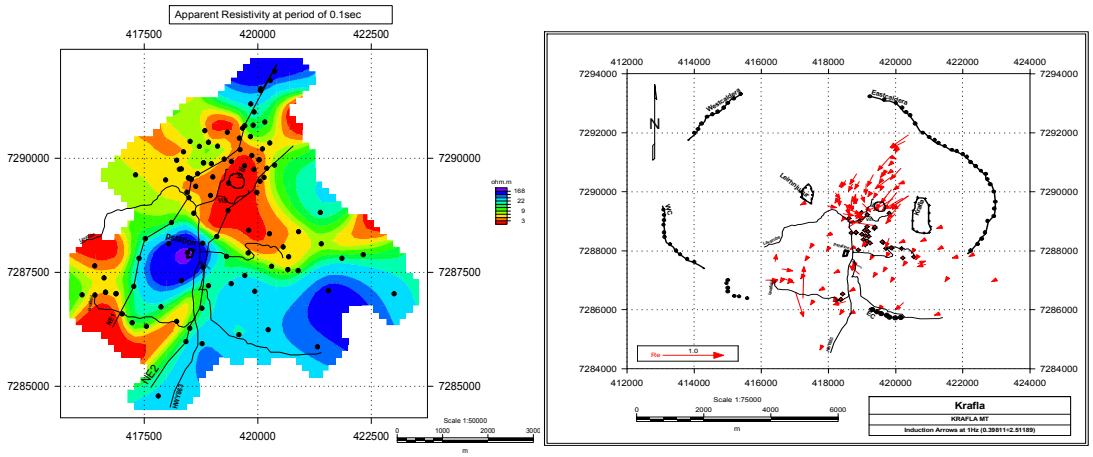

4.3 Generating 1-D P-wave velocity model from resistivity

Based on the results of equations 4.16 to 4.18, it is possible to generate a velocity model from the measured resistivity with the given assumption that for resistivity above 60Ωm, the P-wave velocity approaches that of the rock matrix of un-fractured and unaltered basalt. As an initial example we consider the average invariant resistivity for an 8 layer model for the sites in the area where most of the earthquakes occur.

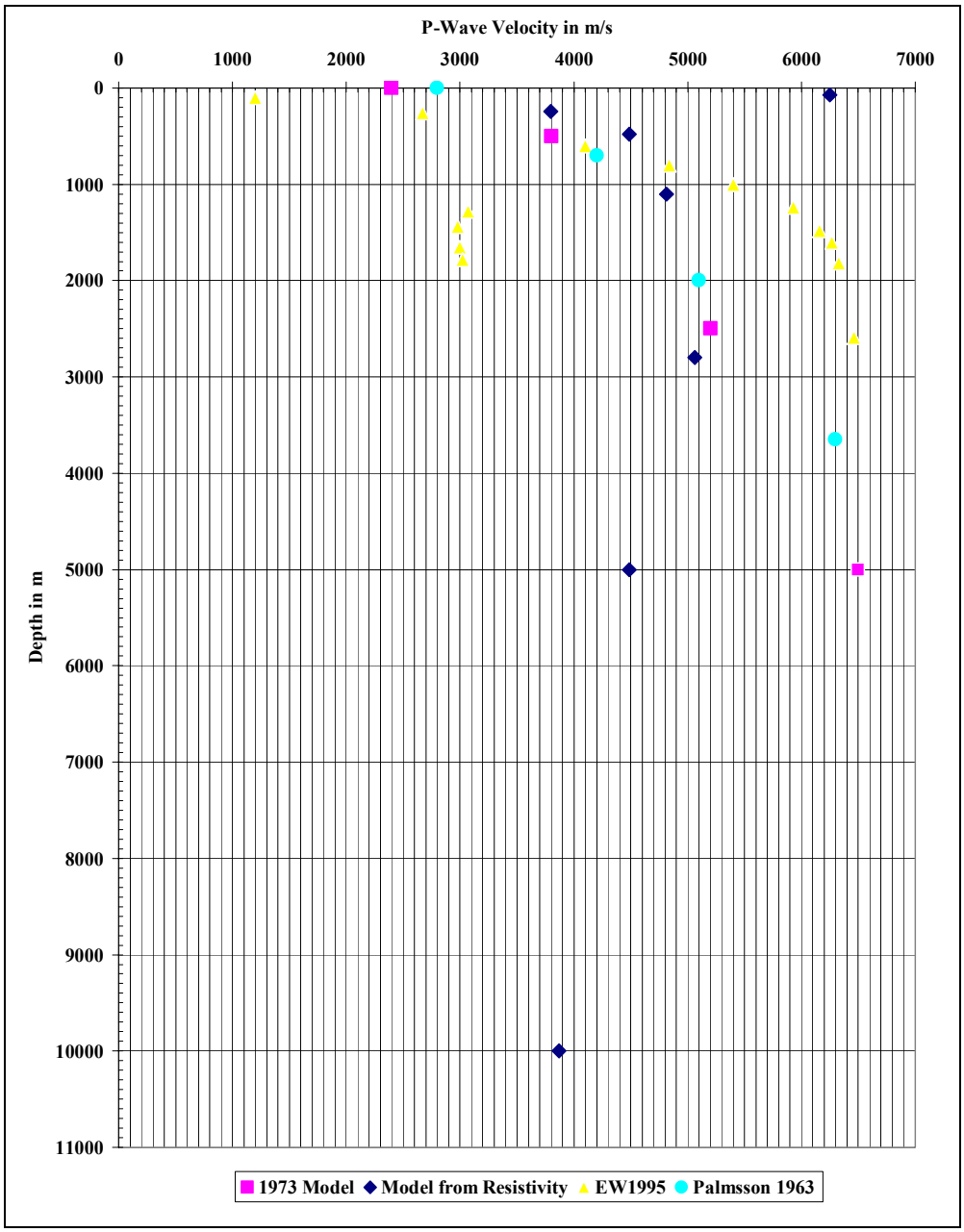

Several P-wave velocity models have been used to model the structure of the Krafla area. Plots of some of the models together with that generated from the resistivity from this study are very comparable within the depth range of 0-1000m. One advantage of using the resistivity model is that it can give a better understanding of the deeper

velocity model. The use of resistivity can also improve the 3-D model velocity structure. In particular the resistivity generated model indicates that the P-wave velocity decreases at a depth of more than 3000m. Due to high resistivity near the surface the P-wave generated model gives high velocity near the surface.

4.4 Microearthquake relocation using P-wave models generated from resistivity

4.5 Analysis of reflections from the magmatic body below the hydrothermal system

Based on the conceptual model that a heat source occurs above the hydrothermal reservoir and the interpretation that the heat source is associated with low resistivity and lower acoustic, it is expected that some reflections would occur for the earthquakes that have their origin above the heat source. Analysis of some of the earthquakes recorded during the field campaign in 2005, shows that some stations show clear large amplitude signals between the P-wave and S-wave arrivals. In this study we interpret these signals as conversions of S-waves to P-waves as shown on the example below. Stroujkova, 2000 used the methods of first-order scattering and stacking to find the likely location and shape of the reflecting zone on microearthquake clusters in the Mammoth Lakes. Based on the particle motions, it was postulated that the reflections were either from the transition of solid to partially molten rock or the transition from dry rock to fluid saturation. In this study we assume that the reflection is from the top of molten rock

mixed with hydrothermal fluids. Several previous studies have found reflectors both in volcanic and rift zones (Ake and Sanford, 1988., Sanford et al., 1973).

Based on the conceptual model for this study, the earthquakes occur above the heat source as shown below.

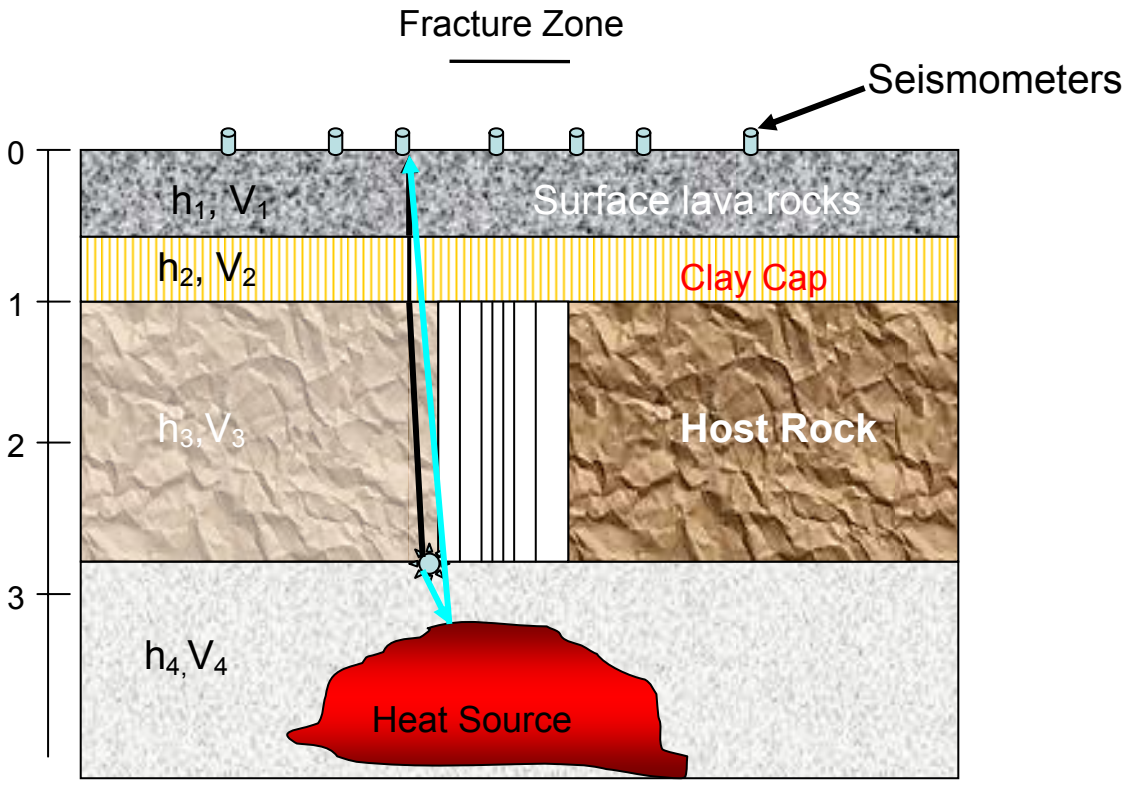

If we consider an earthquake generated on the boundary of the third and fourth layer above the heat source, the head wave travels upwards through the layers 3, 2 and 1. The arrival time is a summation of the origin time and the travel time for both P and S-waves as shown below:

$$T_P = t_o + t_p$$

where $t_P = \sum_{i=j-1}^{1} h_i / V_{Pi}$ and $j = layers$

For S-Wave to P-wave conversion on top of the heat source, the arrival time is given by:

$$T_{SP} = t_0 + h_4 / V_{S4} + h_4 / V_{P4} + t_p$$

The difference in arrival time t_{sp} between the P-wave and the converted S-P wave is given by:

$$t_{SP} = T_{SP} - T_p = h_4 / V_{S4} + h_4 / V_{P4} = h_4 \left(1/V_{S4} + 1/V_{P4} \right)$$

From the equation above, if the depth of the earthquake is known, then the depth to the heat source can be calculated from the equation shown below;

$$D_{heatsource} = D_{earthquake} + \left(t_{sp} V_{S4} V_{P4} / V_{p4} - V_{S4} \right)$$

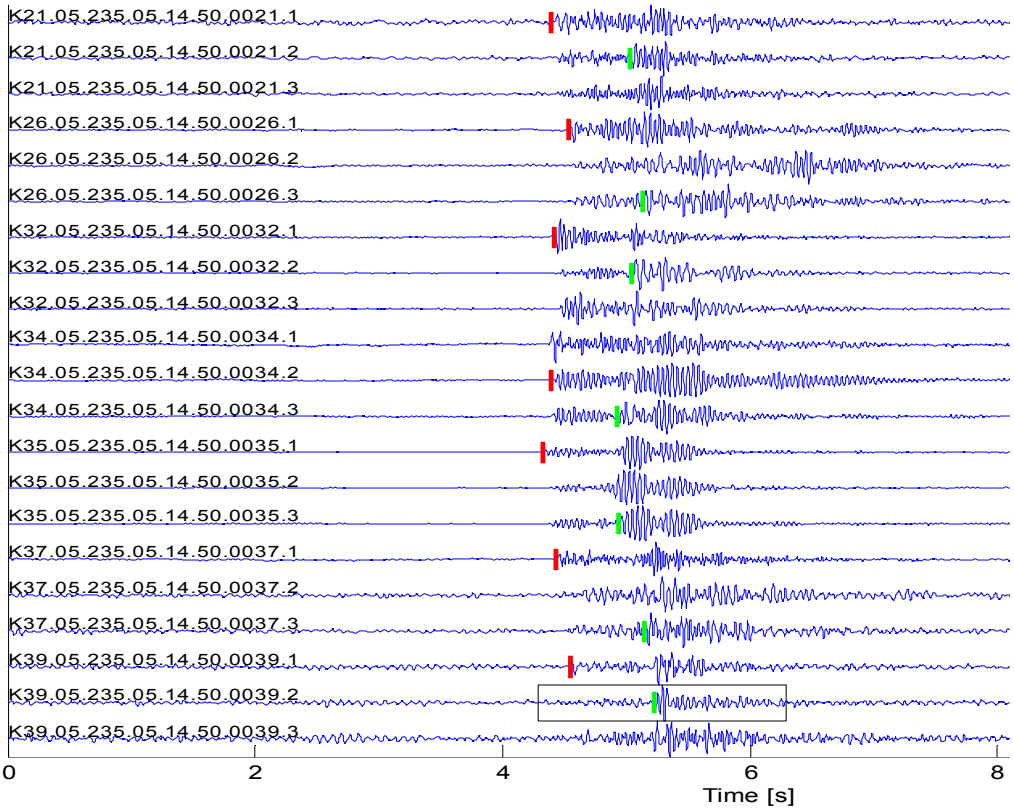

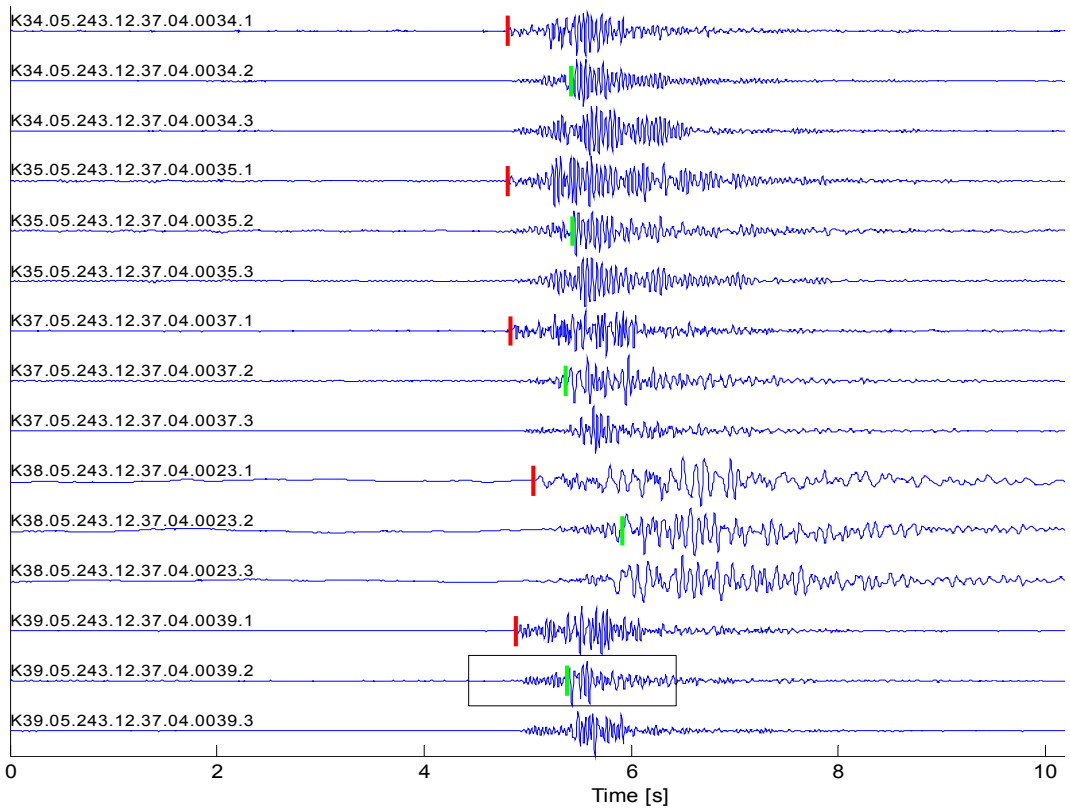
K34.05.243.12.37.04.0034.1
K34.05.243.12.37.04.0034.2
K34.05.243.12.37.04.0034.3
K35.05.243.12.37.04.0035.1
K35.05.243.12.37.04.0035.2
K35.05.243.12.37.04.0035.3
K37.05.243.12.37.04.0037.1
K37.05.243.12.37.04.0037.2
K37.05.243.12.37.04.0037.3
K38.05.243.12.37.04.0023.1
K38.05.243.12.37.04.0023.2
K38.05.243.12.37.04.0023.3
K39.05.243.12.37.04.0039.1
K39.05.243.12.37.04.0039.2
K39.05.243.12.37.04.0039.3
0
2
4
6
8
10
Time [s]

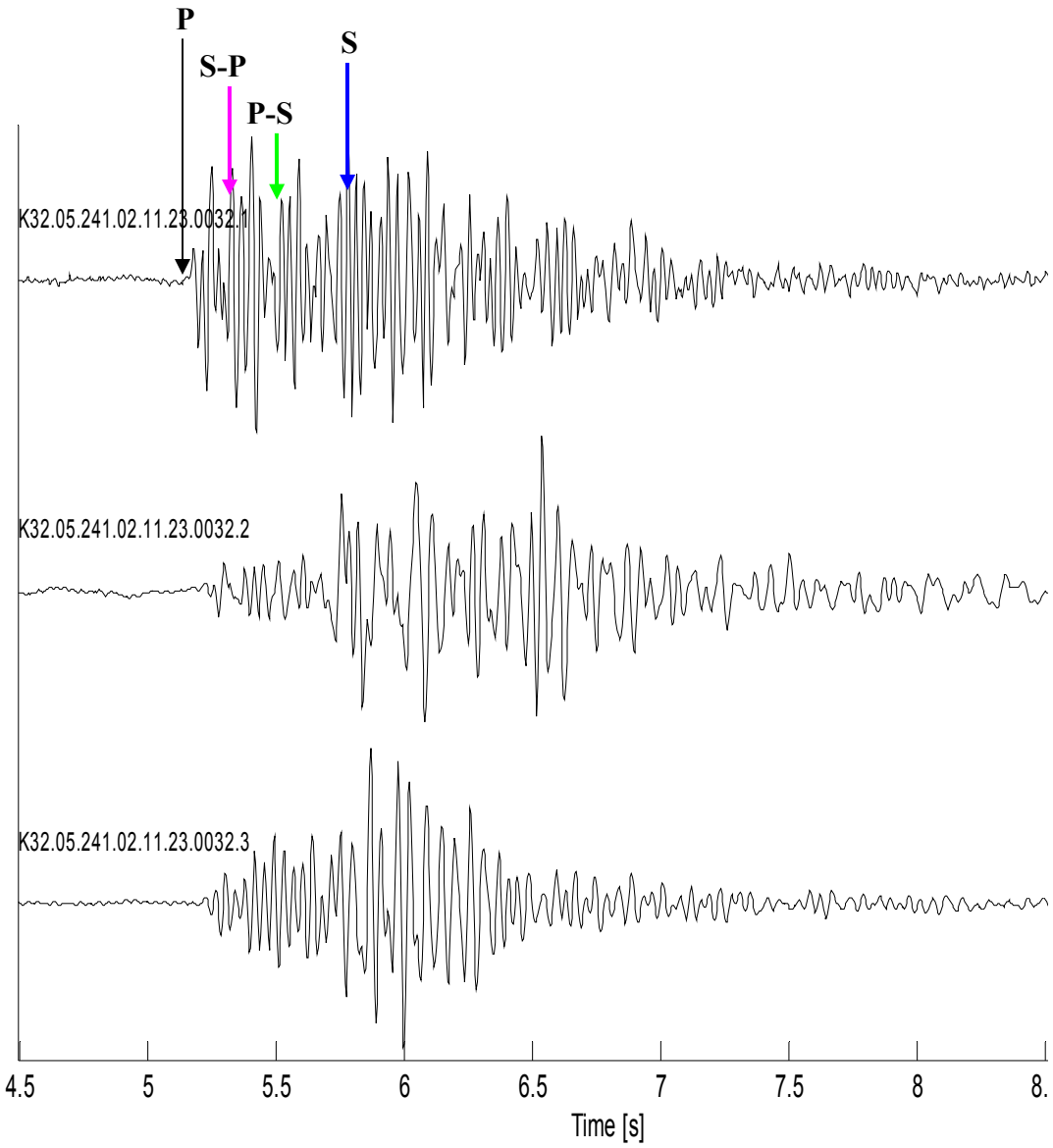
P
S-P
P-S
S
K32.05.241.02.11.23.0032.1
K32.05.241.02.11.23.0032.2
K32.05.241.02.11.23.0032.3
4.5
5
5.5
6
6.5
7
7.5
8
8.
Time [s]

5. Summary of results and conclusions

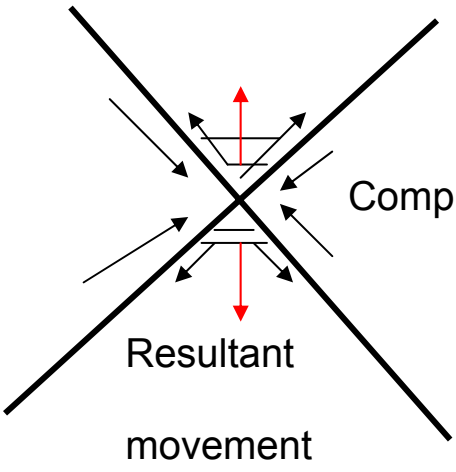

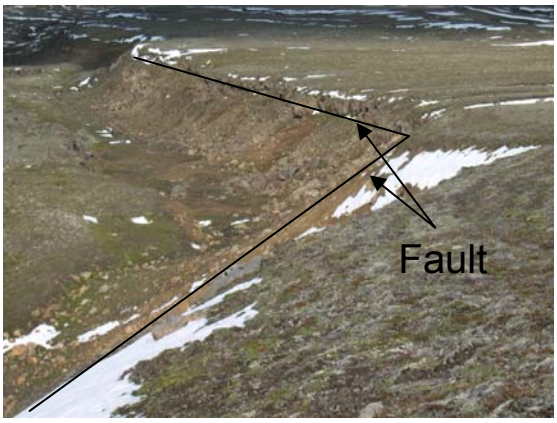

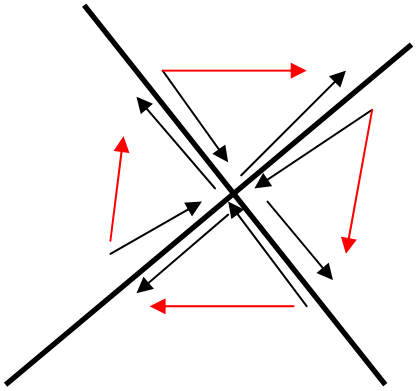

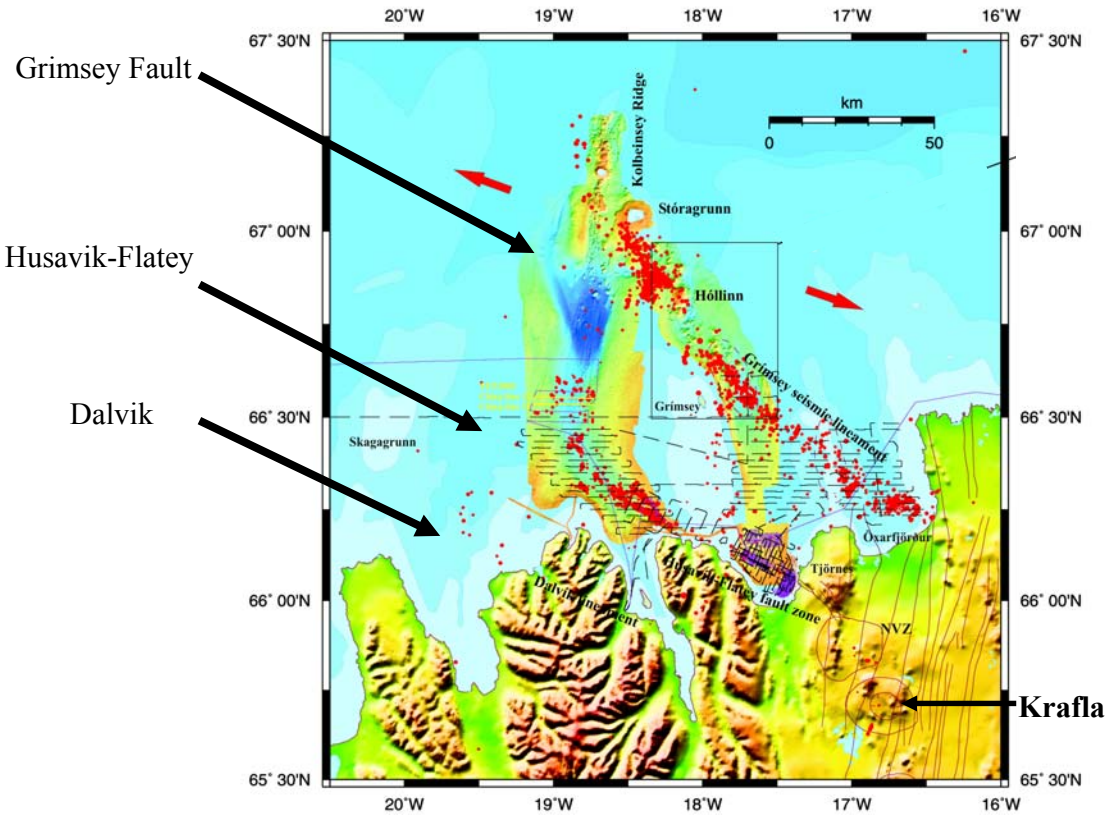
Grimsey Fault
Husavik-Flatey
Dalvik
Krafla
20°W
19°W
18°W
17°W
16°W
67° 30'N
67° 00'N
66° 30'N
66° 00'N
65° 30'N
km
0
50
Kolbeinsey Ridge
Stóragrunn
Hóllinn
Grimsey
Grimsey seismic lineament
Skagagrunn
Öxarfjörður
Tjörnes
Husavik-Flatey fault zone
NVZ

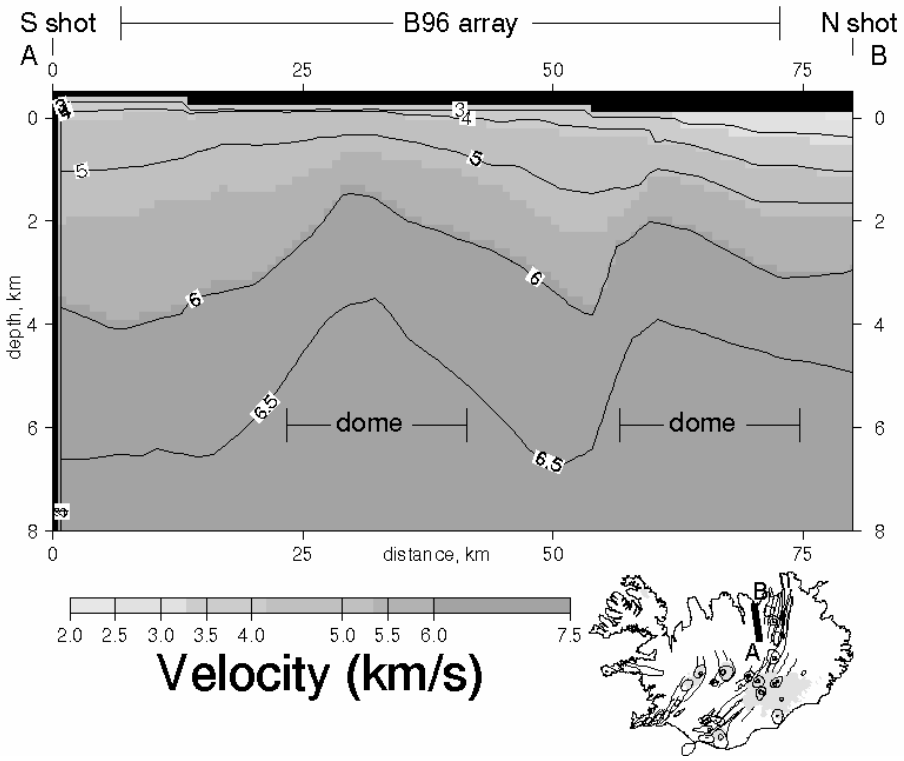

Krafla geothermal field at the intersection of a subsurface NW-trending (transform?) fault zone in older basalts and younger dikes/fissures that cut both older and younger basalts.

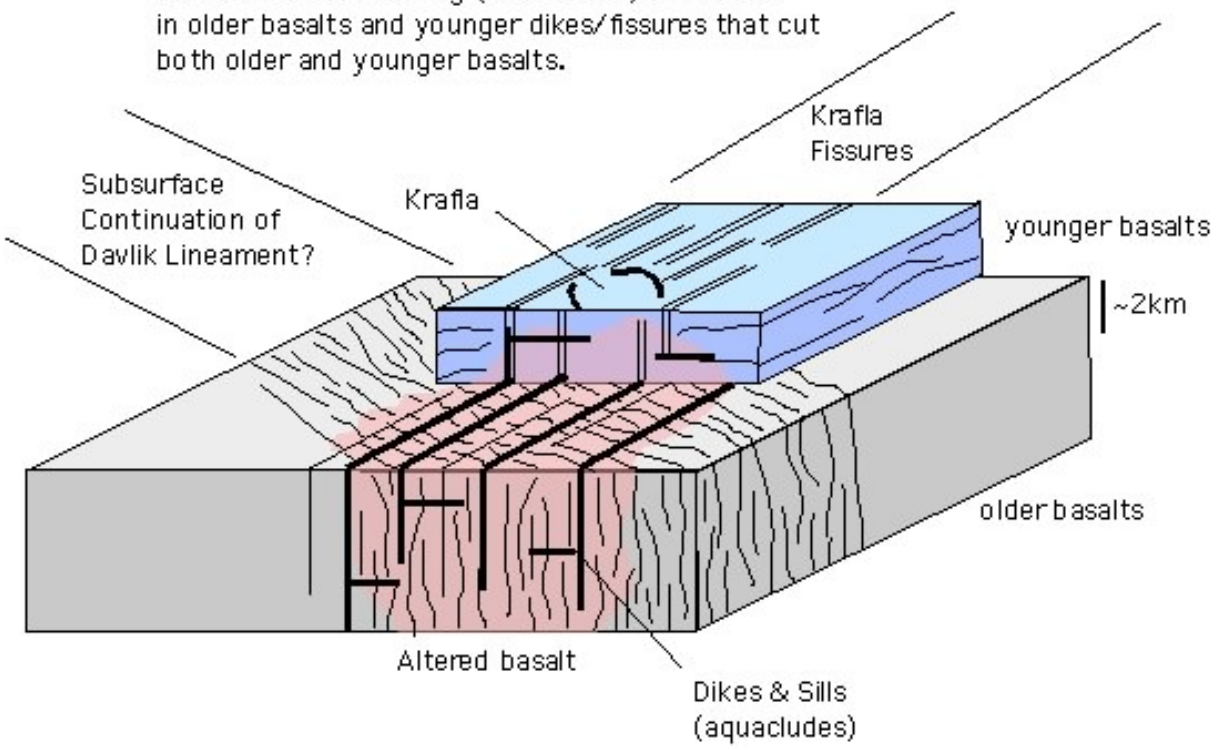

References

Berdichevsky, M. N., V. I. Dmitriev, and E. E. Pozdnjakova (1998), On two-dimensional interpretation of magnetotelluric soundings, Geophysical Journal International, 133, 585-606.

Flovenz, O. G., L. S. Georgsson, and K. Arnason (1985), Resistivity Structure of the Upper Crust in Iceland, Journal of Geophysical Research-Solid Earth and Planets, 90, 136-150.

ighian, M. N. (1979), Quasi-Static Transient-Response of a Conducting Half-Space - Approximate Representation, Geophysics, 44, 1700-1705.

Pellerin, L., and G. W. Hohmann (1990), Transient Electromagnetic Inversion - a Remedy for Magnetotelluric Static Shifts, Geophysics, 55, 1242-1250.

Spies, B. R. (1989), Depth of Investigation in Electromagnetic Sounding Methods, Geophysics, 54, 872-888.

Sternberg, B. K., J. C. Washburne, and L. Pellerin (1988), Correction for the Static Shift in Magnetotellurics Using Transient Electromagnetic Soundings, Geophysics, 53, 1459-1468.

BIOGRAPHY

A brief biography, ordinarily not more than one page in length, is required in doctoral dissertations. Your biography should include (1) the place and date of your birth, (2) the colleges or universities attended with the degrees received and their dates, (3) the titles of all books and articles you have published, and (4) a list of scholarships, fellowships, memberships in honorary societies, and academic honors you received since obtaining the bachelor's degree. The biography should appear on the very last page of your dissertation.

KJ-29 is a 2103 m deep well in the Leirbotnar field of the Krafla high-temperature area, NE-Iceland. It was drilled this year to mine steam for electrical production. The discharge of the well is very high. This study deals with the upper 1000 m of the well. The rock formation dissected by the well consists of basaltic hyaloclastite formations and basaltic lava series which are believed to have accumulated during the last glacial and interglacial periods. Intrusive rocks of basalt/dolerite composition occur below 530 m depth and predominate from 990 m down to the bottom of the well. Aquifers were confirmed at 100-155, 275, 600, 680, 730, 800 and 930 m depth, mostly related to intrusion contacts and fractures. Five alteration zones are identified including a smectite-zeolite zone (<200°C) down to 212 m depth, a mixed-layer clay zone (200-230°C) down to 420 m depth, a chlorite zone (230-250°C) down to 822 m depth, a chlorite-epidote zone (250-280°C) down to 998 m depth and an epidote-actinolite zone (>280°C) from there down to the bottom of the well. Measured temperatures in the lower part of the well

are roughly comparable with the alteration temperatures. These evidences indicate a stable high-temperature environment. The early occurrence of wairakite and quartz may be related to an earlier hydrothermal event, presumably within the last glacial period. Hydrothermal evolution, as seen through alteration, indicates an initial low-temperature condition followed through intermediate to a high-temperature environment. The geology of the well confirmed that it is situated inside the horst system in the Krafla caldera, close to a fault related upflow zone causing an elevation of alteration zones to shallow depths.